

https://dspace.org/

Mapping and monitoring the impacts of climate variability on rainfed agriculture in Semi-arid North Darfur, Sudan

Altoom, Mohammed Bashar Adam

2024-02

University of the Witwatersrand, Johannesburg

https://hdl.handle.net/10539/45911

Altoom, Mohammed B.A.. (2024). Mapping and monitoring the impacts of climate variability on rainfed agriculture in Semi-arid North Darfur, Sudan. [PhD thesis, University of the Witwatersrand, Johannesburg]. WIReDSpace. https://hdl.handle.net/10539/45911

Downloaded from a DSpace repository. https://dspace.org/



Mapping and monitoring the impacts of climate variability on rainfed agriculture in Semi-arid North Darfur, Sudan

Mohammed B.A. Altoom

A thesis submitted to the Faculty of Science, University of the Witwatersrand, in partial fulfilment of the academic requirements for the degree of Doctor of Philosophy in Geography and Environmental Sciences

February 2024
Johannesburg
South Africa

Abstract

Rainfed agriculture is vital to food security and income in most parts of the world. However, one-third of the population of developing countries population lives in the less favoured rainfed agricultural regions. Around 75-82% of the total cropland areas in the world are under rainfed agriculture and produce more than 60% of the globe's cereal grains. However, rainfed agriculture is most prominent in some regions of Africa, such as Sub-Saharan Africa, where more than 95% of the cropland is rainfed. This crucial agriculture sector usually depends on the physical environment and, most importantly, the variability and distribution of rainfall. Therefore, rainfed farming is vulnerable to climate-related hazards, and the crop yield is unreliable and difficult to predict. For instance, the spatio-temporal variability of precipitation extreme events often subjects crops to short-term water deficits, causing crop losses. Sudan heavily depends on rainfed agriculture—about 90% of arable land dominates rainfed cultivation, contributing one-third of the country's gross domestic product (GDP). Rainfed agriculture is the primary source of livelihood for 65% of the population. Unfortunately, agriculture in North Darfur of the west Sudan is characterised by environmental hazards, e.g., frequent droughts and unpredictable low, poorly distributed, and highly variable monthly/ seasonal rainfall.

Therefore, using various Earth observation data, this study aimed to monitor the impacts of rainfall variability on rainfed agriculture in North Darfur State in Sudan. Firstly, the study aimed to determine the feasibility of estimating rainfall variability across North Darfur State at daily, monthly and annual timescales using six satellite precipitation products (SPPs), i.e., the Tropical Rainfall Measuring Mission (TRMM) Multi-satellite Precipitation Analysis (TMPA), African Rainfall Climatology (ARC), and Climate Hazards Group Infrared Precipitation with Station Data (CHIRPS) were evaluated using four categorical indices, i.e., probability of detection (POD), probability of false alarm (POFA), bias in detection (BID) and Heidke skill score (HSS), and four continuous indices, i.e., Pearson correlation coefficient (r), root mean square error (RMSE), per cent bias (Pbias), and Nash-Sutcliffe model efficiency coefficient (NSE) against ground rain-gauge observations. The other SPPs were Integrated Multi-satellitE Retrievals for Global Precipitation Measurements (GPM) Final Run (GPMIMERG), Precipitation Estimation from Remote Sensing Information using Artificial Neural Networks-Climate Data Record (PERSIANN-CDR), and the Tropical Applications of Meteorology using SATellite and ground-based observations (TAMSAT). Results of the statistical analysis demonstrated that 1) at the daily timescale, the SPPs underestimate daily rainfall by 6.53–17.61%, and CHIRPS was the best for detecting rainy days, while PERSIANN-CDR performed poorly; 2) monthly and annual scales performed better than daily timescale, and TAMSAT and CHIRPS portrayed better performance than the other SPPs.

Secondly, the study assessed the capability of optical Earth Observation Data (EOD), i.e., Sentinel-2 multispectral dataset, to map crop types in the heterogeneous semi-arid environment of North Darfur using machine learning classifiers in Google Earth Engine (GEE) platform. Five datasets were compared against random forest (RF) and support vector machine (SVM) classification algorithms: (1) 10 Sentinel-2 bands (comprising visible, near-infrared and shortwave infrared bands), (2) Sentinel-2 (10 bands) + 8 vegetation indices, (3) visible bands and near-infrared bands only, (4) visible and shortwave infrared bands only, and (5) 8 vegetation indices. The eight vegetation indices were normalised difference vegetation index (NDVI), enhanced vegetation index (EVI), soil-adjusted vegetation index (SAVI), green-normalised difference vegetation index (GNDVI, weighted difference vegetation index (WDVI), red edge NDVI (NDVIre), ratio-vegetation index (RVI) and normalised difference

infrared index (NDII). Results showed that the RF algorithm produced the highest classification overall accuracy (OA), i.e., 97% and Kappa coefficient (κ), 0.96, using 10 Sentinel-2 bands dataset. Producer's (PA) and user's accuracies (UA) were in the range of 40-97% and 40-100%, respectively.

Thirdly, the spatiotemporal trend of drought events and their impact on millet production in North Darfur from 1981 to 2020 was analyzed using standardized precipitation index (SPI) and reconnaissance drought index (RDI) by employing different timescales, i.e., 3-month (June-August), 6-month (June-November), and 9-month (June-February) timescales. Drought-yield relationships were assessed using Pearson correlation coefficients (r). Results indicated that RDI is more sensitive to rainfall variabilities than SPI in detecting drought trends. Results revealed that drought events affected North Darfur over broad spatial extents, particularly in 1989, 1990, 1992, 1999, and 2001—an extreme drought event was in 2003. Correlation analysis between the SPI and RDI and the standardized variable of crop yield (SVCY) for millet grain yield showed a strong agreement between them. Moderate to extreme reductions in millet crop yield occurred in 1992, 1999, 2001, and 2003, corresponding to the moderate to extreme drought indicated by RDI. Severe crop losses were in Kabkabiya and Umm Kadadda.

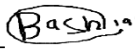
Fourthly, this study aimed to map and monitor spatio-temporal dynamics of rainfed agriculture in North Darfur State from 1984 to 2019 using multitemporal Landsat observation data using random forest (RF) classification algorithm. Overall, Landsat Operational Landsat Imageries (OLI) outperformed Landsat Multispectral Scanner (MSS), Landsat Thematic Mapper (TM), Landsat Enhanced Thematic Mapper Plus (ETM^{+}) in monitoring change in agricultural land and other land use land cover (LULC) classes. Overall accuracies ranged between 94.7% and 96.9%, while kappa statistics were greater than 0.90. Results showed that Goz land used for rainfed agriculture increased by 889,622.46 ha between 1994 and 999, while it decreased by 658,568.61 ha between 2004 and 2009. Rainfed cultivation of wadi lands expanded significantly by 580,515.03 ha over the 2014–2019 period and decreased by 182,701.8 ha over the 1994–1999 period.

Overall, this study enhances the understanding of spatio-temporal rainfall patterns and current drought trends, aiding in developing more effective policies and resource management strategies. Additionally, it offers crucial spatial data that is currently scarce due to ongoing conflicts, empowering decision-makers to establish sustainable land use monitoring systems. The methodologies used in this study have proved successful in mapping crop types in a fragmented highly heterogeneous fine agricultural semi-arid landscape; such mapping approaches can be applied in other environments with similar characteristics.

Preface

This doctoral thesis describes work undertaken as part of a program of study at the School of Geography, Archaeology, and Environmental Studies, University of the Witwatersrand, Johannesburg from January 2019 to January 2024, under the supervision of Professor Elhadi Mohammed I. Adam (School of Geography, Archaeology, and Environmental Studies, University of the Witwatersrand, Johannesburg).

This document is the result of my investigations, therefore, I have exercised reasonable care to ensure that this work is original, and where otherwise stated, all used sources of literature are listed at the end of each chapter. This doctoral thesis has not previously been submitted/ accepted in substance for any degree and is not being concurrently submitted in candidature for any degree.

Mohammed Bashar Adam Altoom_______

Date. _____05/03/2024_____

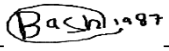
Declaration 1-Plagiaris

I, Mohammed B.A. Altoom declare that,

1. The research reported in this thesis, except where otherwise indicated, and is my original research.
2. This thesis has not been submitted for any degree or examination at any other university.
3. This thesis does not contain other persons' data, pictures, graphs or other information, unless specifically acknowledged as being sourced from other persons.
4. This thesis does not contain other persons' writing, unless specifically acknowledged as being sourced from other researchers. Where other written sources have been quoted, then:

   a. Their words have been re-written but the general information attributed to them has been referenced.

   b. Where their exact words have been used, then their writing has been placed in italics and inside quotation marks, and referenced.
5. This thesis does not contain text, graphics or tables copied and pasted from the internet, unless specifically acknowledged, and the source being detailed in the thesis and in the references section.

Singed _____  _____

Declaration 2- Publication and manuscripts

1. **Altoom**, M.B., Adam, E., and Ali, K.A. (In review). Evaluating satellite precipitation products in capturing the spatio-temporal rainfall variability across North Darfur State, Sudan. *Remote Sensing in Earth Systems Sciences*.
2. **Altoom**, M.B., Adam, E., and Ali, K.A. (In review). Mapping crop types in a heterogeneous arid environments using high-resolution multispectral dataset and machine learning algorithms in Google Earth Engine platform. *Journal of AridLand of Agriculture.*
3. **Altoom**, M.B., Adam, E., and Ali, K.A. (2024). Spatio-temporal analysis of drought and impact on millet crop production across North Darfur State using standardized precipitation index (SPI) and reconnaissance drought index (RDI). *South African Journal of Geomatics. https://dx.doi.org/10.4314/sajg.v13i1.13*
4. **Altoom**, M.B., Adam, E., and Ali, K.A. (2023). Mapping and monitoring spatio-temporal patterns of rainfed agriculture lands of North Darfur State, Sudan, using earth observation data. *Land*, 12, 307. **https://doi.org/10.3390/land12020307**.

Dedication

To my dear wife, Maani, and our child Murad, and our parents, for their constant support for my success

Acknowledgements

I am deeply thankful to the Almighty God for His grace and strength, which helped me overcome challenging times in my education and made my dream come true. I thank the University of the Witwatersrand, Johannesburg, South Africa, for giving me a Merit Award to study for a PhD, Faculty of Science at the School of Geography, Archaeology and Environmental Studies. I am extremely grateful to this institution for covering my tuition and providing me with research facilities as well as the time to work on this study.

I would like to express my sincere gratitude to my supervisor, Professor Elhadi Adam, for the incomparable academic supervision, support, and encouragement during my studies. Thank you for your moral support, encouragement, and inspiration to complete this research. I also thank Al Fashir University's "Academic Affairs Secretariat" and the Ministry of Higher Education and Scientific Research for supporting this study, without which my research could not have been solid. I would also like to thank the North Darfur State Ministry of Agriculture for giving me Meteorological and crop data.

I would like to thank Dr. Jackson for reviewing my thesis.

I am grateful to thank my family, who contributed to my overall well-being. Thanks to everyone who played a part in my research for his or her unequivocal love and support.

I am very grateful to the most important people in my life: my beloved mother, my very dear wife Maani and my child Murad, who provided me with love, patience and continuous unconditional support throughout my PhD study.

Table of Contents

Abstract ii
Preface iv
Declaration 1-Plagiaris v
Declaration 2- Publication and manuscripts vi
Dedication vii
Acknowledgements viii
List of Figures xii
List of abbreviations and acronyms xviii
1. CHAPTER ONE 1
General introduction 1
1.1 Importance of rainfed agriculture 2
1.2 Impacts of spatio-temporal rainfall variability on rainfed agriculture 2
1.3 Monitoring and mapping rainfed agriculture using Earth Observation Data 4
1.4 Statement of the study Problem 6
1.5 Research Aim and objectives 7
1.6 Scope of the study 8
1.7 The study area 8
1.8 Thesis overview 10
2. CHAPTER TWO 12
Evaluating Satellite Precipitation Products in Capturing the Spatio-temporal Rainfall Variability across North Darfur State, Sudan 12
Abstract 13
2.1 Introduction 14
2.2 Materials and methods 17
2.2.1 The study area 17
2.2.2 Datasets 19
2.2.3 Methods 22
2.3 Results 24
2.3.1 Evaluation of the rainfall estimate performance of the satellite products 24
2.3.2 Mean monthly rainfall trends 26
2.3.3 Mean annual rainfall trends 29
2.4 Discussion 31

2.4.1 Validation of satellite precipitation products at daily timescale 32
2.4.2 Validation of satellite precipitation products at monthly timescales 33
2.4.3 Validation of satellite precipitation products at annual timescales 34
2.4.4 Station-wise mean monthly and annual rainfall trends 35
2.4.5 The Study limitations 35
2.5 Conclusions 36
3. CHAPTER THREE 37
Mapping cropland types in a highly heterogeneous semi-arid environment using Sentinel-2 dataset and machine learning algorithms on Google Earth Engine cloud 37
Abstract 37
3.1 Introduction 38
3.2 Materials and Methods 41
3.2.1 Study area 41
3.2.2 Data acquisition and pre-processing 43
3.2.3 Acquisition of ground control data 45
3.2.4 Crop type mapping 47
3.2.5 Image classification 48
3.2.6 Accuracy assessment 48
3.3 Results 50
3.3.1 Crop type classification maps 50
3.3.2 Classification accuracy 57
3.4 Discussion 63
3.5 Conclusion 64
4. CHAPTER FOUR 66
Spatio-temporal Analysis of Drought and Impact on Millet Production across North Darfur State Using Standardized Precipitation Index (SPI) and Reconnaissance Drought Index (RDI) 66
Abstract 67
4.1 Introduction 68
4.2 Materials and Methods 70
4.2.1 Study area. 70
4.2.2 Dataset 72
4.2.3 Methods 73
4.3 Results 77

4.3.1 Spatio-temporal distributions of droughts in North Darfur State from 1981 to 2020 77
4.3.2 Trend analysis of drought in North Darfur State 79
4.3.3 Impact of drought on millet production 80
4.4 Discussion 82
4.5 Conclusions 84
5. CHAPTER FIVE 85
Mapping and monitoring spatio-temporal patterns of rainfed agriculture lands of North Darfur State, Sudan, using earth observation data 85
Abstract 86
5.1 Introduction 87
5.2 Materials and Methods 90
5.2.1 Study Area 90
5.2.2 Remote Sensing Data Acquisition and Pre-Processing 92
5.2.2 Reference Data 92
5.2.3 Classification of Images 94
5.2.4 Change Detection 94
5.2.5 Accuracy Assessment 95
5.3 Results 95
5.3.1 Spatial Distribution of Rainfed Agriculture and Other Land Cover Classes 95
5.3.2 Accuracy Assessment 100
5.3.3 Spatio-temporal trends of the rainfed agriculture and other land cover classes 102
5.4 Discussion 106
5.5 Conclusions 109
6. CHAPTER SIX 111
synthesis 111
6.1 Introduction 111
6.2 Evaluating satellite precipitation products in capturing the spatio-temporal rainfall variability across North Darfur State, Sudan. 112
6.3 Mapping crop types in a highly heterogeneous arid Environment using Sentinel-2 datasets and machine learning (ML) algorithms on the Google Earth Engine (GEE) cloud 113
6.4 Spatio-temporal analysis of drought and impact on millet crop production across North Darfur State using standardized precipitation index (SPI) and reconnaissance drought index (RDI) 114
6.5 Mapping and monitoring spatio-temporal patterns of rainfed agriculture lands of North Darfur State, Sudan, using earth observation data 115
6.6 Conclusions 116
References 119

List of Figures

Figure 1.1. Map of the study area showing districts and distribution of meteorological stations in North Darfur State, Sudan. 9
Figure 1.2. The climate of the North Darfur State, Sudan; mean monthly rainfall and mean monthly temperature. 11
Figure 2.1. Map of the study area in North Darfur State in Sudan; the star symbol shows locations of the rainfall stations. 19
Figure 2.2. Comparison of rain gauge observations based on monthly rainfall trends for 11 stations over North Darfur State and six-satellite precipitation products over the 20-year study period (2000–2019). 28
Figure 2.3. Comparison of rain gauge observations based on annual rainfall trends in 11 stations over North Darfur State and six SPPs over the 20-year study period (2000–2019). 30
Figure 3.1. Geographical location of the study area in Sudan shown using Sentinel-2 (S2) false colour composite (RGB: 123). 42
Figure 3.2. Classification results of spatial distribution of Crops based on the following datasets: (a) RF—10 Sentenil-2 (S2) bands, (b) RF—10 S2 bands + 8 vegetation indices (VIs), (c) RF—visible + near-infrared (VNIR) bands, (d) RF—visible + shortwave infrared (SWIR) bands, (e) RF—8 VIs; (f) SVM—10 S2 bands, (g) SVM—10 S2 bands + 8 VIs, (h) SVM—VNIR bands, (i) SVM—VSWIR bands (j) SVM—8 VIs for 2022 growing season in North Darfur, Sudan. The 10 S2 bands used— B2, B3, B4, B5, B6, B7, B8, B8A, B11, B12; 8 VIs used—normalised difference vegetation index (NDVI), enhanced vegetation index (EVI), soil-adjusted vegetation index (SAVI), green-normalised difference vegetation index (GNDVI, weighted Difference vegetation index (WDVI), red edge NDVI (NDVIre), ratio-vegetation index (RVI), and normalised difference infrared index (NDII); VNIR—visible and near-infrared; VSWIR— visible and shortwave..... 51
Figure 4.1. Map of the study area showing districts and distribution of meteorological stations in North Darfur State, Sudan. 71
Figure 4.2. Spatial patterns of drought in North Darfur State from 1981 to 2020 based on Standardized Precipitation Index (SPI) and Reconnaissance Drought Index (RDI). 78
Figure 4.3. Standardized Precipitation and Reconnaissance Drought Indices values in North Darfur State at three timescales (3-months, 6-months, 9-months and from 1981-2020. 79
Figure 4.4. Drought and crop yield analysis of Um kadada, Kabkabiya, Kutum, Mellit, and Al Fasher districts, the North Darfur from 1998-2020.. 81
Figure 5.1. Location of the study area with spatial distribution of the samples in Landsat-8 image 2019. The northern boundary for rainfed agriculture was identified in 1984 using field observation. 91
Figure 5.2. Spatial distribution of the rainfed agriculture and other LULC classes in 1984, 1989, 1994 and 1999. The classification was obtained using Landsat-5 MSS, Landsat-5TM, and random forest classifier. 97
Figure 5.3. Spatial distribution of the rainfed agriculture and other LULC classes in 2004- 2009 and 2014-2019. The classification was obtained using Landsat-7 ETM+, Landsat-8 OLI, and random forest classifier. 98

Figure 5.4. The overall accuracy and kappa coefficient achieved by random forest classifier for mapping rainfed agriculture and other LULC classes for the period between 1984 and 2019 with five years interval. 101
Figure 5.5. The magnitude of change for rainfed agriculture lands and other LULC types (BS = bare soil, PL = pastureland, RG = rainfed agriculture on goz land, SD = sand dunes, WV = woody vegetation, RW = rainfed agriculture on wadi land) of North Darfur from 2019-1984.....102
Figure 5.6. Compare area coverage by rainfed agriculture on goz land (RG) and on wadi lands (RW) and mean annual rainfall from 1984 to 2019..106

List of Tables

Table 2.1: Characteristics of the 11 rainfall stations in North Darfur State for the study period 2000–2019. 19
Table 2.2: Parameters of the satellite-based precipitation products (SPPs) used in the study for the period 2000–2019; TIR (thermal infrared) and PMW (passive microwave). 20
Table 2.3: Contingency table for comparing rain gauge measurements and satellite-based rainfall estimates. 22
Table 2.4: Statistical indices for satellite-based precipitation products (SPPs), where G = gauge rainfall amount, G = average gauge rainfall amount; S = satellite rainfall estimates, S= average satellite rainfall estimate, N = number of data pairs, H = number of precipitation events detected by both satellites and a rain gauge, M = number of precipitation events detected by a rain gauge by not detected by satellites; and F = number of precipitation events detected by satellites but not detected by rain gauges; D = correct negative. 23
Table 2.5: The point-to-pixel evaluation at a daily timescale using continuous and categorical statistical tools; probability of detection (POD), probability of false alarm (POFA), bias in detection (BID) and Heidke skill score (HSS), correlation coefficient (r), root mean square error (RMSE), per cent bias (Pbias), and Nash-Sutcliffe efficiency (NSE). 24
Table 2.6: The point-to-pixel evaluation at a monthly timescale using continuous statistical tools; correlation coefficient (r), root mean square error (RMSE), per cent bias (Pbias), and Nash-Sutcliffe efficiency (NSE). 25
Table 2.7: The point-to-pixel evaluation at an annual timescale using continuous statistical tools; correlation coefficient (r), root mean square error (RMSE), per cent bias (Pbias), and Nash-Sutcliffe efficiency (NSE). 26
Table 2.8: The Performance of six SPPs in estimating rainfall trends on a monthly timescale at 11 stations, using correlation coefficient (r) and per cent bias (Pbias %). 29
Table 2.9: The rainfall trends for the 20-year study period (2000–2019) were assessed at the annual timescale for six SPPS at 11 stations using the correlation coefficient (r) and per cent bias (Pbias %). 31
Table 3.1: Properties of Sentinel-2 (S2) images used to map crop types in North Darfur State, Sudan 43
Table 3.2: The vegetation indices (VIs) applied in this work and computed in the Google Earth Engine (GEE); NIR near-infrared, SWIR shortwave infrared 45
Table 3.3: Reference data for cropland sites and common land cover/land use classes. The mean reflectance curves were constructed using spectral data Sentinel-2 Multi-Spectral Instrument (MSI) dataset using reference points 46

Table 3.4: Confusion matrix equations used to calculate kappa (κ), overall accuracy (OA), producer accuracy (PA), user accuracy (UA), and F1 score. 49
Table 3.5: Total estimated area (in ha) of crop types in the classified maps derived from various datasets using random forest (RF) classifier; 10 Sentinel-2 (S2) bands used— B2, B3, B4, B5, B6, B7, B8, B8A, B11, B12; 8 vegetation indices (VIs) used— normalised difference vegetation index (NDVI), enhanced vegetation index (EVI), soil-adjusted vegetation index (SAVI), green-normalised difference vegetation index (GNDVI, weighted Difference vegetation index (WDVI), red edge NDVI (NDVIre), ratio-vegetation index (RVI), and normalised difference infrared index (NDII); VNIR— visible and near-infrared; VSWIR— visible and shortwave 54
Table 3.6: Total estimated area (in ha) of crop types in the classified maps derived from various datasets using support vector machine (SVM) classifier: 10 Sentinel-2 (S2) bands used— B2, B3, B4, B5, B6, B7, B8, B8A, B11, B12; 8 vegetation indices (VIs) used— normalised difference vegetation index (NDVI), enhanced vegetation index (EVI), soil-adjusted vegetation index (SAVI), green-normalised difference vegetation index (GNDVI, weighted Difference vegetation index (WDVI), red edge NDVI (NDVIre), ratio-vegetation index (RVI), and normalised difference infrared index (NDII); VNIR— visible and near-infrared; VSWIR— visible and shortwave..... 56
Table 3.7: Confusion matrices for random forest (RF) models used to map crop types in North Darfur State, Sudan for 2022 growing season; SD—sand dunes, BS—bare soil, WB—water bodies, WV—woody vegetation, MI—millet, GN—groundnuts, VE—vegetables, TO—tobacco, GL—grassland. 10 Sentinel-2 (S2) bands used— B2, B3, B4, B5, B6, B7, B8, B8A, B11, B12; 8 vegetation indices (VIs) used— normalised difference vegetation index (NDVI), enhanced vegetation index (EVI), soil-adjusted vegetation index (SAVI), green-normalised difference vegetation index (GNDVI, weighted Difference vegetation index (WDVI), red edge NDVI (NDVIre), ratio-vegetation index (RVI), and normalised difference infrared index (NDII) 57
Table 3.8: Confusion matrices for support vector machine (SVM) models used to map crop types in North Darfur State, Sudan for 2022 growing season; SD—sand dunes, BS—bare soil, WB—water bodies, WV—woody vegetation, MI—millet, GN—groundnuts, VE—vegetables, TO—tobacco, GL—grassland. 10 Sentinel-2 (S2) bands used— B2, B3, B4, B5, B6, B7, B8, B8A, B11, B12; 8 vegetation indices (VIs) used— normalised difference vegetation index (NDVI), enhanced vegetation index (EVI), soil-adjusted vegetation index (SAVI), green-normalised difference vegetation index (GNDVI, weighted Difference vegetation index (WDVI), red edge NDVI (NDVIre), ratio-vegetation index (RVI), and normalised difference infrared index (NDII) 59

Table 3.9: The user and producer accuracy performance of random forest (RF) and support vector machine (SVM) using various datasets; SD—sand dunes, BS—bare soil, WB—water bodies, WV—woody vegetation, MI—millet, GN—groundnuts, VE—vegetables, TO—tobacco, GL—grassland, S2—Sentinel-2, VI—vegetation index, VNIR—visible and near-infrared, VSWIR—visible and shortwave, RF—random forest, SVM—support vector machine. 10 S2 bands used— B2, B3, B4, B5, B6, B7, B8, B8A, B11, B12; 8 VIs used— normalised difference vegetation index (NDVI), enhanced vegetation index (EVI), soil-adjusted vegetation index (SAVI), green-normalised difference vegetation index (GNDVI, weighted Difference vegetation index (WDVI), red edge NDVI (NDVIre), ratio-vegetation index (RVI), and normalised difference infrared index (NDII) 61
Table 3.10: F1 scores class-wise performance of random forest (RF) and support vector machine (SVM) algorithms using five different datasets; SD—sand dunes, BS—bare soil, WB—water bodies, WV—woody vegetation, MI—millet, GN—groundnuts, VE—vegetables, TO—tobacco, GL—grassland, S2—Sentinel-2, VI—vegetation index, VNIR—visible and near-infrared, VSWIR—visible and shortwave. 10 S2 bands used—B2, B3, B4, B5, B6, B7, B8, B8A, B11, B12; 8 VIs used—normalised difference vegetation index (NDVI), enhanced vegetation index (EVI), soil-adjusted vegetation index (SAVI), green-normalised difference vegetation index (GNDVI, weighted Difference vegetation index (WDVI), red edge NDVI (NDVIre), ratio-vegetation index (RVI), and normalised difference infrared index (NDII)..... 62
Table 4.1: Characteristics of weather stations in North Darfur State from which meteorological data used in this study was obtained. 72
Table 4.2: Drought and yield classification based on SPI, RDI, and SVCY values 76
Table 4.3: Interpretation of correlation coefficients 77
Table 4.4: The statistical trend test results for different timescales of SPI and RDI over the period 1981-2020 of the five districts. 80
Table 4.5: Statistical relationship between SVCY and drought trend using SPI and RDI. 81
Table 5.1: Description of the land use and land cover (LULC) classes in the study area. 93
Table 5.2: Area coverage in hectares of rainfed agriculture and other LULC classes for the period between 1984 and 2019. 100
Table 5.3: User and producer accuracies for mapping rainfed agriculture and other LULC classes for the period between 1984 and 2019 in five-year intervals. The accuracies were calculated using the test dataset (30%) and the confusion matrix. 101
Table 5.4: Change matrix of the rainfed agriculture and other LULC types in hectares of North Darfur State from 1984 to 1989. The bold values in the change matrix indicate unchanged land types between the initial and final years. 103

Table 5.5: Change matrix of the rainfed agriculture and other LULC types of North Darfur State in hectares from 1994 to 1999. The bold values in the change matrix indicate unchanged land types between the initial and final years. 104
Table 5.6: Change matrix of the rainfed agriculture and other LULC types of North Darfur State in hectares from 2004 to 2009. The bold values in the change matrix indicate unchanged land types between the initial and final years. 104
Table 5.7: Change matrix of the rainfed agriculture and other LULC types of North Darfur State in hectares from 2014 to 2019. The bold values in the change matrix indicate unchanged land types between the initial and final years.....105

List of abbreviations and acronyms

GDP:	Gross Demotic Product
SPPs:	Satellite Precipitation Products.
PMW:	Passive Microwave
TIR:	Thermal Infrared Radiation
TRMM:	Tropical Rainfall Measuring Mission
TMPA:	Multi-satellite Precipitation Analysis
ARC:	African Rainfall Climatology.
CHIRPS:	Climate Hazards Group Infrared Precipitation with Station Data
POD:	Probability of detection
POFA:	Probability of false alarm
BID:	Bias in detection
HSS:	Heidke skill score
RMSE:	The root mean square error
NSE:	Nash-Sutcliffe model efficiency coefficient
SPI:	Standardized Precipitation Index
RDI:	Reconnaissance Drought Index.
SVCY:	Standardized Variable of Crop Yield.
IDW:	Inverse Distance Weighting.
EOD:	Earth Observation Data
RS:	Remote sensing
ML:	Machine-Learning
LULC:	land Use and land Cover types.
MSS:	Landsat Multispectral Scanner (MSS)
TM:	Landsat Thematic Mapper (TM)
ETM^+:	Landsat Enhanced Thematic Mapper Plus
OLI:	Landsat Operational Landsat Imageries
ERDAS:	Earth Resources Data Analysis System.
ENVI:	Environment for Visualising Images
RF:	Random Forest.
OOB:	Out-Of-Bag data
SD:	Sand dunes
BS:	Bare Soil
PL:	Pasture Land
RG:	Rainfed Agriculture on Goz Land.
RW:	Rainfed agriculture on Wadi Land.
WB:	Water body
WV:	Woody vegetation
MI:	Millet Crop
GN:	Groundnut crop
VE:	Vegetable Crop
TO:	Tobacco Crop
GL:	Grass Land
NDVI:	Normalised difference vegetation index.
EVI:	Enhanced vegetation index.
SAVI:	Soil-adjusted vegetation index.
GNDVI:	Green-normalised difference vegetation index.
WDVI:	Weighted Difference vegetation index.
NDVIre:	Red-Edge Normalized Difference Vegetation Index.

RVI:	Ratio-vegetation index.
NDII:	Normalised difference Infrared index.
GEE:	Google Earth Engine .
SVM:	Support Vector Machines.
ML:	Machine Learning.
OA:	Overall Accuracy.
K:	Kappa
PA:	Producer’s Accuracies
UA:	Users Accuracies
RGB:	Red Green Blue

CHAPTER ONE

General introduction

1.1 Importance of rainfed agriculture

Rainfed agriculture plays a vital role in food security and income in most sections of the world (Devendra, 2012; Elagib *et al.*, 2019). One-third of the population in developing countries live in agricultural regions that are less favourable (Reddy *et al.*, 2014). Approximately 75-82% of the world's total cropland is used for rainfed agriculture, contributing over 60% of the globe's cereal grain production (Laux *et al.*, 2010; Molden *et al.*, 2011). In some areas, such as Sub-Saharan Africa, over 95% of cropland relies on rainfed agriculture, which depends on the physical environment and the variability and distribution of rainfall (Rockström *et al.*, 2010). Sudan heavily depends on rainfed agriculture, in which more than 90% of framing land covers rainfed cultivation, contributing to one-third of the GDP of the country and its associated livelihood to the Sudanese people (Siddig *et al.*, 2018; Siddig *et al.*, 2020a). Rainfed agriculture distributed east and west of the Nile River banks and tributaries provides 65% of the population's livelihood, employing 59% of males and 82% of females in rural Sudan. (Memorandum, 2015; Siddig *et al.*, 2018). Unfortunately, these lands are characterised by frequent droughts, unpredictable low rainfall, poorly distributed and highly variable monthly/ seasonal rainfall, population pressure, social change, deforestation, soil erosion/ salinisation, and water depletion (Ahmed *et al.*, 2011).

1.2 Impacts of spatio-temporal rainfall variability on rainfed agriculture

Rainfall is the main variable in the hydrological process. It is also a critical component to track climate variability and study natural disasters such as drought conditions, flood, and water erosion (Choubin *et al.*, 2019; Lu *et al.*, 2016). Moreover, rainfall is the key environmental constraint for ecological and biogeochemical processes, making it the most crucial climatic factor (Duhan *et al.*, 2013; Kaptué *et al.*, 2015). Rainfall amount, intensity, frequency and duration are the most important climatological variables for characterising the climate system of a region (Longobardi *et al.*, 2010; Mengistu *et al.*, 2020). The spatio-temporal variability in rainfall is the main factor influencing the function and structure of the arid environment ecosystem (Augustine, 2010; Knapp *et al.*, 2001). Factors such as altitude, distance from the sea, air pressure and geographical locations affect the spatial and temporal variation of rainfall (Grist *et al.*, 2001). Understanding rainfall variability is important for rainfed agriculture and wise water resource management (Gbangou *et al.*, 2020; Muchow *et al.*, 1991).

Climate variability has emerged as a leading threat to sustainable development due to its adverse impact on the environment, human health, food and water security, and socio-economic development (Gwambene, 2007; Koubi, 2019). Agriculture is one of the most weather-dependent sectors, and increasing evidence shows that climate variability significantly impacts agricultural production (Craparo *et al.*, 2015; Muthoni *et al.*, 2019). The impact is immense, especially in countries that primarily depend on agriculture, where a large proportion of the labour force is employed in agriculture, and agriculture contributes a large share of GDP (Siddig *et al.*, 2020a). Africa is one of the most vulnerable regions highly affected by climate variability and change—a complex web of stressors and low adaptive capacity has aggravated the situation (Asfaw *et al.*, 2018; IPCC, 2014). Over 75% of the livelihoods in Africa depend on rainfed agriculture, which is highly vulnerable to climate variability (Muthoni *et al.*, 2019; Ochieng *et al.*, 2016). The increased frequency of floods, droughts and heat waves significantly affects crops and ecosystems (Adhikari *et al.*, 2015). Crop yield is unreliable and difficult to predict (Rockström *et al.*, 2010; Sohoulande *et al.*, 2019). The variability in precipitation across space and time frequently exposes crops to brief water deficits, resulting in crop losses (Kistner *et al.*, 2018). Thus, understanding the spatio-temporal patterns of climate variability is crucial for designing and targeting suitable adaptation strategies.

In its fourth assessment report, the Intergovernmental Panel on Climate Change (IPCC) reported that the inter-seasonal, inter-annual, and spatial variability in precipitation during the past few decades has severely affected the environment and human activities across Africa (WG III, 2007). In the last three decades, Africa has experienced frequent food insecurity and water scarcity related to intra-annual rainfall variations, prolonged droughts and frequent droughts (Ngcamu *et al.*, 2020). The frequency, duration, and severity of the droughts will likely increase in many regions (Asadieh *et al.*, 2017; Meza *et al.*, 2021). Also, the combined impacts of climate variability and accelerated population growth will intensify drought risk, exposure and vulnerability in the long term (Ahmadalipour *et al.*, 2019). Climate variability already poses significant challenges to Sudan by declining agricultural yields, adversely affecting food security and rural incomes. Sudan is ranked as one of the most vulnerable countries in the world to the adverse effects of climate variability due to its dependence on rainfed agriculture, low adaptive capacity and a higher reliance on natural resources for livelihood (Dupree, 1977; Waithaka *et al.*, 2013). This emphasizes the importance of comprehensively understanding and effectively managing drought. Also, it is necessary to consider climate and environmental drivers along with socioeconomic factors that determine how susceptible a community, region, system or sector is to drought and their capacity to cope.

By 2050, agricultural production will require to increase by 60-110% to meet the increasing demand for food worldwide (Siddig *et al.*, 2020a). Several authors have suggested that increasing crop yields, rather than clearing more land for food production, is the most sustainable path for food security (Foley *et al.*, 2011; Godfray *et al.*, 2010; Phalan *et al.*, 2011). Unfortunately, some studies indicate that crop yields are no longer increasing in various regions of the world (Cassman, 1999; Ray *et al.*, 2012). Many of these regions are in Africa (Pretty *et al.*, 2012). The world's poorest areas will continue to face the potential impacts of climate fluctuations like droughts and floods on food security, leading to significant instability and reductions in food production (Lobell *et al.*, 2011).

1.3 Monitoring and mapping rainfed agriculture using Earth Observation Data

Rainfed agricultural lands are continuously changing at global and regional scales due to human activities and climatic variability (Waldner *et al.*, 2016). Understanding the spatio-temporal dynamics of cropland plays an important role in regularly monitoring rainfed agriculture production, and supporting land management and understanding the environmental impacts of agricultural land (Hao *et al.*, 2018). The spatial distribution of cropland information is essential for various applications (Yan *et al.*, 2014). In Africa, cropland information is commonly generated by agricultural ministries through agricultural census—data acquired this way provides no information on the spatial distribution of cropland (Forkuor *et al.*, 2017).

Accurate monitoring of rainfed agriculture land is essential in a better understanding of agriculture management and agriculture precision (Abdel-Rahman *et al.*, 2008). Timely analysis of cropland can provide objective information for decision-making in agricultural management, food security early warning, and food allocation in the region (Bofana *et al.*, 2020). In North Darfur, the spatial and temporal rainfall variability aggravates the problem of limited soil productivity and the spatial distribution of agricultural lands (Siddig *et al.*, 2020b), —therefore, climate-related hazards, e.g., drought, have severe effects on poor rural people, because crop yields are unpredictable this combination issues occasionally led to violent clashes between nomadic tribes and local farmers (Osman *et al.*, 2014). Understanding and monitoring the spatio-temporal of rainfed agriculture dynamics and its determining climatic factors in the study area can play a main role in socio-political stability and promoting food security , as well as in protecting and restoring ecosystem services (De Marinis *et al.*, 2021). Moreover, mapping and monitoring rainfed agriculture remains a challenge in North Darfur due to political unrest and conflicts among communities, significantly influencing the spatial

distribution of rainfed agriculture, and insufficient ground data, which often shows gaps in crop data (Ibrahim, 1984; Kevane *et al.*, 2008). Historically, field-based assessment surveys, expert-scouting estimates, and crop cut information were the main approaches for monitoring agriculture (Kolecka *et al.*, 2018). However, many studies have shown that these methods pose extreme danger to field teams, are time consuming and involve significant costs, and are not feasible for large-scale agricultural landscape monitoring (Chabalala *et al.*, 2023; Ouzemou *et al.*, 2018).

Nowadays, timely and accurate production forecasts and near-real-time agricultural monitoring can be done using RS techniques (Kyere *et al.*, 2019). Satellite remote sensing (RS) offers tremendous potential in several technical-scientific fields. Remote sensing (RS) has been used worldwide to monitor changes in the environment (Orusa *et al.*, 2020). Remote sensing (RS) has been an effective tool for monitoring rainfed land in many locations around the world under various environmental conditions (Huete *et al.*, 2002).

Numerous studies have aimed to obtain accurate cropland mapping using various satellite RS images (Bofana *et al.*, 2020; Gislason *et al.*, 2006; Praticò *et al.*, 2021; Xiong *et al.*, 2017). The applications of different RS technologies for agriculture land monitoring are crucial and efficient tools to help map and monitor spatio-temporal agricultural land dynamics for sustainable planning and management in various studies (Bai *et al.*, 2016; Sinha *et al.*, 2022). MODIS satellite data has been extensively used in crop mapping and monitoring at regional and global scales (Gilbertson *et al.*, 2017). However, the efficiency of testing MODIS data in mapping rainfed agriculture lands is limited (Qader *et al.*, 2021). According to Yin *et al*.(Yin *et al.*, 2018), medium-resolution Landsat imagery provides a great opportunity to map agricultural dynamics. High-resolution RS data (< 10 m), i.e., Worldview, Sentinel-2 and SPOT imageries, were used to overcome the issue of spectral mixing and improve crop mapping in agricultural land at a minor scale (LUO *et al.*, 2020). The application of very-high spatial resolution data has been widely used in determining accurate site-specific geospatial information for agriculture decisions (Rao *et al.*, 2021). Still, the application of RS for agriculture planning and sustainable management in North Darfur is limited due to a myriad of challenges.

In order to attain agriculture planning, development and sustainable management, this study aimed to explore spatio-temporal rainfed agriculture patterns using intermediate-resolution spatial multitemporal Landsat images and high-resolution multispectral Sentienl-2 data, Satellite precipitation products, Google Earth, Google Earth Engine and historical rainfall and yield data. The study provides an in-depth understanding of rainfall variability and related

impacts such as land cover patterns change and unpredictable crop yields on rainfed agriculture land patterns in semi-arid North Darfur State. This will aid in water resources management, land use/ land cover (LULC) planning, land degradation management, and drought preparedness.

1.4 Statement of the study problem

North Darfur State is Semi-arid environment, with great geographical and spatio-temporal variability in rainfall (Atiem *et al.*, 2022; Mohmmed *et al.*, 2018). North Darfur has been characterized as a focal point of environmental decline, facing some of the most significant natural challenges in the area. Additionally, it encounters considerable variability in rainfall patterns and enduring periods of drought (Osman, 2012; Osman, 2017). Rainfed agriculture is the essential for local livelihood for about 80—90 % of North Darfur communities, yet it faces significant challenges from climate variability (Siddig, 2010; Siddig *et al.*, 2020a; Young *et al.*, 2005). Therefore, rainfed agriculture is vulnerable to climate-hazards, including variability the crop yields is unreliable and difficult to predict. Nevertheless, the increasingly irregular rainfall patterns and temperature fluctuations threaten the sustainability and productivity of agricultural practices in this region (Osman *et al.*, 2013; Siddig *et al.*, 2020a). The Darfur region in Sudan faces heightened fluctuations in rainfall, resulting in frequent droughts and crop failures (Atiem *et al.*, 2022; Elhag *et al.*, 2018). Moreover, the Darfur region faces resource-related conflicts emanating from droughts, which have led to desertification and land degradation, thus severely reducing the area of arable land available for the farming and grazing of livestock (Karamalla-Gaiballa *et al.*, 2021). Studying the spatio-temporal dynamics of rainfed agriculture and identifying the climatic factors that influence it in the region can significantly enhance food security, socio-political stability, and the preservation of ecosystem services and the region characterised by the lack of availability of spatial data for monitoring trends in rainfed agriculture (De Marinis *et al.*, 2021; Elagib *et al.*, 2021). Due to political instability in certain areas of the study region, conventional agricultural monitoring methods such as expert scouting estimates, crop cut data collection, field assessments, and surveys not only pose serious risks to field teams but also entail substantial financial expenses (Mohmmed *et al.*, 2018; Nakalembe *et al.*, 2021).

Nowadays, most of these events can be predicted, and data and tools can provide early warning and impact assessment; this underscores the importance of timely and accurate production forecasts and near-real-time agricultural monitoring (Sahajpal *et al.*, 2020) Satellite

remote sensing (RS) offers useful analysis tools in several technical-scientific fields and has been used widely worldwide for monitoring the changes that occur in the environment and the identification of their magnitude at different space-temporal resolutions (Carella *et al.*, 2022; Orusa *et al.*, 2020). In North Darfur, the efforts to mitigate these challenges of spatial and temporal assessments using high-resolution satellite data, such as Observation Earth data, combined with Geographic Information Systems (GIS), are limited. There is a critical need to systematically map and monitor the specific impacts of climate variability on rainfed agriculture using advanced remote sensing technologies and spatial analysis tools. By addressing this gap, the study aims to provide actionable insights for adaptive management strategies that enhance the resilience of rainfed agriculture in North Darfur State, thereby supporting sustainable development and food security in the face of changing climatic conditions.

1.5 Research Aim and objectives

This research mainly aimed to use multi source remote sensing (RS) dataset accompanied by various machine-learning (ML) algorithms to understanding the spatio-temporal dynamics of rainfed agriculture in extreme climate conditions in semi-arid North Darfur State, Sudan for the period from 1984 to 2019

The specific objectives of this study were:

1. To evaluate the feasibility of satellite precipitation products (SPPs) in estimating the spatio-temporal rainfall variability across North Darfur State, Sudan from 2000 to 2019
2. To map crop types in a highly heterogeneous semi-arid environment using Sentinel-2 datasets and machine learning (ML) algorithms on the Google Earth Engine (GEE) cloud for the 2022 growing season
3. To analyse spatio-temporal drought trends and impact on millet crop production across North Darfur State using standardized precipitation index (SPI) and reconnaissance drought index (RDI) from 1981 to 2020
4. To map and monitor spatio-temporal patterns of rainfed agricultural lands of North Darfur State, Sudan, using earth observation data (EOD) for the period from 1984 to 2019

1.6 Scope of the study

The study aimed to map and monitor the impacts of rainfall variability on rainfed agriculture patterns in the semi-arid environment of North Darfur State, Sudan, using multitemporal and multispectral RS data. Six SPPs were used to estimate the spatio-temporal variability of rainfall and its impact on rainfed agriculture. The effeteness of spectral features from the high-resolution Sentienl-2 imagery and vegetation indices extracted from Sentinl-2 bands were used to map crop types in a highly heterogeneous semi-arid environment using RF and SVM classification algorithms on Google Earth Engine cloud. The study compared the performance of two drought indices: the standardized precipitation index (SPI) and reconnaissance drought index (RDI), to detect drought events and their impact on millet yield from 2000 to 2019. The potential of the multitemporal Landsat dataset is evaluated in mapping and monitoring rainfed agriculture on a random forest classification model.

The study collected 250 ground control points of the rainfed agriculture in August 2020, and 250 GCPs for the different crops in the field in June–September 2022 using a hand-held Global Positioning System (eTrex® 20 GPS Receiver; Garmin, Olathe, KS, USA) . Because North Darfur State is expansive, the remaining sample data were generated via on-screen digitization on Google Earth, collected 750 GCPs multitemporal Landsat and collected 850 GCPs from Sentinel-2 MSI images, closely guided by visual interpretation, knowledge of the study area, and expert opinion.

1.7 The study area

This study carried out in the North Darfur State, the State is situated in western Sudan on the northern transitional margin of the Inter Tropical Convergence Zone at latitude 11° 45′ 49″-20° 00′ 30″ N and longitude 22° 46′ 47″-27° 29′ 47″ E as shown in (Figure 1.1). The State covers about half the territory of the Darfur region—it borders West Darfur, South Darfur, East Darfur, Central Darfur, Northern, West Kordofan, and North Kordofan states (Young *et al.*, 2005). In addition, North Darfur has a common border with Chad and Libya. The state occupies an area of *c*. 296,420 km^2 and an estimated population of 2.8 million in 2021 (Karamalla-Gaiballa and El-Kafafi, 2021). The Mara Range (*Jebel Mara)* is the highest mountain in Sudan (Elagib, 2009; Young *et al.*, 2005; Zakieldeen, 2009). The region is mainly semi-arid environment, with great geographical and spatio-temporal variability in rainfall. Most rainfall of North Darfur comes from south-westerly winds and the rainy season is mainly from June to October, with average yearly rain ranging between 152 mm yr^{-1} in the northern parts and 540 mm yr^{-1} in the

southern parts and the rainfall is at its peak in August, the rainy season may comprise a large number of dry days and a small number of heavy but short rainstorms (Mohmmed *et al.*, 2018).

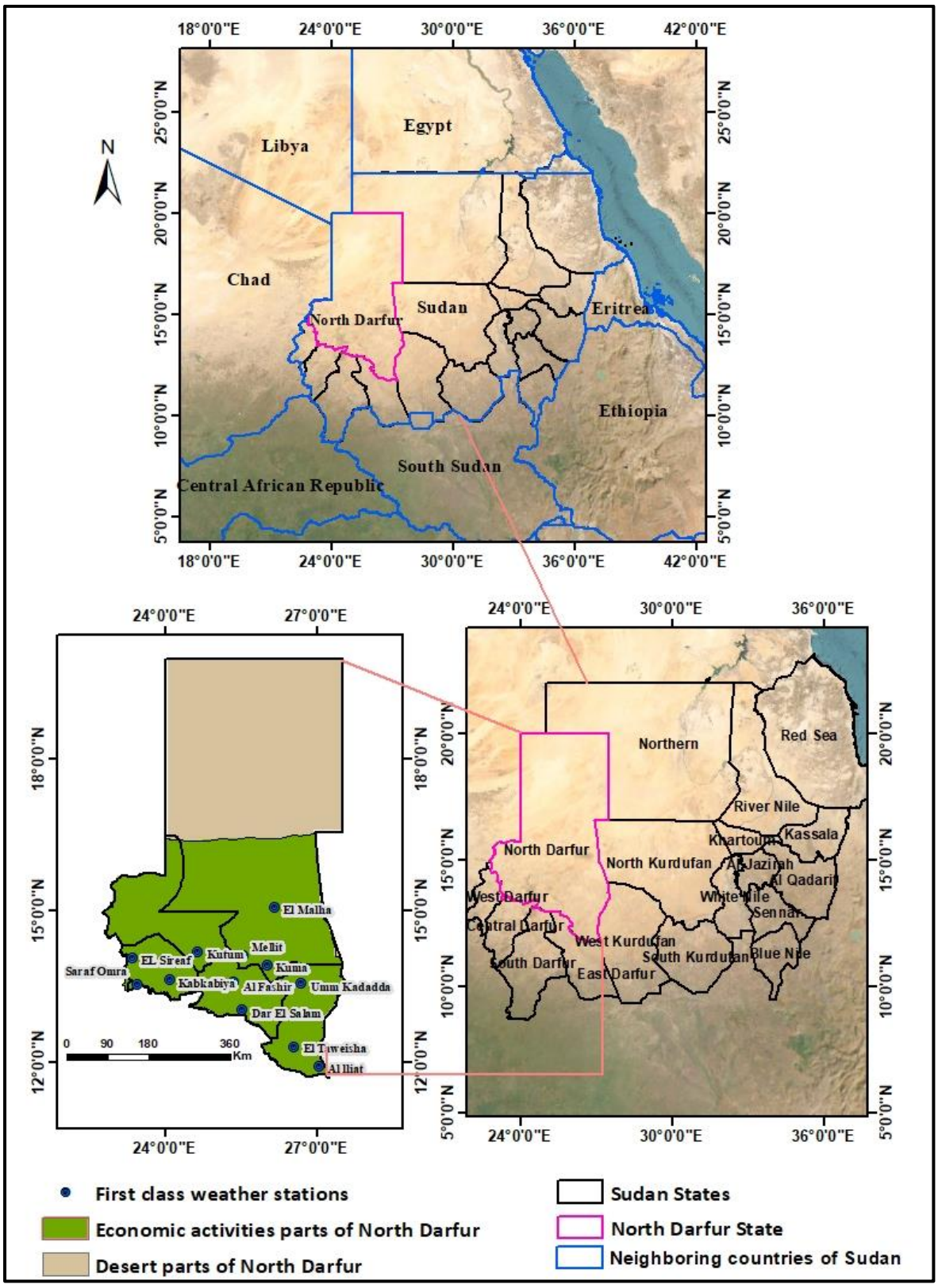


Figure 1.1. Map of the study area showing districts and distribution of first class weather stations in North Darfur State, Sudan and neighbouring countries of Sudan.

During May and June, temperatures regularly rise over 42 °C—in January, temperatures drop below 11 °C (Elagib, 2009; Young *et al.*, 2005). Rainfed agriculture is the primary livelihood for about 80% of the population in Darfur, and rain-fed millet, a drought-resistant crop planting on goz land, serves as a major food and cash crop, the soils in North Darfur State are predominantly characterized by sandy soil types (GOz), with occasional patches of clay soil found in the beds of seasonal valleys (wadis) (Siddig, 2010; Young *et al.*, 2005). Unfortunately, rainfall variability in space and time significantly impacts on agricultural sector. As a result, climate-related risks are a concern for the region's rainfed agriculture, and crop yields are unpredictable and difficult to anticipate (Abdelaziz *et al.*, 2012; Håland, 1991; Osman and Cohen, 2014). Nevertheless, irrigated agriculture is practiced to cultivate multiple vegetables on small plots of wadi land. These crops are grown in saturated alluvial wadi soil, with occasional use of shallow wells for irrigation (El-Amin, 2002).

North Darfur has been described as a hotspot of environmental degradation, experiencing among the most prominent natural threats in the region. Also, the region experiences high rainfall spatio-temporal variability and persistent drought (Osman *et al.*, 2013). Persistent security threats in the region due to conflicts among communities and political unrest significantly impact the distribution of rain gauge measurements (Ibrahim, 1984; Kevane and Gray, 2008). The population of North Darfur State has increased since 1973 from 530,000 to 1.15 million to 2.8 million in 2021, and the population density increased from 8/km^2 to 23/km^2 (Karamalla-Gaiballa and El-Kafafi, 2021; Schimmer, 2008). As the population increased, agricultural land conversion into pasture land caused clashes and friction between different communities. Additionally, as farmers sought to expand their farms to obtain the crops needed to feed more people, it led to soil erosion and decreased land productivity (Bushra *et al.*, 2000; Osman, 2012).

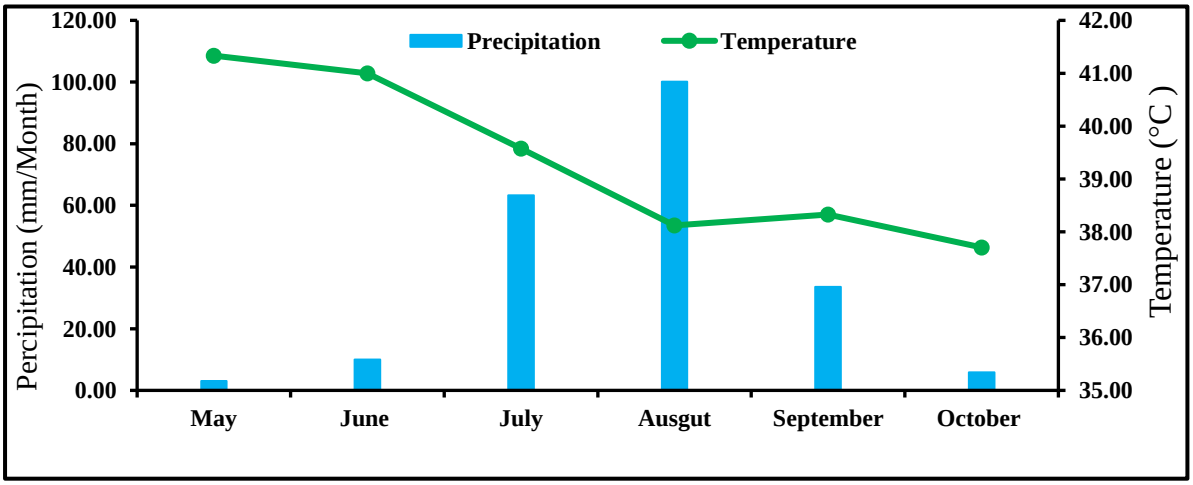


Figure 1.2. The meteorological climate data of the North Darfur State, Sudan; mean monthly rainfall and mean monthly temperature for the period 2000 to 2019 the data were average from whole climatic stations.

In recent decades, the North Darfur region has experienced increasing rainfall variability, causing an increase in the frequency and severe droughts resulting in several cycles (Fuller, 1987b; Sayed *et al.*, 2013).

1.8 Thesis overview

This thesis aims to achieve the main objectives of this study through four research papers that have been submitted to international peer-reviewed journals—one of which has already been published, two are being reviewed, and the other one is being prepared for journal submission. Each was written as a stand-alone article that can be read independently of the other parts of the thesis but draws separate conclusions that are linked to the overall research objectives and questions. As a result, there are overlaps and replications in the sections "Introduction" and "Method" in the various chapters. When one considers the rigorous peer-review procedure and the fact that the various chapters are papers that can be read independently without losing the overall context, this problem is of relatively minor importance. The thesis is divided into six chapters.

Chapter two evaluates the applications feasibility of satellite precipitation products (SPPs) in capturing the spatio-temporal rainfall variability across North Darfur State, Sudan. The chapter focused on download raster files of six SPPs from their websites—the TMPA 3B42/3B43-7.0, CHIRPS 2.0, PERSIANN-CDR, GPMIMERG 6.0, ARC 2.0, and TAMSAT 3.1, then the point values from pixels of respective SPPs were georeferenced to rain gauge location and using Spatial Analyst tools for the extraction from the download raster files. Then the chapter employed a point-pixel pairwise comparison SPPs against rain gauge measurements for the 2000-2019 period at daily, monthly and annually timescale to identify the best products for capturing rainy days and estimating rainfall amounts and variability trends across the study area. However, the rain gauge observations have been disrupted owing to unstable security conditions and conflicts. Therefore, accurately estimating and predicting rainfall trends has been challenging.

Chapter three involved mapping crop types over North Darfur State, Sudan using Sentinel-2 (S2) datasets and ML algorithms on the Google Earth Engine GEE cloud. The chapter performance the RF and SVM using multispectral Sentienl-2 data to mapping cropland types in high heterogeneous semi-arid environment under open canopy rainfed agriculture.

Eight vegetation indices were extracted from Sentienl-2 bands used for mapping and compared the results to determining better dataset for mapping cropland in the study area.

Chapter four analysed the spatio-temporal drought trends using widely two drought indices based on meteorological data; standardized precipitation index (SPI) and reconnaissance drought index (RDI) at three timescales and its impact on millet crop production using Preseason correlation coefficient (r) across North Darfur State. The Darfur region experiences exacerbated variability in rainfall, leading to frequent droughts and crop failure. Therefore, the SPI and RDI were used to detect drought events between 1981 and 2020 and investigate the impacts of drought events on millet production from 1998 to 2020. Millet crop is highly relied upon for food security and nutrition by in North Darfur. The chapter also evaluated the performance of the two indices for monitoring drought during the last 40 years.

Chapter five was about mapping and monitoring spatio-temporal patterns of rainfed agricultural lands of North Darfur state using earth observation data. The chapter used four medium-resolution multitemporal Landsat sensors—Multispectral Scanner (MSS) at 60 m resolution acquired in 1984; Landsat Thematic Mapper (TM) at 30 m resolution acquired in 1989, 1994, and 1999; Landsat Enhanced Thematic Mapper Plus (ETM^{+}) at 30 m resolution acquired in 2004 and 2009; and Landsat Operational Landsat Imageries (OLI) at 30 m resolution acquired in 2014 and 2019 for monitor and map rainfed agriculture for the 1984 to 2019. Rainfed agriculture and livestock are the primary sources of livelihood for 80-90% of the population of the Darfur region. This crucial agriculture sector usually depends on the physical environment and, most importantly, the amount and distribution of rainfall. Therefore, rainfed agriculture is vulnerable to climate-related hazards, including variability, and the crop yield is thus unreliable and difficult to predict. Persistent drought and associated impacts on rainfed agricultural practices contribute to regional social and/ or political instability.

Chapter six provides a synthesis of the study and the summary of the outcomes. It outlines the main contributions of this research to the identification, mapping and monitoring of rainfed agriculture. In this chapter, the limitations of the current study are outlined, and it gives an outlook into other research aspects that can be considered in further studies.

At the end of the thesis, a single reference list from all the chapters is provided

CHAPTER TWO

Evaluating Satellite Precipitation Products in Capturing the Spatio-temporal Rainfall Variability across North Darfur State, Sudan

This Chapter based on:

Altoom, M.B., Adam, E., & Ali, K.A. (in review). Evaluating Satellite Precipitation Products in Capturing the Spatio-temporal Rainfall Variability across North Darfur State, Sudan

Abstract

Accurate rainfall measurement is vital when investigating spatio-temporal precipitation variability on agriculture, ecosystem and hydrological modelling for water management, especially in semi-arid lands. However, there are many regions worldwide where only a few ground-based observations are made available. Therefore, a comparative assessment of satellite precipitation products (SPPs) is vital. This research aimed to evaluate the accuracy and applicability of six SPPs in the North Darfur State in Sudan, i.e., the Tropical Rainfall Measuring Mission "…(TRMM)…". Multi-satellite Precipitation Analysis (TMPA), African Rainfall Climatology (ARC), Climate Hazards Group Infrared Precipitation with Station Data (CHIRPS), Integrated Multi-satellitE Retrievals for Global Precipitation Measurements "…(GPM) Final Run (GPMIMERG)…", Precipitation Estimation from Remote Sensing Information using Artificial Neural Networks-Climate Data Record (PERSIANN-CDR), and the Tropical Applications of Meteorology using SATellite and ground-based observations "…(TAMSAT)…". Four categorical indices, i.e., the probability of detection (POD), probability of false alarm (POFA), bias in detection (BID) and Heidke skill score (HSS), and four continuous indices, i.e., the Pearson correlation coefficient (r), the root mean square error (RMSE), the per cent bias (Pbias), and the Nash-Sutcliffe model efficiency coefficient (NSE) were used to evaluate the accuracy of the SPPs. The global-based SPPs were assessed at daily, monthly and annual timescales by applying a point-to-pixel comparison with ground-based rain gauge data for the period 2000–2019. The overall results of the statistical analysis showed that: 1) at the daily timescale, the SPPs underestimate daily rainfall by 6.53–17.61%, and CHIRPS was the best for detecting rainy days, while PERSIANN-CDR performed poorly, 2) monthly and annual scales performed better than daily timescale, and TAMSAT and CHIRPS portrayed better performance than the other SPPs, therefore, the two could reasonably estimate rainfall amounts in North Darfur State.

Keywords: in situ rainfall data, ARC2.0, CHIRPS, GPMIMERG6, PERSIANN-CDR, TMPA, validation statistics, North Darfur State

2.1 Introduction

Rainfall is vital to how water moves through Earth's water cycle, which connects the land, atmosphere and oceans (Choubin *et al.*, 2019) therefore, rainfall are essential in Earth's climate system (Duhan and Pandey, 2013; Wedajo *et al.*, 2021). Rainfall is not evenly distributed worldwide—some places receive more than normal, while others become prone to droughts (Maidment *et al.*, 2017). The variable distribution, rate and amount of rainfall determines Earth's ecosystems (Ayehu *et al.*, 2018; Stillman *et al.*, 2014). Reliable measurement of rainfall data is essential for understanding the spatio-temporal variability of rainfall at various timescales and its effects on hydrology, agriculture and ecosystem functioning (Asfaw *et al.*, 2018; Ayehu *et al.*, 2018; Brocca *et al.*, 2016). Traditionally, rain gauge observations have been used to characterise the spatio-temporal variability of rainfall (Zambrano-Bigiarini *et al.*, 2017a). However, in developing countries, due to various reasons, rainfall data is often unavailable, and even if it does exist, the quality are poor or inaccessible (Field *et al.*, 2014). For example, the Meteorological Department of Sudan does not receive sufficient funding from the government; this has hampered the recruitment and retention of trained and volunteer observers and the ability to rehabilitate malfunctioned and/or abandoned meteorological stations (Ibrahim, 1984; Zakieldeen, 2009). In addition, the second Sudanese Civil War between 1983 and 2005 interfered with measuring and reporting meteorological data, especially in the southern region (Abd Elhamid *et al.*, 2020; Elhag and Zhang, 2018; Osman *et al.*, 2002). Therefore, political unrest and conflict significantly influenced the distribution, density and quality of rain gauge measurements. It is particularly true in the Darfur region, which often shows gaps in temporal rainfall data (Ibrahim, 1984; Kevane and Gray, 2008).

The limitations associated with rain gauge observations have necessitated alternative methods to measure rainfall (Maidment *et al.*, 2017). Fortunately, remote sensing provides an alternative approach to ground-based rainfall measurement and monitoring methods. Rainfall data can be gathered from satellite-based products (Ayehu *et al.*, 2018). A variety of satellite precipitation products (SPPs) are produced by the passive microwave (PMW) and thermal infrared radiation (TIR) sensors onboard low-Earth orbiting and geostationary satellites, respectively. The TIR-based method uses algorithms to assess rainfall from cloud-top temperature (Paredes Trejo *et al.*, 2016). The PMW technique can penetrate clouds and produce accurate rainfall amounts compared to the TIR-based technique, which has difficulties

identifying rain-producing clouds (Ageet *et al.*, 2022; Kidd *et al.*, 2011). However, the poor temporal resolution of low Earth-orbiting satellites makes the PMW technique not helpful in assessing accumulated rainfall over a longer duration (Toté *et al.*, 2015). Therefore, uncertainties may originate from the temporal resolutions of satellites, the algorithms used to assess rainfall from cloud-top temperature, and satellite instruments themselves—these reduce the accuracy of satellite rainfall estimates (Gebremichael *et al.*, 2005). Other techniques, e.g., combined PMW/TIR (Di Paola *et al.*, 2012) or merged PMW/TIR technique with rain gauge observations or numerical weather models (Usman *et al.*, 2018) were developed to enhance the accuracy of satellite rainfall assessment. Several studies, i.e., Huffman *et al*. (Huffman *et al.*, 1997), Xie *et al* (Xie *et al.*, 1998), Boushaki *et al*.(Boushaki *et al.*, 2009), Ebert *et al*.(Ebert *et al.*, 2007), Katiraie-Boroujerdy *et al*.(Katiraie-Boroujerdy *et al.*, 2017), Sanogo *et al*. (Sanogo *et al.*, 2015), Dezfuli *et al*. (Dezfuli *et al.*, 2017), Bai *et al*. (Bai *et al.*, 2019), Dembélé and Zwart (Dembélé *et al.*, 2016) and Ayugi *et al*. (Ayugi *et al.*, 2016) have been conducted using the latter technique at different spatial and temporal scales.

The SPPs play a vital role in accurately mapping the spatiotemporal variability of rainfall, which is essential in designing climate change adaptation strategies. Sanogo *et al*. (Sanogo *et al.*, 2015) evaluated the spatio-temporal characteristics of rainfall in West Africa using the gridded African Rainfall Climatology Version 2 (ARC 2.0). The results were consistent with ground-gauge observation rainfall. Dezfuli *et al*. (Dezfuli *et al.*, 2017) showed that the diurnal precipitation cycle was better captured by the Integrated Multi-satellitE Retrievals for Global Precipitation Measurement (IMERG)-Final v6 (IMERG6) than the TRMM (Tropical Rainfall Measuring Mission) Multi-satellite Precipitation Analysis- TMPA, and the products exhibited a better agreement with ground data in dry East and humid West Africa than with the southern Sahel. The Usman *et al.* (Usman *et al.*, 2018) analysis assessed the capability of four satellite-based rainfall models, i.e., TAMSAT (Tropical Applications of Meteorology using SATellite) African Rainfall Climatology and Time series- TARCAT, ARC 2.0, TRMM, and Climate Hazards group Infrared Precipitation with Stations (CHIRPS) to portray rainfall trends in West Africa. Additionally, Dembélé and Zwart. (Dembélé and Zwart, 2016) evaluated how well the TRMM, ARC 2.0, CHIRPS 2.0, Precipitation Estimation from Remote Sensing Information using Artificial Neural Networks (PERSIANN), African Rainfall Estimation (RFE 2.0), TAMSAT, and TARCAT performed at estimating rainfall amounts in the semi-arid Sahelian area in Burkina Faso. The satellites performed poorly at daily time scales but better at annual timescales, with the best product being the RFE 2.0. The CHIRPS 2.0 and

TARCAT were the best products for assessing drought in the Upper Blue Nile Basin of Ethiopia, according to Bayissa *et al.* (Bayissa *et al.*, 2017)—the study compared the capabilities of five satellite precipitation products, i.e., ARC 2.0, CHIRPS 2.0, PERSIANN, TARCAT 2.0 and TMPA. Toté *et al.* (Toté *et al.*, 2015) analysed three satellite rainfall estimates i.e., TARCAT 2.0, Famine Early Warning System NET work (FEWS NET), RFE 2.0, and CHIRPS 2.0 for drought and flood monitoring in tropical climate areas of Mozambique—TARCAT 2.0 was superior at modelling the relative frequency of rainfall events. Ahmed *et al.* (Ahmed *et al.*, 2020) evaluated TRMM and RFE 2.0 over the Sudanese portion of the Blue Nile River and found that the TRMM product performance was superior to RFE 2.0. Girm,(Girma, 2021) explored TAMSAT 3.1 over southern Ethiopia and demonstrated that TAMSAT matched rain gauge data. Lu *et al.* (Lu *et al.*, 2016) evaluated the SPPs in analysing changes in rainfall patterns in Namibia and found that the TMPA estimations and the data from the rain gauges agreed at monthly and annual timescales. Babaousmail *et al.* (Babaousmail *et al.*, 2019) showed that the National Oceanic and Atmospheric Administration (NOAA) Climate Prediction Center Morphing Technique (CMORPH) was the most suitable product for satellite-based precipitation estimates for the prevailing Mediterranean climate. However, the majority of the aforementioned studies demonstrated that the algorithm performance varies significantly depending on topography, location, season and local climate (Abd Elhamid *et al.*, 2020; Maidment *et al.*, 2013; Toté *et al.*, 2015; Usman *et al.*, 2018).

The North Darfur region is characterised by spatio-temporal rainfall variability. The variability aggravates the problem of limited soil productivity and the spatial distribution of agricultural land. Despite these challenges, 80%–90% of the population relies on rainfed agriculture and livestock rearing as their main sources of income (Osman, 2012; Siddig *et al.*, 2020b). Therefore, climate-related hazards, e.g., drought, have severe and disproportionate effects, especially on the rural poor, because crop yields are unpredictable and difficult to anticipate. The Sahel region's devastating droughts and hunger in the 1970s, 1980s and mid-1990s, particularly in Chad and Sudan's Darfur region, occasionally led to violent clashes between nomadic tribes and local farmers (Brauch, 2006). Therefore, understanding the spatio-temporal variation in rainfall, especially in arid and semi-arid regions, is critical for predicting extreme hydrological events and mitigating climate-related risks through improved water resources planning, agricultural development of agro-pastoral systems and environmental management and restoration (Elagib *et al.*, 2021).

Hydrological modelling for water management in arid and semi-arid lands requires accurate spatio-temporal rainfall measurements. However, mostly, only a few ground-based observations are available. Therefore, SPPs can fill the spatio-temporal rainfall data gaps in such regions. Satellite precipitation products have performed differently in mapping the spatio-temporal variability of rainfall. Hence, accurately detecting rainfall variability and trends has been challenging. This study aimed to determine whether it is feasible to estimate rainfall variability across North Darfur State at daily, monthly and annual timescales using SPPs to inform decisions in water management. No relevant studies have been carried out in the North Darfur State. The SPPs used were the TRMM (Tropical Rainfall Measuring Mission) Multi-satellite Precipitation Analysis (TMPA), African Rainfall Climatology (ARC), Climate Hazards group Infrared Precipitation with Stations (CHIRPS), Integrated Multi-satellitE Retrievals for Global Precipitation Measurements (GPM) Final Run (GPMIMERG), Precipitation Estimation from Remote Sensing Information using Artificial Neural Networks-Climate Data Record (PERSIANN-CDR), and Tropical Applications of Meteorology using SATellite and ground-based observations (TAMSAT).

2.2 Materials and methods

2.2.1 The study area

The study area is situated in North Darfur State in western Sudan, at latitude 11° 45′ 49″-20° 00′ 30″ N and longitude 22° 46′ 47″-27° 29′ 47″ E (Figure 2.**Error! Reference source not found.**). The southern part of North Darfur state comprises a higher concentration of population and economic activities. The Jabbed Marrah Mountains roughly at 3,000 m above sea level, are at the maximum elevation within the study area (Osman, 2012; Osman and Cohen, 2014). The region is mainly semi-arid environment, with great geographical and temporal variability in rainfall. Most rainfall of North Darfur comes from south-westerly winds and the rainy season is mainly from June to October, with average yearly rain ranging between 152 mm yr^{-1} in the northern parts and 540 mm yr^{-1} in the southern parts and the rainfall is at its peak in August (Ibrahim, 1984; Kevane and Gray, 2008). In North Darfur State, Sudan, the rainy season may comprise a large number of dry days and a small number of heavy but short rainstorms. The few rainy days may take the following forms: (i) rain may start early, followed by partial/complete failure, (ii) rain may start late, (iii) the few rainy days may spread

throughout the wet season, and (iv) evenly-distributed but infrequent heavy rainfall. Yearly mean maximum and mean minimum temperatures are 42 °C and 11 °C respectively (Mohmmed *et al.*, 2018).

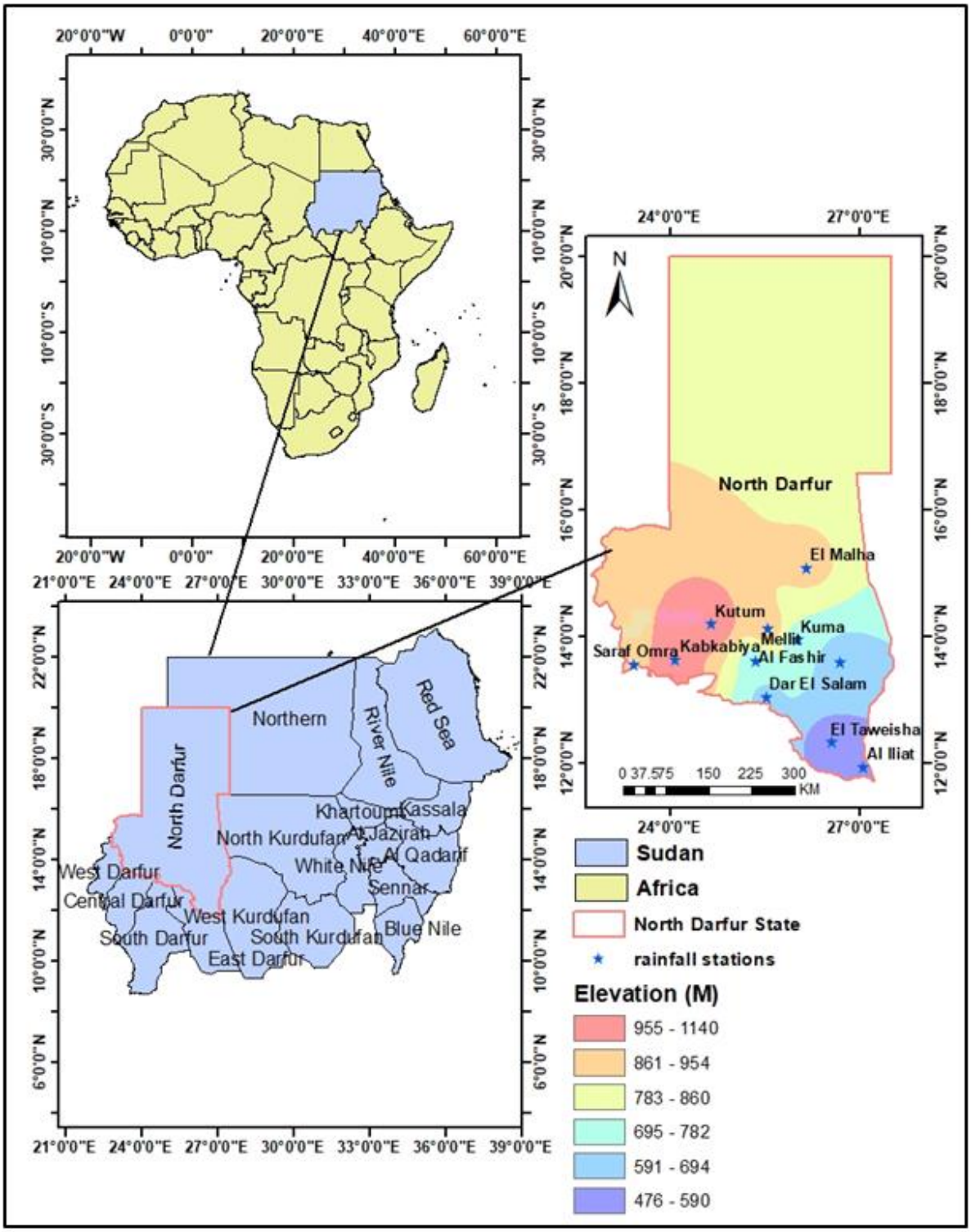


Figure 2.1. Map of the study area in North Darfur State in Sudan; the star symbol shows locations of the11 first class rainfall stations (meteorological data).

The largest food crop is millet, *"…grown in sandy soil (qoz) …"* (Siddig, 2010; Young *et al.*, 2005). Agriculture is constrained by poor soil fertility, small per capita landholding, soil degradation and erratic rainfall; as a result, most parts of the area are chronically food insecure (Osman, 2012).

2.2.2 Datasets

2.2.2.1 In situ rainfall data

Daily rainfall data from 2000 to 2019 from 11 rainfall stations were obtained from the North Darfur State Ministry of Agriculture (Figure 2.**Error! Reference source not found.**). The rainfall stations in the study area are located in densely populated areas in south-western parts, especially in areas of intense agricultural activity, because the northern parts of the North Darfur State is mostly desert (Ibrahim, 1984; Mohmmed *et al.*, 2018). Only less than 10% of rainfall data were missing at each of the 11 weather stations considered in this study were infilled using the modified inverse distance weighting (IDW) method (Organization, 2017; Taye *et al.*, 2023; Zambrano-Bigiarini *et al.*, 2017a). A brief description of the 11 rainfall stations is presented in Table 2.1 for the period from 2000 to 2019. The stations are installed at different elevations and have been recording data since 1970 to now.

Table 2.1: Characteristics of the 11 first class rainfall stations in North Darfur State for the study period 2000–2019.

No.	Station name	Latitude (°N)	Longitude (°E)	Elevation (amsl)	Data availability	Mean annual rainfall (mm)
1	Al Fashir	13° 38'	25° 20'	0740	Daily	232.3
2	Al Liait	11° 57'	27° 04'	0587	Daily	517.1
3	Dar El Salam	13° 05'	25° 53'	0817	Daily	302.2
4	El Malha	15° 09'	26° 15'	0900	Daily	211.7
5	El Tawiesha	12° 29'	26° 59'	0591	Daily	363.4
6	Kabkabiya	13° 39'	24° 5'	1120	Daily	558.6
7	Kuma	13° 39'	26° 01'	0875	Daily	220.2
8	Kutum	14° 21'	24° 40'	1160	Daily	279.8
9	Mellit	14° 13'	25° 55'	0900	Daily	223.9
10	Saraf Omra	13° 47'	23° 30'	1105	Daily	404.3
11	Umm Kadadda	13° 59'	26° 14'	0595	Daily	227.2

Source: the ministry of agriculture North Darfur State, Sudan

2.2.2.2 The satellite-based precipitation products

Six satellite precipitation products (SPPs) were compared against rain gauge observations to evaluate their efficiency in capturing rainfall variability across North Darfur State for 20 years, i.e., from 2000 to 2019. The SPPs used were the Tropical Rainfall Measuring Mission-based (TRMM) Multi-Satellite Precipitation Analysis (TMPA-3B42 7.0), African Rainfall Climatology Version 2 (ARC 2.0), Climate Hazards Group Infrared Precipitation with Stations Data (CHIRPS 2.0), Global Precipitation Measurements (GPM)—the Integrated Multi-satellitE Retrievals Final Runv6 (GPMIMERG 6.0), Precipitation Estimation from Remote Sensing Information using Artificial Neural Networks-Climate Data Record (PERSIANN-CDR), and the Tropical Applications of Meteorological using SaTEllite and ground-based observations (TAMSAT 3.1). The parameters of the six SPPs are shown in Table 2.2.

Table 2.2: Parameters of the satellite-based precipitation products (SPPs) used in the study for the period 2000–2019; TIR (thermal infrared) and PMW (passive microwave).

No.	Satellites-based precipitation products	Sensor	Temporal coverage	Spatial coverage	Temporal resolution	Spatial resolution
1	TMPA-3B42 7.0	TIR/PMW	1998–2019	Near global	Daily	0.25˚× 0.25˚
2	ARC 2.0	TIR	1983–present	Africa	Daily	0.1˚× 0.1˚
3	CHIRPS 2.0	TIR	1981–present	Near global	Daily	0.05˚× 0.05˚
4	GPMIMERG 6.0	TIR/PMW	2000–2019	Near global	Daily	0.1˚× 0.1˚
5	PERSIANN-CDR	TIR	1982–2020	Near global	Daily	0.25˚× 0.25˚
6	TAMSAT 3.1	TIR	1983–present	Africa	Daily	0.0375˚× 0.0375˚

The TRMM-based TMPA provides quasi-global precipitation products for the years 1998 to 2019 with a spatial resolution of 0.25° × 0.25° and a temporal resolution of daily and three hours, covering the latitudes 50°N–50°S (Huffman *et al.*, 2007; Wedajo *et al.*, 2021; Yong *et al.*, 2014). The TMPA is combined into gauge-adjusted daily (3B42) and monthly (3B43) post-real-time precipitation. Only the daily rainfall dataset was downloaded, and TMPA version 7 used (TMPA-3B42 7.0). The TMPA product was accessed at https://disc.gsfc.nasa.gov/. The ARC 2.0 data have been available as daily gridded precipitation data centered over the African continent at a spatial resolution of 10 km (0.1°) since 1983. The ARC 2.0 was developed by the Climate Prediction Center of the NOAA. ARC 2.0 data were retrieved from the European Organization for the Exploitation of Meteorological Satellites (EUMETSAT), which provides 3-hourly geostationary thermal infrared (TIR) data, and the Global Telecommunication System

(GTS) gauge measurements reporting 24-hour rainfall accumulations across Africa. Both the EUMETSAT and GTS have high quality data (Novella *et al.*, 2013; Usman *et al.*, 2018). The daily ARC 2.0 rainfall estimates for the period were retrieved from https://www.icpac.net/data-center/arc2/. The CHIRPS Version 2.0 rainfall dataset was developed by the United States Geological Survey and the Climate Hazard Group at the University of California. These data are available from 1981 onwards and span 50°N–50°S (all longitudes included). To create gridded rainfall time series, CHIRPS incorporates the Climate Hazard group Precipitation climatology (CHPclim) that incorporates i) satellite information to represent sparsely gauged locations, ii) 0.05° resolution cold cloud duration (CCD) -based Climate Hazard group Infrared Precipitation (CHIRP) estimates, and iii) rain gauge data (Funk *et al.*, 2015). For this study, daily CHIRPS2.0 datasets from 2000 to 2019 were used as obtained from https://earlywarning.usgs.gov/. The GPMIMERG 6.0 has a spatial resolution of (0.1° x 0.1°) and a temporal resolution of half an hour. The Global Precipitation Climatology Center's (GPCC) monthly gauge analysis is used to calibrate the Integrated Multi-satellitE Retrievals for GPM (IMERG), which is produced using combined passive microwave (PMW) and infrared (IR) data from the GPM constellation (Huffman *et al.*, 2015; Sungmin *et al.*, 2017). The most recent version of GPM (IMERG) is Final Run v 6B (IMERG6), which covers Early Run (near real-time with a latency of 6 hours), Late Run (near real-time with a latency of 18 hours), and Final Run (gauge-adjusted with a delay of four months) (Huffman *et al.*, 2015; Wedajo *et al.*, 2021). In this study, daily IMERG6 were obtained from https://gpm.nasa.gov/data/. The PERSIANN climate database was created by scientists from the University of California's Center for Remote Sensing and Hydrometeorology (Ashouri *et al.*, 2015). The PERSIANN product applies the artificial neural network (ANN) model to convert IR information into rain rates (Hsu *et al.*, 1997). For this study, daily PERSIANN data were downloaded from https://climatedataguide.ucar.edu. The TAMSAT algorithm, based on Meteosat thermal infrared (TIR) from EUMESTAT (Dembélé and Zwart, 2016), was developed at the University of Reading; the purpose is to estimate rainfall during drought in Africa and to provide famine warnings. TAMSAT's rainfall estimation is based on the assumption of a positive linear relationship between the life-time of convective clouds and rainfall amount at the surface. Therefore, TAMSAT works best for convective precipitation (Grimes *et al.*, 1999; Maidment *et al.*, 2014; Tarnavsky *et al.*, 2014). Since 1982, TAMSAT products have been provided with a spatial resolution of 0.0375° and temporal resolutions of decadal, seasonal and monthly intervals (Ayehu *et al.*, 2018). In this study, daily TAMSAT data for the period 2000–2019 were obtained from https://www.tamsat.org.uk.

2.2.3 Methods

2.2.3.1 Evaluation of satellite products

The study focused on evaluating the performance of six SPPs—the TMPA 3B42/3B43-7.0, CHIRPS 2.0, PERSIANN-CDR, GPMIMERG 6.0, ARC 2.0, and TAMSAT 3.1, to identify the best products for capturing rainy days and estimating rainfall amounts and variability trends across the study area. This was done by comparing satellite products against rain gauge measurements for the 2000–2019 period at daily, monthly and annual timescales. The point values from pixels of respective SPPs were georeferenced to gauge location and extracted from the downloaded raster files (Diem *et al.*, 2014). The study employed a point-to-pixel pairwise comparison approach, in which rainfall estimations from each satellite are created and compared with the data from each rain gauge (Ayehu *et al.*, 2018; Wedajo *et al.*, 2021).

2.2.3.2 Validation statistics

The ability of SPPs to detect rainy days, defined here as days with rainfall totaling more than 0.2 mm, was assessed based on a contingency table (Table 2.**Table *2.3***), using categorical statistical indices (Equations 2.1–2.4, Table 2.**Table *2.4***). The categorical statistics used in this study were: the probability of detection (POD, i.e., the proportion of observed rain days that were detected by the satellite product); the probability of false alarm (POFA, i.e., the proportion of satellite-estimated rain days that did not in fact occur); bias in detection (BID, i.e., assesses whether SPPs overestimates or underestimates rainy day frequency) and Heidke skill score (HSS, i.e., the measure of the overall skill of the rainfall-day estimates accounting for matches owing to chance)(Ageet *et al.*, 2022; Diem *et al.*, 2014; Girma, 2021).

Table 2.3: Contingency table for comparing rain gauge measurements and satellite-based rainfall estimates.

	Gauge $\geq$ 0.2 mm	Gauge $<$ 0.2 mm
Satellite $\geq$ 0.2 mm	Hits (H)	False alarm (F)
Satellites $<$ 0.2 mm	Miss (M)	Correct no rain (D)

The performance of the SPPs in estimating the amount and variability of rainfall across the study area was also evaluated using continuous statistical indices (Equations 2.5–2.8). One of

these indices used in this study is the Pearson correlation coefficient (r), which is used to assess the correlation's goodness of fit, with a value of 1 being the perfect score (Dembélé and Zwart, 2016). The root mean square error (RMSE) measures the mean difference between two variables; a low RMSE value indicates the predictions are precise (Ayehu *et al.*, 2018; Dembélé and Zwart, 2016; Usman *et al.*, 2018). The per cent bias (Pbias) is used to show how well the satellite rainfall estimates correspond with the gauge rainfall data average; a positive Pbias indicates overestimates, while negative Pbias indicates underestimates. The Nash-Sutcliffe efficiency (NSE) coefficient assesses the predictive skill of models—higher values suggest a better agreement between observations and satellite estimates (Nash *et al.*, 1970). A negative NSE value shows that the observed mean is a better estimator than the model, while a value of zero shows that the model predictions are as accurate as the mean of the observed data (Diem *et al.*, 2014; Legates *et al.*, 1999). The test-retest reliability was used to assess the consistency and reproducibility of the results obtained.

Table 2.4: Statistical indices for satellite-based precipitation products (SPPs), where G = gauge rainfall amount, $\bar{G}$ = average gauge rainfall amount; S = satellite rainfall estimates, $\bar{S}$= average satellite rainfall estimate, N = number of data pairs, H = number of precipitation events detected by both satellites and a rain gauge, M = number of precipitation events detected by a rain gauge by not detected by satellites; and F = number of precipitation events detected by satellites but not detected by rain gauges; D = correct negative it mean when the rain gauge and satellite rainfall failed to detect rainfall.

Statistics indicator	Abbreviation	Formula		Values range	Perfect score
Probability of detection	POD	$\frac{H}{H+M}$	(2.1)	[0 , 1]	1
Probability of false alarm	POFA	$\frac{F}{H+F}$	(2.2)	[0 , 1]	0
Bias in detection	BID	$\frac{H+F}{H+M}$	(2.3)	[- ∞ , +∞]	1
Heidke skill score	HSS	$\frac{2(HD-FH)}{(H+M)(M+D)+(H+F)(F+D)}$	(2.4)	[- ∞ , 1)	1
Pearson correlation coefficient	r	$\frac{\Sigma(G-\bar{G})\ (S-\bar{S})}{\sqrt{\Sigma((G-\bar{G})^2}\,((S-\bar{S})^2}$	(2.5)	[-1 , 1]	1
Root mean square error	RMSE (mm)	$\sqrt{\frac{1}{N}}\sum_{i=1}^{n}(S-G)^2$	(2.6)	[0 , + ∞]	0
Per cent bias	Pbias (%)	$\frac{1}{N}\left(\frac{\sum(S-G)}{\bar{G}}\right)*100$	(2.7)	[- ∞ , +∞]	0
Nash-Sutcliffe efficiency	NSE	$1-\frac{\sum(G-S)^2}{\sum(G-\bar{G})^2}$	(2.8)	[- ∞ , 1]	1

2.2.3.3 Assessment of the rainfall trends using various satellite products

The rainfall trends were assessed for the individual stations, using the mean monthly and annual rain gauge data versus the respective SPPs using the correlation coefficient (r) (Equation 2.5) and per cent bias (Pbias) (Equation 2.7).

2.3 Results

2.3.1 Evaluation of the rainfall estimate performance of the satellite products

2.3.1.1 Daily rainfall comparisons

All the daily satellite precipitation products (SPPs) and rain gauge measurements showed medium agreement, i.e., the correlation coefficient r ranged from 0.37 to 0.52 and Nash-Sutcliffe model efficiency (NSE) coefficient showed negative values, i.e., -1.57 to -0.13 (Table 2.5). The summary of comparisons indicates that Climate Hazards Group Infrared Precipitation with Station Data (CHIRPS 2.0) had a relatively high probability of detection (POD). In contrast, African Rainfall Climatology (ARC 2.0) and Tropical Rainfall Measuring Mission (TRMM) Multi-satellite Precipitation Analysis (TMPA-3B42 7.0) products scored comparatively low values for POD (Table 2.5). The CHIRPS 2.0 scored higher probability false alarm ratio (POFA) value, 0.37. The ability of all the SPPs to detect rainy days was better than random chance, as indicated by Heidke skill score (HSS) values greater than zero. All SPPs underestimated daily rainfall rates; higher rates of underestimation of rain also recorded higher values of root mean square error (RMSE). Overall, CHIRPS 2.0 was the best-performing product, followed by Tropical Applications of Meteorology using SATellite and ground-based observations (TAMSAT 3.1). The categorical statistical indices (POD, POFA, BID, and HSS) results were not considered at monthly and annual timescales because cumulative monthly and annually precipitation cloud does not reflect specific precipitation events detected by SPPs.

Table 2.5: The point-to-pixel evaluation at a daily timescale using continuous and categorical statistical tools; probability of detection (POD), probability of false alarm (POFA), bias in detection (BID) and Heidke skill score (HSS), correlation coefficient (r), root mean square error (RMSE), per cent bias (Pbias), and Nash-Sutcliffe efficiency (NSE).

Dataset	POD	POFA	BID	HSS	r	RMSE (mm day^{-1})	Pbias (%)	NSE
TMPA-3B42 7.0	0.43	0.27	0.59	0.23	0.41	57.85	-15.45	-1.41
CHIRPS 2.0	0.53	0.37	0.91	0.23	0.44	45.51	-12.15	-0.58
ARC 2.0	0.45	0.33	0.68	0.2	0.37	59.51	-17.61	-1.57

GPMIMERG 6.0	0.46	0.29	0.65	0.23	0.4	57.53	-15.36	-1.23
PERSIANN-CDR	0.51	0.31	0.9	0.16	0.49	24.47	-6.53	-0.21
TAMSAT 3.1	0.48	0.28	0.98	0.24	0.52	31.34	-8.37	-0.13

Performance: Weakest  Strongest

2.3.1.2 Monthly rainfall comparisons

Monthly rainfall comparisons reveal reliable agreement between the six SPPs and ground-based rain gauge measurements, with the NSE coefficient ranging from 0.36 to 0.49, and a strong correlation coefficient of r ≥ 0.66 (**Table 2.6**). Based on the statistical analysis, TAMSAT 3.1 performed better in estimating the monthly rainfall in the region than the other SPPs; TAMSAT 3.1 produced the best value of NSE, 0.49 and the lowest RMSE, 47.1. All SPPs overestimated the rainfall amount, except the ARC 2.0 product; the highest per cent bias (Pbias) value was produced by the Precipitation Estimation from Remote Sensing Information using Artificial Neural Networks-Climate Data Record (PERSIANN-CDR), 48.88% (**Table *2.6***). The SPPs produced relatively strong correlation coefficients against rain gauge observations; the TAMSAT 3.1 scored the highest r value, 0.71.

Table 2.6: The point-to-pixel evaluation at a monthly timescale using continuous statistical tools; correlation coefficient (r), root mean square error (RMSE), per cent bias (Pbias), and Nash-Sutcliffe efficiency (NSE).

Dataset	r	RMSE (mm month^{-1})	Pbias (%)	NSE
TMPA-3B42 7.0	0.71	52.73	15.34	0.36
CHIRPS 2.0	0.73	50.64	1.49	0.41
ARC 2.0	0.67	51.19	-20.25	0.4
GPMIMERG 6.0	0.72	51.49	18.01	0.39
PERSIANN-CDR	0.66	76.66	48.88	-0.35
TAMSAT 3.1	0.75	47.1	10.29	0.49

Performance: Weakest  Strongest

2.3.1.3 Annual comparisons of rainfall totals

Strong agreement between the six SPPs and rain gauge measurements was demonstrated by annual comparisons, producing NSE coefficients ranging from 0.19 to 0.61 (**Table *2.7***), and reliable correlation coefficients (r) ranging from 0.58 to 0.81 (Table 2.7). The Integrated Multi-satellitE Retrievals for Global Precipitation Measurements (GPM) Final Run (GPMIMERG 6.0) produced a relatively high correlation value. Based on the statistical analysis, the results

indicated that TAMSAT 3.1 performed better than the other SPPs products; TAMSAT 3.1 produced the best value for the NSE and RMSE (**Table 2.7**). All SPPs overestimated the rainfall amount, except the ARC 2.0 product which provided an underestimate. The highest Pbias values was by PERSIANN-CDR, 82.69%.

Table 2.7: The point-to-pixel evaluation at an annual timescale using continuous statistical tools; correlation coefficient (r), root mean square error (RMSE), per cent bias (Pbias), and Nash-Sutcliffe efficiency (NSE).

Dataset	r	RMSE (mm annual^{-1})	Pbias (%)	NSE
TMPA-3B42 7.0	0.8	110.2	21.33	0.5
CHIRPS 2.0	0.78	112.4	22.85	0.39
ARC 2.0	0.76	89.8	-16.9	0.35
GPMIMERG 6.0	0.81	100.4	10.19	0.19
PERSIANN-CDR	0.58	235.2	82.69	-0.57
TAMSAT 3.1	0.71	8.7	14.98	0.61

Performance: Weakest — Strongest

2.3.2 Mean monthly rainfall trends

Spatio-temporal variation in the mean monthly precipitation for the 11 rain gauge stations using the six SPPs are shown in **Figure 2.2**. The SPPs estimated the trends in rainfall for the rainy season, i.e., from May to October, with peak rainfall occurring during August and September (**Figure 2.2**). All SPPs show that, comparatively, Kabkabiya, Saraf Omra, and Kutum, located in the Marra Mountains, receive more rainfall. As indicated by the SPPs, Kabkabiya, at an elevation of 1120 m, receives a monthly rainfall range 2.2-295.9 mm, while Saraf Omra, at an elevation of 1105 m, receives 2-380.5 mm. Kutum area at an elevation of 1160 m north of Marra mountains ranges 1.5-170.9 mm. Mellit and El Malha areas at lower elevation, recorded 1-119.7 mm and 3-129.2 mm, respectively.

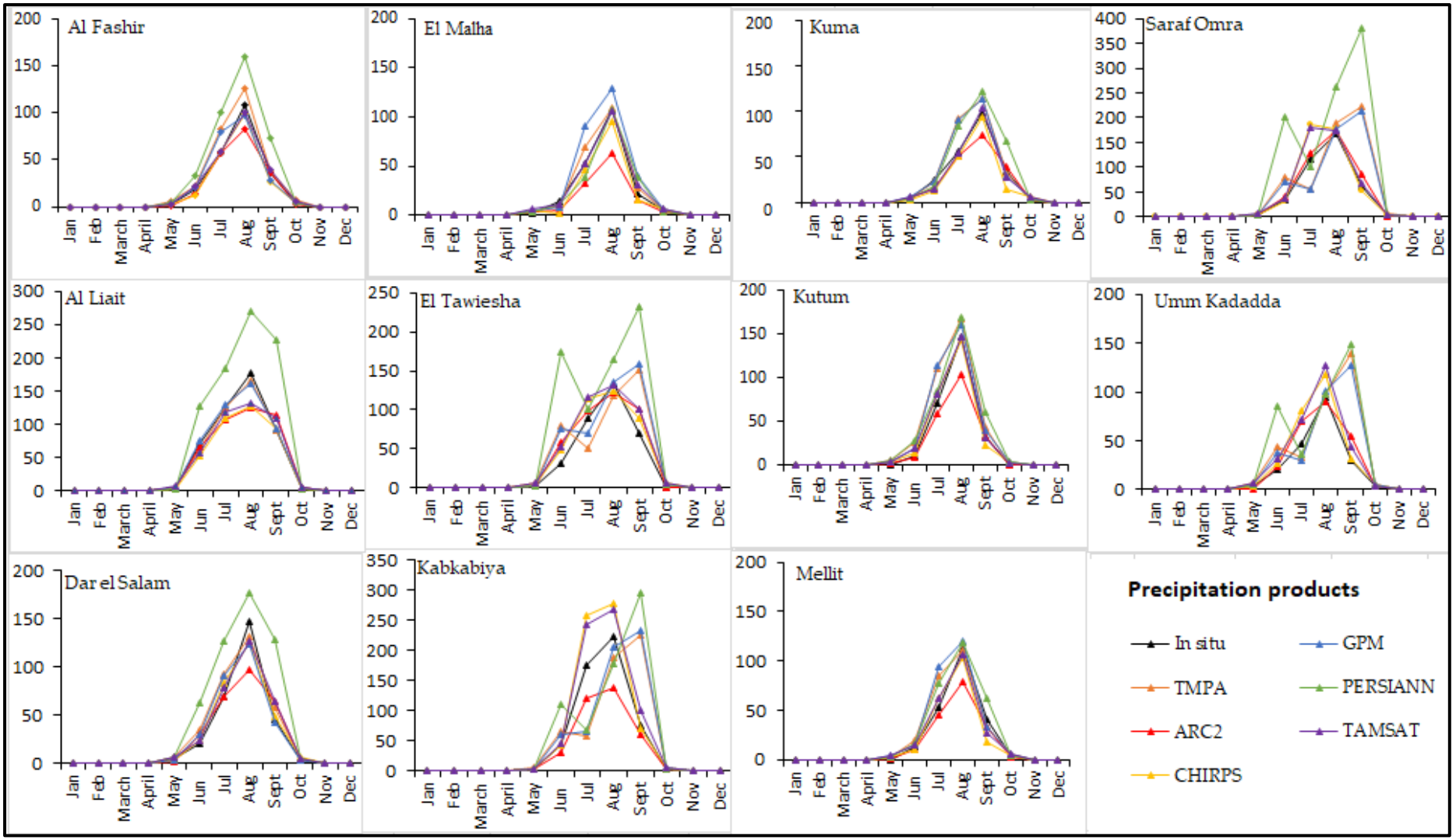


Figure 2.2. Comparison of rain gauge observations based on monthly rainfall trends for 11 stations over North Darfur State and six-satellite precipitation products over the 20-year study period (2000–2019).

TMPA-3B42 7.0 and CHIRPS 2.0 in Al Fashir (**Table 2.8**), recorded the highest correlation values. Al Liait recorded the lowest correlation values. The highest overestimated trends in rainfall were by PERSIANN-CDR), while the most underestimated trends in rainfall were by ARC 2.0.

Table 2.8: The Performance of six SPPs in estimating rainfall trends on a monthly timescale at 11 stations, using Pearson's correlation coefficient (r) and per cent bias (Pbias %).

Stations	Statistic	TMPA-3B427.0	CHIRPS 2.0	ARC 2.0	GPMIMERG 6.0	PERSIANN-CDR	TAMSAT 3.1
Al Fashir	r	0.83	0.84	0.61	0.80	0.80	0.72
	Pbias	24.91	-10.23	-19.72	5.56	67.57	3.62
Al Liait	r	0.48	0.41	0.25	0.42	0.20	0.48
	Pbias	-17.78	-13.79	0.05	70.88	-9.39	-3.36
Dar El Salam	r	0.61	0.62	0.56	0.59	0.45	0.72
	Pbias	15.19	1.99	-6.96	4.68	72.00	8.17
El Malha	r	0.68	0.65	0.71	0.71	0.64	0.64
	Pbias	4.19	-20.84	-43.36	28.49	-4.58	7.50
El Tawiesha	r	0.47	0.65	0.43	0.53	0.53	0.66
	Pbias	17.68	11.16	9.91	29.21	85.50	17.41
Kabkabiya	r	0.54	0.71	0.74	0.54	0.55	0.53
	Pbias	0.55	23.57	-34.98	5.67	16.10	28.46
Kuma	r	0.56	0.61	0.44	0.57	0.55	0.61
	Pbias	-15.65	-14.13	27.71	37.49	-2.47	29.27
Kutum	r	0.77	0.79	0.79	0.70	0.67	0.67
	Pbias	29.53	-1.92	-24.32	24.89	21.77	5.25
Mellit	r	0.66	0.70	0.69	0.64	0.61	0.61
	Pbias	14.59	-10.77	-24.68	21.38	25.45	-1.94
Saraf Omra	r	0.50	0.70	0.68	0.39	0.46	0.72
	Pbias	20.90	14.25	42.32	143.12	27.26	49.51
Umm Kadadda	r	0.61	0.41	0.44	0.55	0.57	0.60
	Pbias	59.96	26.08	16.65	50.98	76.68	40.04

2.3.3 Mean annual rainfall trends

Spatio-temporal variation in the mean annual precipitation for the 11 rain gauge stations using the six SPPs are shown in **Figure 2.3**. El Malha receives between 26 and 542.1 mm, while Mellit receives 92-545 mm. *The wetter* Kabkabiya, Saraf Omra and Kutum areas recorded rainfall in the range 206-1113 mm, 188-1205 mm, and 103-551 mm, respectively.

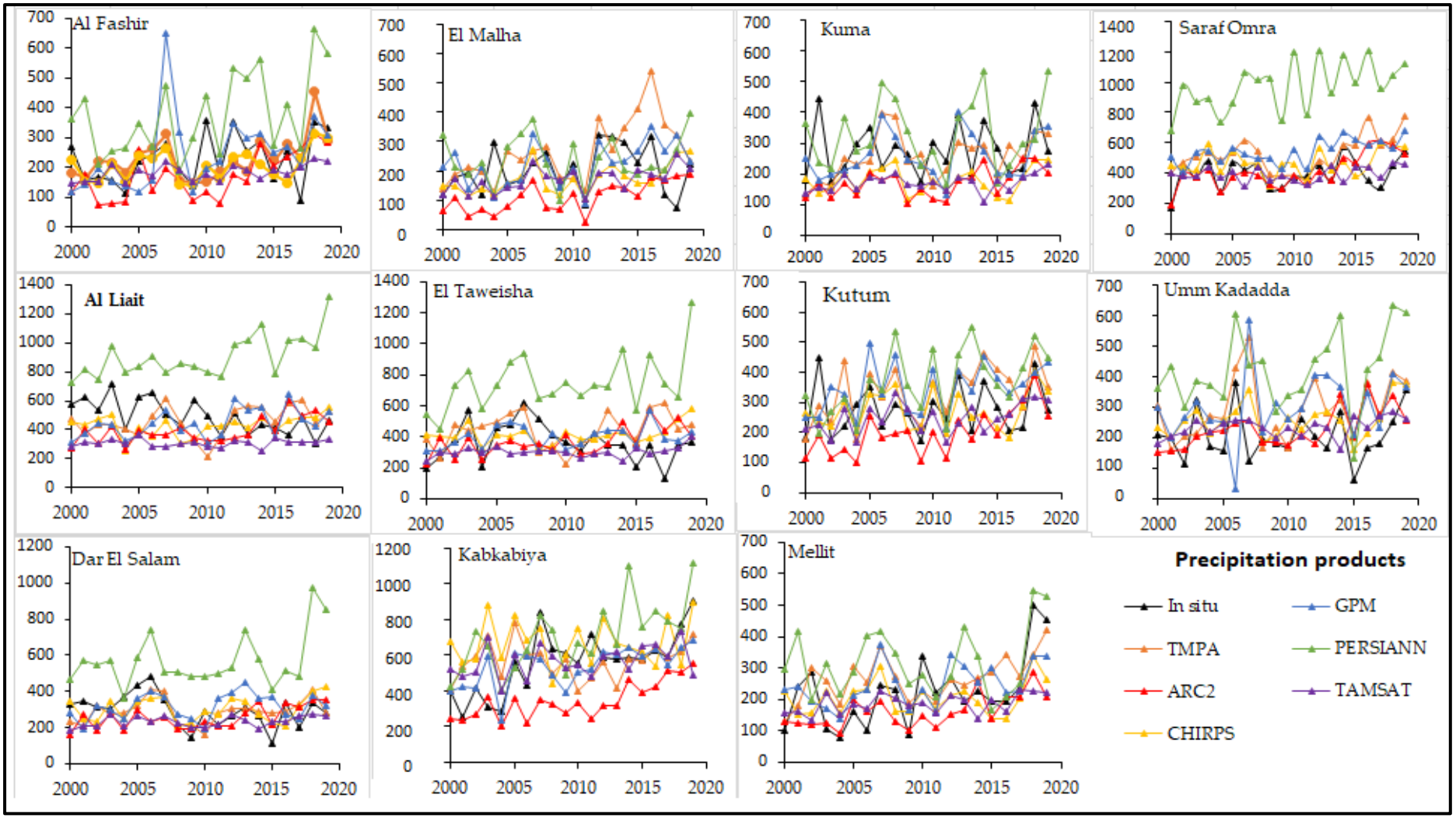


Figure 2.3. Comparison of rain gauge observations based on annual rainfall trends in 11 stations over North Darfur State and six SPPs over the 20-year study period (2000–2019).

The highest correlation values were in El Malha by GPMIMERG 6.0 and ARC 2.0 (Table 2.9). Others were TAMSAT 3.1 in Kutum and PERSIANN-CDR in Kuma, Kutum and Kabkabiya. The PERSIANN-CDR reported the most overestimated trends in rainfall, while the most underestimated trends in rainfall were by CHIRPS 2.0. Generally, the best performing SPPs were TMPA-3B42 7.0 (Al Fashir, Dar ES Salam) and TAMSAT 3.1 (Kabkabiya, Saraf Omra).

Table 2.9: The rainfall trends for the 20-year study period (2000–2019) were assessed at the annual timescale for six SPPS at 11 stations using the Pearson's correlation coefficient (r) and per cent bias (Pbias %).

Stations	Statistic/ products	TMPA-3B42 7.0	CHIRPS 2.0	ARC 2.0	GPMIMERG 6.0	PERSIANN-CDR	TAMSAT 3.1
Al Fashir	r	0.47	0.57	0.66	0.36	0.67	0.46
	Pbias	0.79	-24.26	-9.45	-16.26	65.96	-20.22
Al Liait	r	0.22	0.38	0.46	0.55	0.66	0.34
	Pbias	-6.37	-13.09	-20.22	-10.03	83.53	-37.56
Dar El Salam	r	0.43	0.51	0.39	0.17	0.47	0.46
	Pbias	-1.64	2.45	-13.79	7.22	92.38	-21.26
El Malha	r	0.42	0.34	0.82	0.83	0.37	0.52
	Pbias	29.50	-15.47	-44.78	6.97	12.97	-15.97
El Tawiesha	r	0.41	0.22	0.43	0.42	0.64	0.36
	Pbias	21.54	14.30	1.72	10.25	106.48	-16.81
Kabkabiya	r	0.23	0.46	0.56	0.70	0.72	0.25
	Pbias	23.25	-38.37	-3.59	25.58	1.12	1.30
Kuma	r	0.14	0.57	0.54	0.44	0.76	0.25
	Pbias	-7.25	-35.51	-38.05	-6.63	18.67	-37.98
Kutum	r	0.50	0.57	0.56	0.61	0.72	0.74
	Pbias	20.87	-0.96	-27.45	25.11	32.83	9.99
Mellit	r	0.61	0.44	0.58	0.57	0.61	0.43
	Pbias	19.08	-8.07	-26.94	11.15	42.91	-16.70
Saraf Omra	r	0.51	0.40	0.51	0.62	0.63	0.28
	Pbias	31.81	19.48	3.03	37.85	161.07	-0.90
Umm Kadadda	r	0.25	0.63	0.38	0.44	0.46	0.21
	Pbias	44.79	24.72	10.07	53.00	103.54	12.45

2.4 Discussion

Rainfall in Africa is challenging to estimate accurately because it is majorly a result of convective rainstorms, which are very localized spatially and temporally. The seasonal movement of the Inter-Tropical Convergence Zone (ITCZ) mainly regulates rainfall in Sudan. Therefore, the rainfall is convective in nature, derived from showers and thunderstorms. The rainfall depicts an extreme spatial variation which the existing rain gauge network cannot monitor effectively. In fact, it is argued that no conceivable rain gauge network would be adequate for the country. The reliability and applicability of the current satellite precipitation products (SPPs) against rain gauge observations across North Darfur State of Sudan was evaluated for a 20-year study period, i.e., 2000–2019. The SPPs were the Tropical Rainfall Measuring Mission (TRMM) Multi-satellite Precipitation Analysis (TMPA-3B42 7.0), African Rainfall Climatology Version 2 (ARC 2.0), Climate Hazards Group Infrared Precipitation with Station Data (CHIRPS 2.0), Integrated Multi-satellitE Retrievals for Global

Precipitation Measurements (GPM) Final Run v 6 (GPMIMERG 6.0), Precipitation Estimation from Remote Sensing Information using Artificial Neural Networks-Climate Data Record (PERSIANN-CDR), and the Tropical Applications of Meteorology using SATellite and ground-based observations (TAMSAT 3.1). The satellite-based rainfall estimation was assessed at daily, monthly, and annual timescales using point-to-pixel-based pairwise statistics.

2.4.1 Validation of satellite precipitation products at daily timescale

Although CHIRPS 2.0 recorded the highest probability of detection (POD), the probability of false alarm (POFA) was also the highest (**Table 2.5**). To the contrary, the TMPA-3B42 7.0 performed poorly—it only detected 43% of the observed rainfall events in the study area, although it reported the lowest POFA and bias in detection (BID). The PERSIANN-CDR reported the lowest root mean square error (RMSE) and per cent bias (Pbias). Daily satellite rainfall had a low correlation (r) with the rain gauge data—the TAMSAT 3.1 recorded the highest correlation value, 0.53. The weak agreement between the SPPs and rain gauge observations is in line with Usman *et al.* (Usman *et al.*, 2018) and Dembélé and Zwart (Dembélé and Zwart, 2016) in the Sudano Sahelian zone of Nigeria and Burkina Faso, respectively—and that CHIRPS 2.0 was the product most capable of detecting rainy days. The subpar performance of the rainfall products can be primarily attributed to errors in satellite models when predicting the accumulation and distribution of rainfall (Dembélé and Zwart, 2016; Zambrano-Bigiarini *et al.*, 2017b). Another reason could be the presence of a high variance and lack of dynamic range in daily rainfall estimates (Mekonnen *et al.*, 2023). The POD metric indicates that SPPs fail to identify precipitation events with short durations. Rainfall events in the study area are spatially and temporally discontinuous, and the duration of rainfall may not last for long, therefore, satellite sensors may not capture the rainfall events (Haile *et al.*, 2013). Another source of error is the presence of the Marrah highlands—the magnitude of rainfall is underestimated because satellite estimates normally miss precipitation that is enhanced by flow lifting over mountains (Castro *et al.*, 2015).

2.4.2 Validation of satellite precipitation products at monthly timescales

Overall, all SPPs relatively correlated well with rain gauge observations—as the time scale increases, the performance of SPPs improves significantly (Ayehu *et al.*, 2018; Dinku *et al.*, 2007; Wedajo *et al.*, 2021; Wu *et al.*, 2019). The TAMSAT 3.1 showed the best correlation with rain gauge observations (**Table 2.6**). The best performance in RMSE was the TAMSAT, while the CHIRPS 2.0 recorded the lowest overestimation of monthly rainfall. The PERSIANN-CDR was the worst because it reported the lowest correlation coefficient, the highest RMSE, and the highest Pbias. Also, Gadouali *et al.* (Gadouali *et al.*, 2020) in Morocco and Dembélé and Zwart (Dembélé and Zwart, 2016) of Burkina Faso reported PERSIANN-CDR as the worst at detecting monthly rainfall events. The poor performance can be attributed to cloud-top infrared (IR) observations (Beck *et al.*, 2017). The only underestimation of rainfall was from ARC 2.0, which is in agreement with Ayehu *et al.* (Ayehu *et al.*, 2018). The other five SPPs overestimated rainfall—Wedajo *et al.* (Wedajo *et al.*, 2021) and Girma, (Girma, 2021) reported overestimations of rainfall data from the TMPA-3B42 7.0, CHIRPS 2.0 and GPMIMERG 6.0, and TAMSAT 3.1, respectively. Gebremicael *et al.* (Gebremichael *et al.*, 2005) found that the CHIRPS 2.0 and TMPA-3B42 7.0 products underestimated rainfall in northern Ethiopia—the inconsistency with the current study may be due to differences in topography and/or climate conditions. Satellite precipitation products (SPPs) are known for overestimation of rainfall in arid and semiarid areas and underestimation in humid areas (Ibrahim *et al.*, 2022). The overestimations are due to the fact that raindrops might evaporate before striking the surface (McCollum *et al.*, 2000), and the underestimation over higher altitude is due to strong scattering of the microwave (MW) signal by mountains (Huffman *et al.*, 2007) and misses the discrimination of warm clouds by IR sensors commonly found on the tops of mountainous regions (Cavalcante *et al.*, 2020). Also, during the rainy season, satellite sensors have limited capability in identifying rainfall events because of non-raining clouds that could produce brief localized showers (Su *et al.*, 2017). As well, intense rainfall can cause radar signals to attenuate, leading to inaccurate measurements (Cheema *et al.*, 2012).

Generally, the TAMSAT 3.1 and CHIRPS 2.0 performed better, and the PERSIANN-CDR performed poorly in all indices—this is consistent with Ageet *et al.* (Ageet *et al.*, 2022), Grimes et al. (Grimes *et al.*, 1999), Fenta *et al.* (Fenta *et al.*, 2018), Basheer *et al.* (Basheer *et al.*, 2019) , and Dinku *et al.* (Dinku *et al.*, 2007). The TAMSAT's primary benefit is that it

employs local calibration datasets, where the temperature threshold and regression parameters are geographically and temporally variable (Dinku *et al.*, 2007). The strong performance of CHIRPS 2.0 in this study is in line with its high temporal and spatial resolution, capacity to integrate satellite data and ability to gauge and reanalyse outputs (Funk *et al.*, 2015). The use of CHPClim, a gauge-satellite climatological tool, also offsets bias.

2.4.3 Validation of satellite precipitation products at annual timescales

The GPMIMERG 6.0 and TMPA-3B42 7.0 were the highest correlated SPPs with rain gauge measurements (Table **2.7**). The PERSIANN-CDR performed dismally, i.e., it recorded the lowest correlation coefficient, the worst RMSE, the highest overestimation of rainfall, and a negative Nash-Sutcliffe Efficiency (NSE). The TAMSAT 3.1 reported the least RMSE. Only ARC 2.0 underestimated annual rainfall, while the rest of the SPPs overestimated rainfall in the range. The TAMSAT 3.1 recorded the highest NSE value—higher values suggest a better agreement between rain gauge measurements and satellite estimates (Nash and Sutcliffe, 1970). Overall, TAMSAT 3.1 performed better and the PERSIANN-CDR performed poorly in all indices. These results are in line with prior research on the Sudanese Blue Nile basin and the East African Sio-Malaba-Malakisi River basin (Abd Elhamid *et al.*, 2020; Omonge *et al.*, 2022). However, a study carried out in Ethiopia's Upper Blue Nile basin contradicted the superiority of TAMSAT 3.1 at annual timescales (Bayissa *et al.*, 2017). The underperformance of the PERSIANN-CDR in capturing rainfall variability amounts is also consistent with studies conducted in East Africa and northern Egypt (Kimani *et al.*, 2017; Roushdi, 2022). The PERSIANN-CDR is calibrated based on Global Precipitation Climatology Project (GPCP) (Liu *et al.*, 2017); however, this does not guarantee improved performance in the study area. The performance of GPMIMERG 6.0 in rainfall estimations is superior to that of ARC 2.0 and PERSIANN-CDR, as confirmed by Zhang et al. (Zhang *et al.*, 2019). Owing to the dual and high-frequency channels, which improve the detection of light and solid precipitation, GPMIMERG 6.0 has a superior performance (Huffman *et al.*, 2015). This can be explained by the greater efficiency of MW sensors—satellite products that use MW sensors to measure rainfall perform better than those that use IR sensors (Bitew *et al.*, 2011). Generally, the IR sensor compared to passive/active MW can lead to high POFA, and low POD, especially in sub-tropics and semi-arid and arid regions (Kidd *et al.*, 2022).

2.4.4 Station-wise mean monthly and annual rainfall trends

In this study, the rate of rainfall is linearly related to altitude—comparatively, the area located in the south, around the Marrah Mountains, roughly receives more rainfall compared to the north, the lowland. Station-wise monthly rainfall trends showed that not all SPPs followed similar pattern as the rain gauge data—notable was the PERSIANN-CDR and ARC2. The PERSIANN-CDR curve was conspicuously above the rain gauge and other SPPs curves in Al Fashir, Al Liait, and Dar el Salam. Severally, the PERSIANN-CDR curve exhibited a bimodal distribution, e.g., El Tawiesha, Kabkabiya, Saraf Omra, and Umm Kadadda, while the rain gauge curve showed only a single peak. Only in El Malha and Kutum stations, the PERSIANN-CDR closely followed the rain gauge curve. The ARC 2.0 curve was mostly below the rain gauge and other SPPs curves—only in Saraf Omra that the ARC 2.0 curve was almost the same as the rain gauge curve. The TAMSAT 3.1 and CHIRPS 2.0 closely followed the rain gauge curve pattern. The PERSIANN-CDR remains the worst at station-wise level with relatively low correlation coefficient compared to other SPPs. The TAMSAT 3.1 and CHIRPS 2.0 were better performers, with higher correlation coefficients. Compared to station-wise mean monthly rainfall trend, station-wise mean annual rainfall trends are different. The PERSIANN-CDR has relatively higher correlation coefficients compared to TAMSAT 3.1 and CHIRPS 2.0 in almost all rain gauge stations, although the PERSIANN-CDR relatively overestimated the mean annual rainfall, compared to the other SPPs. Overall, the TAMSAT 3.1 and CHIRPS 2.0 were the best performers. Generally, all SPPs revealed increasing trends.

2.4.5 The Study limitations

This study used six SPPs and 11 rain gauge stations which are not spatially distributed in the climatic zones of North Darfur State. The variations in the quantity, quality, and distribution of rain gauge stations in the study area might have introduced errors that led to uncertainties in the performance of SPPs in capturing the spatio-temporal rainfall variability (Mekonnen *et al.*, 2023). Also, the uncertainties attributed to errors in the retrieval algorithm, rain gauge measurement, and bias correction processes may render SPPs measurement of rainfall unreliable, because it may distort interpretation of the rainfall's behaviour and simulation results by penetrating into other models such as the crop, hydrological and meteorological models. The reliability of a particular rainfall dataset could vary with the temporal period of evaluation (Mekonnen *et al.*, 2023). Another uncertainty may be associated with the point-to-

pixel approach used that compared two datasets at different spatial scales (Mekonnen *et al.*, 2023). Therefore, these errors cannot be ignored when using SPPs in various applications (Taye *et al.*, 2023). The errors could be the reason why several SPPs underestimated and/or overestimated rainfall in the study area. Therefore, comprehensive uncertainty characterization of satellite-derived rainfall products is vital. But the main limitation is the spatial and temporal resolutions of the data—investigating spatio-temporal variability of rainfall requires the use of precipitation datasets that have high spatial and temporal resolutions (Pierre *et al.*, 2011).

2.5 Conclusions

For climate studies and meteorological applications in data-poor regions of Africa, such as the Darfur region, satellite precipitation products (SPPs) represent an alternative source of rainfall data. The daily time intervals showed that there was a weaker agreement between SPPs and rain gauge measurements—the Climate Hazards Group Infrared Precipitation with Station Data (CHIRPS 2.0) was identified to be better in detecting rainy days. The results of the monthly and annual time scales showed that there was a stronger agreement between rain gauge observations and SPPs. Overall, the Tropical Applications of Meteorology using SATellite and ground-based observations (TAMSAT 3.1) and CHIRPS 2.0 were comparatively better—therefore, TAMSAT 3.1 and CHIRPS 2.0 could be reliable sources of rainfall data for stakeholders and researchers, in North Darfur. All SPPs exhibited errors in the continuous and categorical indices used—the SPPs indicated underestimations and overestimations in the analyses. Since the accuracy and reliability of satellite datasets is vital, future research should focus on more sophisticated algorithms and technological advancement that can provide near-real time data effective in improving the accuracy and reduce the uncertainties of estimated precipitation in data-scarce regions worldwide. Advanced SPPs data fusion techniques for infrared (IR) and microwave (MW) datasets should be explored.

CHAPTER THREE

Mapping cropland types in a highly heterogeneous semi-arid environment using Sentinel-2 dataset and machine learning algorithms on Google Earth Engine cloud

This Chapter based on:

Altoom, M.B., Adam, E., & Ali, K.A. (in preparation). Mapping cropland types in a highly heterogeneous semi-arid environment using Sentinel-2 dataset and machine learning algorithms on Google Earth Engine cloud

Abstract

Monitoring crops ensures national, regional, and global food security. Monitoring crops entails gathering information such as the health and growth of crops and environmental conditions. Therefore, monitoring crops aids farmers in making well-informed decisions, enhancing productivity, and reducing environmental impact. This, in turn, leads to improved economic outcomes and long-term agricultural sustainability. Monitoring crops in arid and semi-arid lands is critical because water availability is a major factor limiting crop growth. This study used Sentinel-2 (S2) image collection in Google Earth Engine (GEE) to classify crop types in North Darfur State, Sudan using support vector machine (SVM) and random forest (RF) models classifiers. Eight vegetation indices (VIs), i.e.,normalised difference vegetation index (NDVI), enhanced vegetation index (EVI), soil-adjusted vegetation index (SAVI), green-normalised difference vegetation index (GNDVI, weighted Difference vegetation index (WDVI), red edge NDVI (NDVIre), ratio-vegetation index (RVI), and normalised difference infrared index (NDII) were used as additional bands. The results show that the RF models produced overall accuracies (OA) in the range of 90–97%, and 0.87–0.96 for kappa coefficient (κ). The SVM models reported OA and κ values in the range of 84–95% and 0.81–0.94, respectively. Producer's (PA) and user's accuracies (UA) were in the range 83–97% and 81–98%, respectively. Highest F1 scores for both classifiers were 0.98. The findings of this study, along with the derived classification maps, would enable farmers, policymakers, and other stakeholders to make well-informed decisions regarding agricultural production, land use planning, and resource management in North Darfur and arid environments.

Key words: Sentinel-2 image collection, crop type mapping, food security, North Darfur State, semi-arid lands, Google Earth Engine, machine learning algorithms.

3.1 Introduction

Accurate mapping and monitoring of agricultural land at the crop type level is crucial in precision agriculture, especially in regions facing rapid climate variability (Brinkhoff *et al.*, 2019; Chabalala *et al.*, 2022). Lack of adequate data due to insufficient resources and difficulties with access to some areas, probably because of security concerns and other obstacles, means that traditional approaches to collecting agricultural data are challenging (Eklund *et al.*, 2017; Qader *et al.*, 2021). Furthermore, Crop yield assessment based on conventional data collection techniques such as crop cut data, expert scouting estimates, and field surveys lacks reliability because they are resource-intensive, time consuming, and susceptible to errors (Ge *et al.*, 2016; Sinha *et al.*, 2022). Therefore, embracing such an approach may introduce uncertainties as yields can display significant spatial variations within farmland (Lobell *et al.*, 2019; Paliwal *et al.*, 2020). As the demand for addressing food insecurity and enhancing livelihoods grows, the significance of dependable farm-level yield estimates derived from crop type maps is increasingly paramount (Karst *et al.*, 2020; Sapkota *et al.*, 2016).

In order to address the ongoing and escalating demands for future food needs, employing accurate, timely, reliable, cost-effective, and inclusive agricultural intelligence technology is essential (Löw *et al.*, 2013; Ouzemou *et al.*, 2018). Such technology will facilitate improved management of the agricultural landscape and accurate mapping of crops (Defourny *et al.*, 2019; Mazarire *et al.*, 2020). Satellite remote sensing (RS) has become a crucial and efficient technology, allowing for spatiotemporal monitoring of crops. Remote sensing (RS) helps identify crop types, evaluate actual distribution and extent of damage, assess nutrient status, and predict yields (Asgarian *et al.*, 2016). Remote sensing (RS) saves time and conserve resources in agricultural management (Asgarian *et al.*, 2016; Cui *et al.*, 2022; Felegari *et al.*, 2021; Kosari *et al.*, 2020). Remote sensing (RS) offers the advantage of monitoring vast spatial expanses (Böhler *et al.*, 2020; Chabalala *et al.*, 2023; Gourlay *et al.*, 2017). Nevertheless, monitoring crops in heterogeneous arid environments faces frequent hindrances due to challenges such as limited input datasets, high soil background reflectance, the coexistence of green and senescent grasses, and the prevalence of shrubs in grasslands, which share similar reflective characteristics to cropland (Ozdogan, 2010; Qader *et al.*, 2023; Tran *et al.*, 2022). Recent improvements in spatial, spectral, and temporal resolutions, exemplified by sensor

datasets like those from the Sentinel-2 Multispectral Imager (MSI), provide new opportunities for monitoring smallholder farms. The global coverage and free access to such datasets further contribute to their utility. The Sentinel-2 MSI sensor comprises shorter revisit periods to accommodate the temporal dynamics of crop growth (Malenovský *et al.*, 2012). The high spatial resolution across a broad range of spectral channels facilitates the discrimination of intricate vegetation spectral signatures (Defourny *et al.*, 2019). Furthermore, it boasts high radiometric and spectral resolution, enabling the identification of detailed vegetation properties.

Vegetation indices (VIs) serve as valuable tools in precision agriculture, such as mapping crop types for policy makers to make well-informed decisions (Thenkabail *et al.*, 2000). Due to the numerous light, environmental, and biological variables in agriculture, researchers have devised various vegetation indices (Rouse *et al.*, 1974; Xue *et al.*, 2017). Selecting the appropriate VI is crucial for achieving accurate results, and this choice depends on factors such as sensor type, environmental conditions, crop type, and growth stage (Hatfield *et al.*, 2019; Kang *et al.*, 2019). Therefore, in crop mapping, gaining insight into the inherent strengths and limitations of commonly used indices aids in selecting the most suitable one (Delavarpour *et al.*, 2021). The RGB sensors exclusively generate VIs based on visible light, capturing what is perceptible to the human eye with subtle variations (Xue and Su, 2017). On the other hand, multispectral sensors, such as Sentinel-2 (S2), provide VI choices derived from invisible infrared wavelengths, thereby uncovering details that are not discernible to the human eye (Kganyago *et al.*, 2021).

The development of machine learning (ML) algorithms presents an intriguing opportunity to understand how classifiers operate within heterogeneous agricultural landscapes (Mazarire *et al.*, 2020). Therefore, the choice of classification method is equally crucial for successful crop type mapping besides selecting the appropriate RS data (Sothe *et al.*, 2017). Different ML algorithms have been used for mapping crop types using satellite imagery, e.g., (Camargo *et al.*, 2019; Friedman, 2002; Jony *et al.*, 2018; Loukika *et al.*, 2021; Mahalanobis *et al.*, 1996; Nitze *et al.*, 2012; Qian *et al.*, 2014; Rodriguez-Galiano *et al.*, 2012).
Non-parametric classifiers are deemed appropriate and superior due to their capacity to disregard the dataset's assumption of a normal distribution, and they do not necessitate statistical parameters when distinguishing between image classes (Adam *et al.*, 2014; Inglada *et al.*, 2015; Ouzemou *et al.*, 2018; Sothe *et al.*, 2017). Hence, contemporary algorithms are

preferred as they overcome the limitations of traditional ones by being able to synthesize classification functions using both discrete and continuous datasets (Sothe *et al.*, 2017). Machine learning (ML) algorithms are also robust to noise, ensuring that they are not constrained by assumptions related to parametric distributions (Löw *et al.*, 2013). Moreover, a gap exists in identifying which machine learning algorithms are most suitable for the distinctive classification of crop types (Mazarire *et al.*, 2020).

While the acquisition and availability of satellite imagery data have seen significant improvements, traditional hardware and software methods remain time-consuming, mainly when undertaking image processing on a larger scale (Gorelick *et al.*, 2017; Kumar *et al.*, 2018; Mashala *et al.*, 2023). Therefore, massive challenges exist in RS images download and processing efficiency on large scale. Using high-resolution images for identifying crop types across extensive regions is expensive, demanding substantial computation power for image processing and significant storage capacities (Chong *et al.*, 2021; Loukika *et al.*, 2021; Shaharum *et al.*, 2020; Sujud *et al.*, 2021). To address these challenges effectively, Google developed the Google Earth Engine (GEE), a free cloud computing and storage platform, which enables high-speed analysis using advanced techniques for processing data (Amani *et al.*, 2020; Sonobe *et al.*, 2014). Thus, GEE enhances researchers' and practitioners' accessibility to computationally demanding analyses, particularly those with limited access to advanced computational resources. Google Earth Engine (GEE) incorporates freely accessible satellite imagery from Sentinel, MODIS, and Landsat, among other sources. In GEE, client libraries are created in JavaScript to handle the code editing and built-in ML algorithms (Pimple *et al.*, 2018; Shelestov *et al.*, 2017).

Like most developing countries in the Sahel region, Sudan faces multiple challenges, such as high poverty, a decline in agricultural productivity and other socioeconomic challenges and environmental degradation (Mirzabaev *et al.*, 2021). Nevertheless, agriculture constitutes approximately one-third of the GDP and is the predominant source of employment, with over 75% of the labour force engaged in agricultural and related activities (Osman, 2017). Sorghum, millet, groundnuts, wheat, and sugar cane are grown in Sudan (Abbas *et al.*, 2013; Altoom *et al.*, 2023; Ibrahim, 1978).

In North Darfur, employing RS technology in agriculture poses specific challenges, e.g., the communal landscape is primarily marked by fragmented, small parcel-sized fields with

varying crop types within a pixel, contributing to highly heterogeneous crop cover. This limitation arises from various crop types exhibiting significant variability in phonological stages within fields, encompassing early sprouting, establishment, and maturation. Consequently, these variations may result in identical spectral signatures at specific points in their development (Asgarian *et al.*, 2016). This study utilised high-resolution Sentinel-2 optical satellite dataset in GEE, to map crops in North Darfur using random forest (RF) and support vector machine (SVM) classification algorithms. Also, eight VIs, i.e., normalised difference vegetation index (NDVI), enhanced vegetation index (EVI), soil-adjusted vegetation index (SAVI), green-normalised difference vegetation index (GNDVI), weighted difference vegetation index (WDVI), red-edge NDVI (NDVIre), ratio-vegetation index (RVI), and normalised difference infrared index (NDII) were extracted from the S2 image collection.

3.2 Materials and Methods

3.2.1 Study area

The North Darfur is a vast region located in western Sudan at latitude 11° 45′ 49″–20° 00′ 30″ N and longitude 22° 46′ 47″–27° 29′ 47″ E, occupying more than half of the Darfur region (Figure 3.1). The highest point is Marrah Mountain (3,000 m above sea level) (Altoom *et al.*, 2023; Ibrahim, 1984). Locally, the state shares borders with Northern, North, and South Kordofan and internationally with Libya and Chad. North Darfur State comprises eleven districts, and Al Fashir is the capital city.

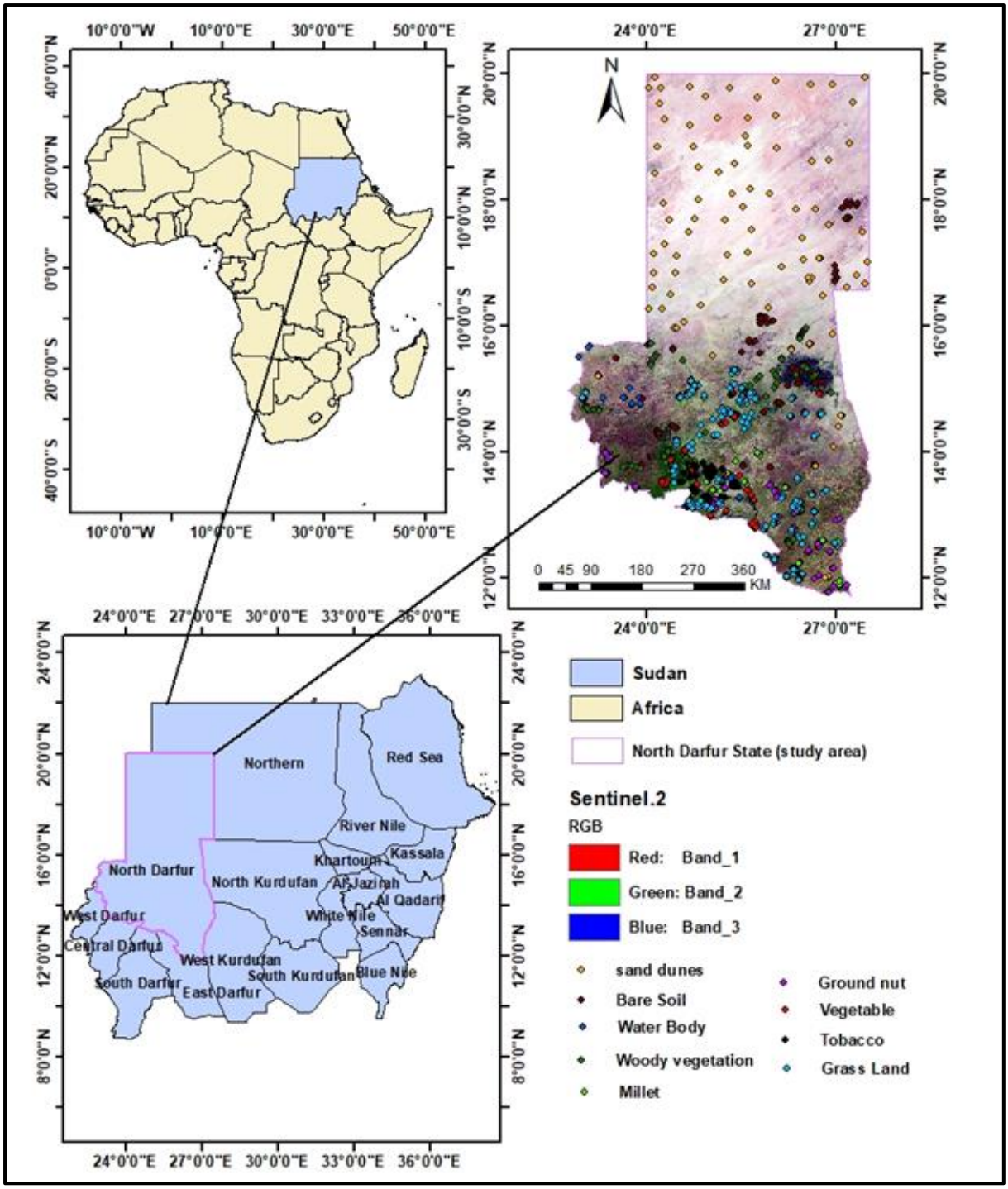


Figure 3.1. Geographical location of the study area in Sudan shown using Sentinel-2 (S2) false colour composite (RGB: 123).

The inter-tropical convergence zone's (ITCZ) seasonal movement and the southwest monsoon's northerly movement determine the rainfall pattern and amount in the arid and semi-arid North Darfur state. Rain falls in the summer, i.e., from June to October, with an average annual rainfall range of 152 mm in the north and 540 mm in the south, with wettest months

being July and August, where 80% of rainfall occurs (Kevane and Gray, 2008). The average annual temperature ranges from 42 °C in the hot months of April and May to 11 °C in the cold months of January and December (Mohmmed *et al.*, 2018). Rainfed agriculture sector is the key economic activities for 85% of the population in the North Darfur area; millet and groundnuts are planted mostly in goz lands, while cash crops and vegetables are grown in wadi lands (Osman and Cohen, 2014). These crops are substantial sources of food security, and their productivity mainly depends on land fertility and rainfall occurrence (Osman, 2012).

3.2.2 Data acquisition and pre-processing

Several Earth Observation Data (EOD) from the previous three decades, encompassing satellite images from popular platforms such as MODIS, Landsat, and Sentinel, as well as other geographical data, are stored in the cloud-based Google Earth Engine (GEE) environment (Loukika *et al.*, 2021). These data can be accessed in the GEE cloud database through https://earthengine.google.com/. In this study, Sentient-2 (S2) multispectral (MSI) Level-1C images were imported into the GEE platform and processed using the built-in .ee.Image Collection ("COPERNICUS/S2_SR") command. The S2 satellites were launched by the European Commission (EC) and the European Space Agency on 23 June 2015 (Sentinel-2A) and 07 March 2017 (Sentinel-2B) with a revisit frequency of 5 days (Inoue *et al.*, 2020; Xie *et al.*, 2022). The two satellites provide continually open-access multispectral data, with both high spatial, spectral, and temporal (10 days from one satellite and 5 days by both satellites) resolutions (Table 3.1). The S2 bands used in this study are blue (B2), green (B3), red (B4), vegetation red edge (B5, B6, B7, and B8A), near-infrared (B8), shortwave infrared (B11), and shortwave infrared (B12). Therefore, Top-of-Atmospheric- (TOA) corrected S2 (MSI-1C) data were obtained for 01/07/2022 to 30/09/2022 using GEE JavaScript-based environment, which was utilized to map crops in this study. More detail about spectral bands presented in Table 3.1.

Table 3.1: Properties of Sentinel-2 (S2) images used to map crop types in North Darfur State, Sudan.

Bands	Description	Abbreviation	Resolution (m)	Central Wavelength (nm)
Band 1	Coastal aerosol	C	60	443.9 (S2A)/ 442.3 (S2B)
Band 2	Blue	B	10	496.6 (S2A)/492.1 (S2B)
Band 3	Green	G	10	560 (S2A)/559 (S2B)
Band 4	Red	R	10	664.5 (S2A)/665 (S2B)
Band 5	Vegetation Red Edge	VRE	20	703.9 (S2A)/703.8 (S2B)

Band 6	Vegetation Red Edge	VRE	20	740.2 (S2A)/739.1 (S2B)
Band 7	Vegetation Red Edge	VRE	20	782.5 (S2A)/779.7 (S2B)
Band 8	Near-infrared	NIR	10	835.1 (S2A)/833 (S2B)
Band 8A	Vegetation Red Edge	VRE	20	864.8 (S2A)/864 (S2B)
Band 9	Water vapor	W	60	945 (S2A)/943.2 (S2B)
Band 10	Shortwave–Cirrus	SWIR–C	60	1373.5 (S2A)/ 1376.9 (S2B)
Band 11	Shortwave Infrared	SWIR	20	1613.7 (S2A)/1610.4 (S2B)
Band 12	Shortwave Infrared	SWIR	20	2202.4(S2A)/2185.7 (S2B

This study applied radiometric and geometric corrections, including orthorectification and spatial registration to a global reference system with sub-pixel accuracy for the Sentinel-2 MSI Level-1C TOA reflectance images. Because optical remote sensing (RS) images are greatly affected by cloud conditions, pixels heavily affected by dense and cirrus clouds were removed from all Sentinel-2 MSI images by applying the QA60 Quality Assessment band. All 20 m resolution bands were resampled to 10 m resolution bands by using the nearest neighbour method. This resampling algorithm has been widely used, due to its easy implementation and spectral information conservation (Roy *et al.*, 1994). The 'filter' function was applied to filter and mosaic images. The date parameters (start and end) were set to cover the period from June 1st to September 30th, 2022. The 'filter. Bound ()' function was utilized to crop filtered images to match the boundaries of the study area. The resulting stacked images were normalized to account for illumination variations and reduce clouds presence. Composite imagery was generated using the median reducer to produce cloud-free composites (Abubakar *et al.*, 2023). A median value is assigned to each pixel for the entire stack of images, resulting in a single image for the entire image collection. According to the local agricultural calendar, the growing season of crops is four months, i.e., June to September; this is considered the rain season, and it offers few cloud-free days for acquiring optical remotely sensed data. Therefore, S2 images of minimal cloud cover (<10%) of the study area finally, to attain quality results, image enhancement and smoothing were performed. The image acquisition dates correspond to the sprouting and/or harvesting time of crops in order to make discrimination between them easier (Abubakar *et al.*, 2023; Mazarire *et al.*, 2020).

The study selected S2 images because its bands are more suitable for monitoring vegetation, wavelength sensitivity to chlorophyll content and phonological state and also its finer spatial resolution compared to other satellite images (Sánchez-Espinosa *et al.*, 2019). Eight most widely used vegetation indices (VIs), i.e., normalised difference vegetation index (NDVI) (Rouse *et al.*, 1974), enhanced vegetation index (EVI) (Huete *et al.*, 2002; Praticò *et al.*, 2021), and soil-adjusted vegetation index (SAVI) (Huete, 1988) were computed from the

S2 dataset. Others were the green normalised difference vegetation index (GNDVI) (Gitelson *et al.*, 1996), weighted difference vegetation index (WDVI) (Richardson *et al.*, 1977), red edge NDVI (NDVIre) (Frampton *et al.*, 2013), ratio-vegetation index (RVI) (Jordan, 1969), and normalised difference infrared index (NDII) (Kimes *et al.*, 1981). Table 3.2 shows the equations used to calculate the VIs adopted in this work and computed in GEE.

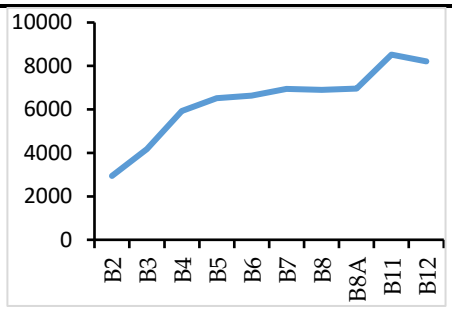
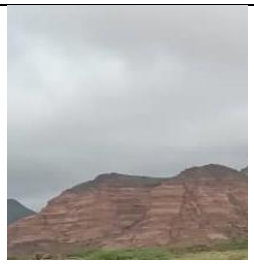
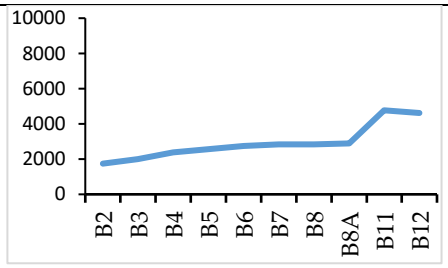
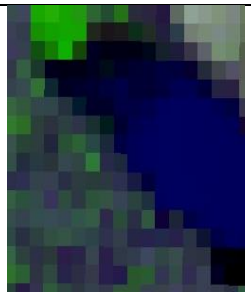
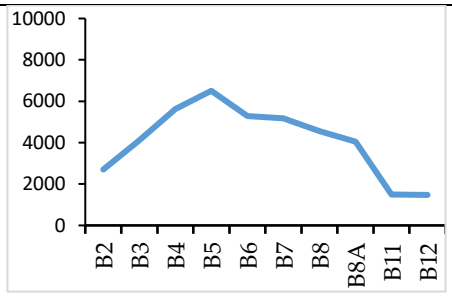
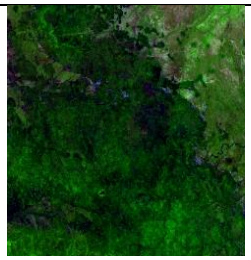
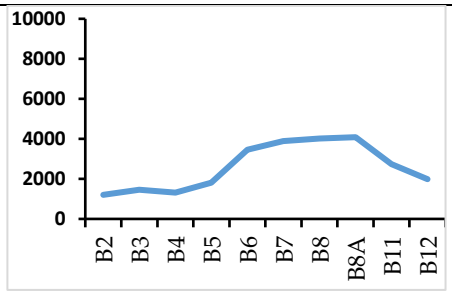
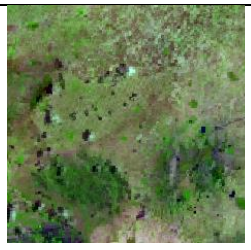
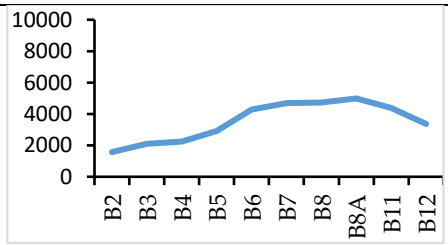
Table 3.2: The vegetation indices (VIs) applied in this work and computed in the Google Earth Engine (GEE); NIR near-infrared, SWIR shortwave infrared.

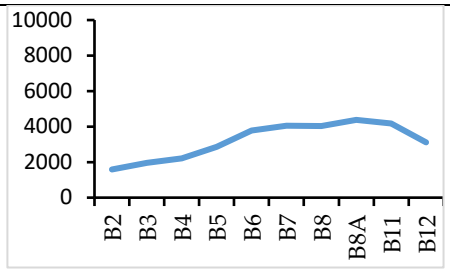
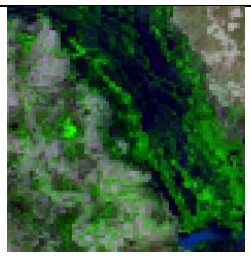
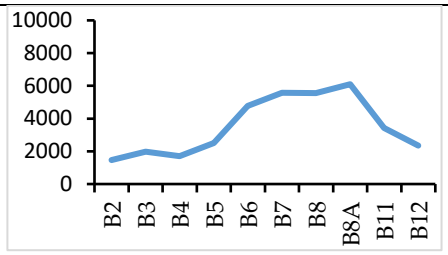
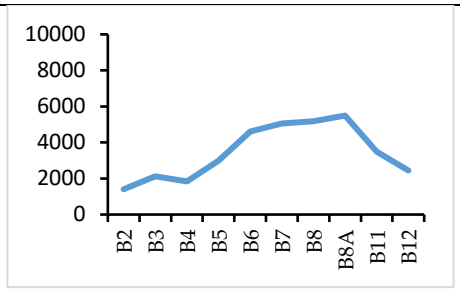
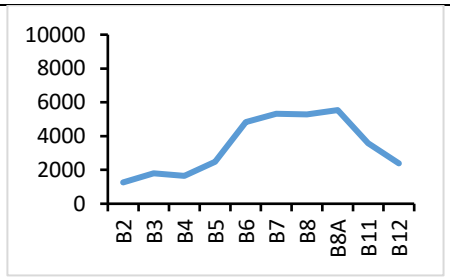
Vegetation index	Abbreviation	Formula	Equation #	Reference
Normalised difference vegetation index	NDVI	$\frac{NIR-Red}{NIR+Red}$	(3.1)	(Rouse *et al.*, 1974)
Enhanced vegetation index	EVI	$\frac{2.5 \times (NIR-Red)}{NIR + 6.0\times Red - 7.5 \times Blue + 1}$	(3.2)	(Huete *et al.*, 2002)
Soil-adjusted vegetation index	SAVI	$\frac{1.5 \times ((NIR-Red))}{((NIR + Red+1.5))}$	(3.3)	(Huete, 1988)
Green normalised difference vegetation index	GNDVI	$\frac{NIR-Green}{NIR+Green}$	(3.4)	(Gitelson *et al.*, 1996)
Weighted difference vegetation index	WDVI	$\frac{NIR}{Green}$	(3.5)	(Richardson and Wiegand, 1977)
Rededge NDVI	NDVIre	$\frac{\text{Rededge} - \text{Red}}{\text{Rededge} + \text{Red}}$	(3.6)	(Frampton *et al.*, 2013)
Ratio-vegetation index	RVI	$\frac{NIR}{Red}$	(3.7)	(Jordan, 1969)
Normalised difference infrared index	NDII	$\frac{NIR-SWIR\,1}{NIR+SWIR\,1}$	(3.8)	(Kimes *et al.*, 1981)

3.2.3 Acquisition of ground control data

To improve the quality of classification results, the choice of validation and training points is a critical step (Praticò *et al.*, 2021). The target crops were millet (MI), groundnut (GN), vegetables (VE) and tobacco (TO). Other land cover classes include dunes (SD), bare soil (BS), water body (WB), woody vegetation (WV), and grassland (GL). This study collected ground control data of the different crops (Table 3.3) in the field in June–September 2022 using a hand-held Global Positioning System (eTrex® 20 GPS Receiver; Garmin, Olathe, KS, USA). Because North Darfur is expansive, the remaining sample data were generated via on-screen digitization on Google earth and Sentinel-2 MSI images, closely guided by visual interpretation, knowledge of the study area, and expert opinion (Figure 3.1). A total of 2824 samples were shared between training and testing datasets, i.e., 70% (1977) and 30% (847), respectively. Mean reflectance curves were constructed from Sentinel-2 dataset using reference ground control points (Table 3.3).

Table 3.3: Reference data for cropland sites and common land cover/land use classes. The mean reflectance curves were constructed using spectral data Sentinel-2 Multi-Spectral Instrument (MSI) dataset using reference points.

Crops / Other land use land cover (LULC)	Field observation images	Earth observation (sentinel-2 images)	Spectral reflectance curves	Total sample points
Sand dunes (SD)				686
Bare Soil (BS)				346
Water body (WB)				110
Woody vegetation (WV)				480
Millet (MI)				358

Groundnuts (GN)				111
Vegetables (VE)				112
Tobacco (TO)				95
Grassland (GL)				526

Typical images of crop and coexisting LULC were taken during the field survey to study area in September 2022

3.2.4 Crop type mapping

To map crop types, five pixel-oriented classification models based on RF and SVM algorithms were trained and evaluated using the ground truth data collected in the field. The five data subsets extracted from the S2 MSI dataset are: (1) the visible and near-infrared (VNIR) bands, (2) visible and shortwave infrared (VSWIR) bands, (3) ten S2 bands, i.e., blue (band 2), green (band 3), red (band 4), vegetation red edge (bands 5, 6, 7, and B8A), near-infrared (band 8), shortwave infrared (band 11), and shortwave infrared (band 12), (4) eight vegetation indices (VIs), and (5) ten S2 bands + eight vegetation indices. The five models were later compared for crop type mapping in North Darfur State.

3.2.5 Image classification

Two supervised machine learning (ML) algorithms available in the GEE platform were selected based on their different classification mechanisms, resulting in different nonlinear or linear boundaries for the same data and performed in GEE (Gorelick *et al.*, 2017). Random Forest (RF) has been one of the ensemble learning techniques that built numerous classifiers and has been proven to improve classification accuracy. RF classifier employs a bagging (bootstrap aggregation) operation where a number of trees (*ntree*) are constructed based on a random subset of samples derived from the training data (Foody, 2002). Each tree is independently grown to maximum size based on a bootstrap sample from the training dataset without pruning. Each node is split using the best among a subset of input variables (*mtry*) (Breiman *et al.*, 1984). Furthermore, the RF builds trees using randomly replaced bootstrapped comprising two thirds of the training samples, decreasing the variance in classification error (Genuer *et al.*, 2015). The RF has low sensitivity overtraining or noise and a high ability to handle high-dimensional data and its capacity to determine variable importance (Rodriguez-Galiano *et al.*, 2012; Xie and Niculescu, 2022). The support vector machine (SVM) classifier is a supervised classification algorithm used to solve classification and regression problems based on a statistical learning framework (Loukika *et al.*, 2021). It uses a hyperplane to classify the data points distinctly, and there are many possible methods for the hyperplane to separate the support vectors in which the key goal of SVMs is to find the hyperplane that has the maximum margin (Maxwell *et al.*, 2018; Shaharum *et al.*, 2020). The support machine learning comprises various hyperplane parameters such as kernel type, penalty value (*C*) and gamma (γ). These hyperparameters can be tuned and adjusted to improve the performance of SVM in classification images.

3.2.6 Accuracy assessment

Confusion matrices were generated using 30% of ground reference data, from which kappa coefficient (κ), overall accuracies (OA), user accuracies (UA), producer accuracy (PA) and F1 score were computed to assess the performance of the models (Table 3.4). Overall accuracy (OA) is defined as the proportion of the total number of correctly classified pixels to the total number of pixels (Foody, 2002). The κ presented the agreements between classification and truth values, while the PA reflects the conditional probability that a specific location on the

classification map output is consistent with any random sample in the test dataset. User accuracy (UA) consists of selecting a random sample with the same conditional probability as the actual type of ground from the classification maps (Rwanga *et al.*, 2017). The F1 score is an important metric that balances the difference between PA and UA for each class by formulating a harmonic mean.

Table 3.4: Confusion matrix equations used to calculate kappa (κ), overall accuracy (OA), producer accuracy (PA), user accuracy (UA), and F1 score.

Accuracy measure	Abbreviation	Formula	Equation #
Overall accuracy	OA	$(\frac{\sum_{i=1}^{n} Pii}{N}) \times 100$	(3.9)
Kappa	κ	$\frac{N\sum_{i=1}^{n} Pii - \sum_{i=1}^{n}(Pi+ \times P+i)}{N^2 - \sum_{i=1}^{n}(Pi+ \times P+i)}$	(3.10)
User accuracy	UA	$(\frac{Pii}{Pi+}) \times 100$	(3.11)
Producer accuracy	PA	$(\frac{Pii}{P+i}) \times 100$	(3.12)
F1-score	F1-score	$(\frac{AU \times PA}{AU+PA}) \times 2$	(3.13)

Where *n* is the total number of columns of the confusion matrix; *Pii* is the number of correctly classified upper crop type samples in the *i* row and *i* column of the confusion matrix, *Pi+* and *P+i* are the total number of crop-type samples in row i and column *i*, and *N* is the total number of samples included for verification.

3.3 Results

3.3.1 Crop type classification maps

The classification maps of crops in the study area derived from optical Sentinel-2 (S2) data using random forest (RF) and support vector machine (SVM) in Google Earth Engine (GEE) are presented in Figure 3.2. However, the results from the two classifiers show that the spatial distribution of crops across the study area is depicted differently by different models; there are visually noticeable differences among the maps.

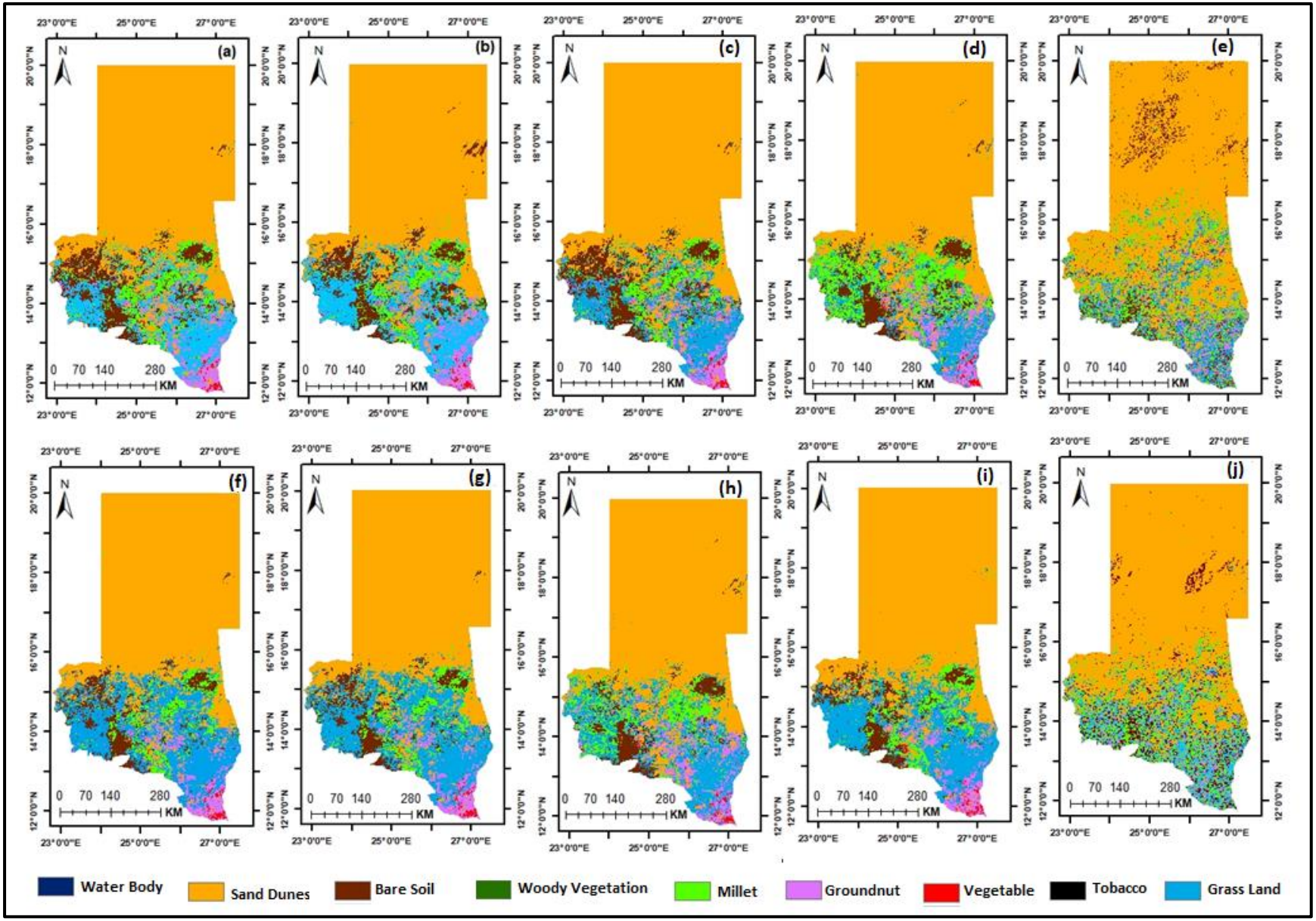


Figure 3.2. Classification results of spatial distribution of Crops based on the following datasets: (a) RF—10 Sentenil-2 (S2) bands, (b) RF—10 S2 bands + 8 vegetation indices (VIs), (c) RF—visible + near-infrared (VNIR) bands, (d) RF—visible + shortwave infrared (SWIR) bands, (e) RF—8 VIs; (f) SVM—10 S2 bands, (g) SVM—10 S2 bands + 8 VIs, (h) SVM—VNIR bands, (i) SVM—VSWIR bands (j) SVM—8 VIs for

2022 growing season in North Darfur, Sudan. The 10 S2 bands used— B2, B3, B4, B5, B6, B7, B8, B8A, B11, B12; 8 VIs used— normalised difference vegetation index (NDVI), enhanced vegetation index (EVI), soil-adjusted vegetation index (SAVI), green-normalised difference vegetation index (GNDVI, weighted Difference vegetation index (WDVI), red edge NDVI (NDVIre), ratio-vegetation index (RVI), and normalised difference infrared index (NDII); VNIR— visible and near-infrared; VSWIR— visible and shortwave.

The estimated area coverage for specific crop types in the classified maps derived from various datasets was assessed using the RF and SVM classifier algorithms. The corresponding results are presented in Tables 3.5 and 3.6, respectively. Notably, there are differences in the area covered by each specific crop. For example, millet covered 1, 359, 488 ha using ten Sentenil-2 bands (bands 2, 3, 4, and 8 represent blue, green, red, and near-infrared bands, respectively, while bands 5, 6, 7, and 8A are vegetation red edge bands, and bands 11 and 12 are shortwave), but 1, 426, 106 ha by VSWIR (visible and shortwave infrared) bands (Table 3.5). Groundnuts occupied 249, 525 ha, as shown by a combination of ten S2 bands and eight vegetation indices (VIs), but the VIs alone indicate that groundnuts covered 576, 358 ha. Similarly, tobacco had varied spatial distribution in the study area; a combination of ten S2 bands and eight VIs showed tobacco covered 53, 069 ha, while VIs alone showed 186, 006 ha

Table 3.5: Total estimated area (in ha) of crop types in the classified maps derived from various datasets using random forest (RF) classifier; 10 Sentinel-2 (S2) bands used— B2, B3, B4, B5, B6, B7, B8, B8A, B11, B12; 8 vegetation indices (VIs) used— normalised difference vegetation index (NDVI), enhanced vegetation index (EVI), soil-adjusted vegetation index (SAVI), green-normalised difference vegetation index (GNDVI, weighted Difference vegetation index (WDVI), red edge NDVI (NDVIre), ratio-vegetation index (RVI), and normalised difference infrared index (NDII); VNIR— visible and near-infrared; VSWIR— visible and shortwave.

Class	10 S2 bands	Percent (%)	10 S2 bands + 8 VIs	Percent (%)	VNIR bands	Percent (%)	VSWIR bands	Percent (%)	8 VIs	Percent (%)
Sand dunes	14,644,714	63.40	14,348,403	62.12	14,543,447	62.96	14,443,447	62.53	13,896,840	60.16
Bare soil	1,929,655	8.35	1,915,642	8.29	1,561,230	6.76	1,661,230	7.19	1,826,934	7.91
Water bodies	320,097	1.38	401,163	1.73	158,517	0.69	158,517	0.68	320,167	1.39
Woody vegetation	1,609,335	6.96	1,408,074	6.096	2,354,865	10.19	2,254,865	9.76	2,191,030	9.49
Millet	1,359,488	5.88	1,395,427	6.041	1,326,106	5.74	1,426,106	6.17	1,412,910	6.12
Ground nuts	247,465	1.07	249,525	1.08	275,805	1.19	265,805	1.15	576,358	2.49
Vegetables	218,062	0.94	206,000	0.89	200,693	0.87	220,693	0.96	307,879	1.33
Tobacco	94,736	0.41	53,069	0.23	171,287	0.74	161,287	0.69	186,006	0.81
Grassland	2,672,786	11.57	3,119,035	13.50	2,504,388	10.84	2,504,388	10.84	2,378,214	10.29
Total	23,096,338	100.00	23,096,338	100.00	23,096,338	100.00	23,096,338	100.00	23,096,338	100.00

The SVM classifier showed that millet covered 1, 277,434 ha using ten S2 bands. However, VSWIR bands showed it was 1, 189,634 ha. Additionally, the groundnut area was estimated as 401 928 ha by ten S2 bands, while the ten S2 bands alone showed 311, 928 ha. The area covered by vegetables and tobacco was in the range 160, 587-254, 763 ha and 48, 442-104, 417 ha, respectively, as indicated by the various datasets.

Table 3.6: Total estimated area (in ha) of crop types in the classified maps derived from various datasets using support vector machine (SVM) classifier: 10 Sentinel-2 (S2) bands used— B2, B3, B4, B5, B6, B7, B8, B8A, B11, B12; 8 vegetation indices (VIs) used— normalised difference vegetation index (NDVI), enhanced vegetation index (EVI), soil-adjusted vegetation index (SAVI), green-normalised difference vegetation index (GNDVI, weighted Difference vegetation index (WDVI), red edge NDVI (NDVIre), ratio-vegetation index (RVI), and normalised difference infrared index (NDII); VNIR— visible and near-infrared; VSWIR— visible and shortwave.

Class	10 S2 bands	Percent (%)	10 S2 bands + 8 VIs	Percent (%)	VNIR bands	Percent (%)	VSWIR bands	Percent (%)	8 VIs	Percent (%)
Sand dunes	14,189,862	61.44	14,289,862	61.87	14,298,619	61.91	14,513,962	62.84	14,448,059	62.56
Bare soil	1,602,201	6.94	1,302,201	5.64	1,329,330	5.76	1,513,054	6.55	1,842,476	7.98
Water bodies	235,274	1.02	234,274	1.01	193,532	0.84	228,867	0.99	373,776	1.62
Woody vegetation	1,427,283	6.18	1,428,283	6.18	1,992,935	8.63	1,540,794	6.67	1,820,599	7.88
Millet	1,277,434	5.53	1,487,434	6.44	1,546,018	6.69	1,189,634	5.15	1,367,438	5.92
Groundnuts	311,928	1.35	401,928	1.74	253,456	1.10	267,919	1.16	214,899	0.93
Vegetables	182,557	0.79	192,557	0.83	254,763	1.10	203,773	0.88	160,587	0.69
Tobacco	58,442	0.25	48,442	0.21	104,417	0.45	61,512	0.27	98,635	0.42
Grassland	3,811,357	16.50	3,711,357	16.07	3,123,268	13.52	3,576,823	15.49	2,769,869	11.99
Total	23,096,338	100.00	23,096,338	100.00	23,096,338	100.00	23,096,338	100.00	23,096,338	100.00

3.3.2 Classification accuracy

The performance of the various data sets classified using RF and SVM algorithms was compared and presented in Table 3.7, 3.8, and 3.9. The RF classifier obtained the best accuracy score of 97.1% using VNIR (visible and near-infrared) bands (Table 3.7). The VIs composite performed the least of the datasets. Both producer accuracy (PA) and user accuracy (UA) ranged from 83-98% (Table 3.9). Generally, VIs scored relatively lower PA and UA values than S2 multispectral bands. Tobacco and groundnuts reported the lowest PA and UA values. Table 3.10 shows the F1 scores used to assess class-wise performance for RF and SVM classifiers using five different datasets, i.e., VNIR bands, VSWIR bands, ten S2 multispectral bands, eight VIs, and ten S2 bands + eight VIs. Groundnuts reported the highest F1 score, i.e., 0.98 from the ten S2 multispectral bands. Again, VIs performed poorly compared to the optical datasets.

Table 3.7: Confusion matrices for random forest (RF) models used to map crop types in North Darfur State, Sudan for 2022 growing season; SD—sand dunes, BS—bare soil, WB—water bodies, WV—woody vegetation, MI—millet, GN—groundnuts, VE—vegetables, TO—tobacco, GL—grassland. 10 Sentinel-2 (S2) bands used— B2, B3, B4, B5, B6, B7, B8, B8A, B11, B12; 8 vegetation indices (VIs) used— normalised difference vegetation index (NDVI), enhanced vegetation index (EVI), soil-adjusted vegetation index (SAVI), green-normalised difference vegetation index (GNDVI, weighted Difference vegetation index (WDVI), red edge NDVI (NDVIre), ratio-vegetation index (RVI), and normalised difference infrared index (NDII).

				10 Sentiel-2 bands					
Classes	SD	BS	WB	WV	MI	GN	VE	TO	GL
SD	477	1	0	1	3	0	0	0	1
BS	2	215	0	2	1	0	0	2	2
WB	0	1	78	0	0	0	0	0	0
WV	1	6	0	332	0	0	0	0	1
MI	2	0	1	2	244	1	0	0	2
GN	0	0	0	0	1	71	0	0	0
VE	1	0	1	1	1	0	68	0	1
TO	0	0	0	1	0	0	2	58	0
GL	1	5	1	4	1	0	2	0	331
Total	484	228	81	343	251	72	72	60	338
Overall accuracy (OA) 97%									
Kappa Coefficient (κ) 0.96									
				10 Sentienl-2 (S2) bands + 8 vegetation indices (VIs)					
	SD	BS	WB	WV	MI	GN	VE	TO	GL
SD	467	3	1	2	3	3	1	0	3
BS	8	202	2	6	0	0	0	0	6
WB	1	2	72	1	1	0	0	0	2
WV	2	9	0	324	0	0	0	1	4

MI	3	1	0	3	239	2	1	1	2
GN	0	0	0	1	5	65	0	0	1
VE	0	1	1	1	1	0	64	1	4
TO	0	2	0	4	0	0	1	53	1
GL	8	8	0	9	2	1	0	0	317
Total	489	228	76	351	251	71	67	56	340

Overall accuracy (OA) 96.5%
Kappa Coefficient (κ) 0.94

Visible + near-infrared (VNIR) bands

	SD	BS	WB	WV	MI	GN	VE	TO	GL
SD	475	1	0	2	3	1	0	0	1
BS	2	214	0	3	0	0	0	1	4
WB	0	1	78	0	0	0	0	0	0
WV	3	9	0	324	2	0	1	0	1
MI	0	1	1	2	247	0	0	0	1
GN	0	0	0	0	4	68	0	0	0
VE	1	0	1	0	2	0	68	1	0
TO	0	0	1	1	0	0	1	58	0
GL	3	4	1	3	3	1	0	0	330
Total	484	230	82	335	261	70	70	60	337

Overall accuracy (OA) 97.1%
Kappa Coefficient (κ) 0.95

Visible +shortwave infrared (VSWIR) bands

	SD	BS	WB	WV	MI	GN	VE	TO	GL
SD	475	2	0	2	3	1	0	0	0
BS	3	212	1	3	0	0	0	2	3
WB	1	0	78	0	0	0	0	0	0
WV	1	10	0	324	0	0	0	1	4
MI	0	0	1	0	245	1	0	0	5
GN	0	0	0	0	4	67	0	0	1
VE	1	0	1	0	0	0	69	0	2
TO	0	0	0	2	0	0	2	57	0
GL	2	6	2	4	6	2	0	0	323
Total	483	230	83	335	258	71	71	60	338

Overall accuracy (OA) 96.5%
Kappa Coefficient (κ) 94%

8 vegetation indices (VIs)

	SD	BS	WB	WV	MI	GN	VE	TO	GL
SD	460	4	0	7	4	0	1	2	5
BS	16	171	3	9	8	5	2	0	10
WB	1	0	78	0	0	0	0	0	0
WV	19	9	1	302	5	0	0	0	4
MI	5	2	1	4	234	1	0	1	4
GN	1	2	0	1	3	62	1	0	2
VE	2	1	1	1	3	0	64	1	0
TO	1	0	1	4	3	0	1	51	0
GL	11	5	2	11	10	2	3	2	299
Total	516	194	87	339	270	70	72	57	324

Overall accuracy (OA) 90%
Kappa coefficient (κ) 0.87

However, Table 3.8 results show that the SVM classifier's best overall accuracy (OA) was 95%, achieved by combining ten S2 bands and eight vegetation indices. Like with the RF classifier, the VI data set performed the least, achieving an OA value of 84%. The PA was 81-

94%, while UA ranged between 87% and 97% (Table 3.9). Generally, VIs scored relatively lower PA and UA values than S2 multispectral bands. Yet again, tobacco and groundnuts reported the lowest PA and UA values, while the S2 multispectral bands outperformed the VIs dataset. Millet and vegetables reported the highest F1 score, i.e., 0.94, each, by VNIR bands and the ten S2 bands/eight VIs dataset, respectively (Table 3.10).

Table 3.8: Confusion matrices for support vector machine (SVM) models used to map crop types in North Darfur State, Sudan for 2022 growing season; SD—sand dunes, BS—bare soil, WB—water bodies, WV—woody vegetation, MI—millet, GN—groundnuts, VE—vegetables, TO—tobacco, GL—grassland. 10 Sentinel-2 (S2) bands used— B2, B3, B4, B5, B6, B7, B8, B8A, B11, B12; 8 vegetation indices (VIs) used— normalised difference vegetation index (NDVI), enhanced vegetation index (EVI), soil-adjusted vegetation index (SAVI), green-normalised difference vegetation index (GNDVI, weighted Difference vegetation index (WDVI), red edge NDVI (NDVIre), ratio-vegetation index (RVI), and normalised difference infrared index (NDII).

				10 Sentienl-2 bands					
Classes	SD	BS	WB	WV	MI	GN	VE	TO	GL
SD	467	3	1	2	3	3	1	0	3
BS	8	202	2	6	0	0	0	0	6
WB	1	2	72	1	1	0	0	0	2
WV	2	9	0	324	0	0	0	1	4
MI	3	1	0	3	239	2	1	1	2
GN	0	0	0	1	5	65	0	0	1
VE	0	1	1	1	1	0	64	1	4
TO	0	2	0	4	0	0	1	53	1
GL	8	8	0	9	2	1	0	0	317
Total	490	228	76	351	251	71	67	56	340
Overall accuracy (OA) 93%									
Kappa coefficient (κ) 0.92									
				10 Sentienl-2 bands+ 8 vegetation indices					
	SD	BS	WB	WV	MI	GN	VE	TO	GL
SD	465	6	1	3	3	1	1	1	2
BS	6	207	2	0	1	4	2	1	1
WB	0	2	74	1	0	0	2	0	0
WV	1	10	3	317	1	0	3	2	3
MI	3	4	3	0	225	4	6	3	4
GN	0	1	1	0	0	63	3	0	4
VE	0	1	2	2	1	0	64	3	0
TO	0	3	0	1	0	0	0	56	1
GL	3	5	6	8	2	1	2	3	315
Total	478	239	92	332	233	73	83	69	330
Overall accuracy (OA) 95%									
Kappa coefficient (κ) 0.94									
				Visible + near-infrared bands					
	SD	BS	WB	WV	MI	GN	VE	TO	GL
SD	466	2	1	3	1	2	1	0	7
BS	5	200	2	6	2	0	2	0	7
WB	0	1	75	1	0	0	1	0	1
WV	8	9	0	320	0	0	0	1	2
MI	6	1	0	3	237	3	0	1	1
GN	2	0	0	1	2	64	0	0	3
VE	0	1	1	3	0	0	65	1	2
TO	0	2	0	3	1	0	1	54	0
GL	11	5	2	3	5	2	0	0	317

Total	498	221	81	343	248	71	70	57	340
Overall accuracy (OA) 93% **Kappa coefficient (κ) 0.91**									
	Visible + shortwave infrared bands								
	SD	BS	WB	WV	MI	GN	VE	TO	GL
SD	471	2	0	1	4	2	0	0	3
BS	6	194	1	14	1	0	0	0	8
WB	1	0	73	1	3	0	0	0	1
WV	3	9	2	320	0	0	0	0	6
MI	4	1	1	5	228	4	2	1	6
GN	2	0	0	0	7	61	1	0	1
VE	1	1	0	2	0	0	64	1	4
TO	0	3	0	2	0	0	1	54	1
GL	7	7	1	7	5	2	0	0	316
Total	495	217	78	352	248	69	68	56	346
Overall accuracy (OA) 92% **Kappa coefficient (κ) 0.90**									
	8 vegetation indices								
	SD	BS	WB	WV	MI	GN	VE	TO	GL
SD	460	2	2	7	6	1	1	0	4
BS	14	179	1	9	6	2	0	1	12
WB	0	0	78	0	0	0	0	1	0
WV	9	8	1	307	5	0	1	0	9
MI	3	2	1	6	236	1	1	0	2
GN	0	1	0	0	5	63	1	0	2
VE	1	2	1	2	2	1	62	1	1
TO	2	3	0	2	1	0	1	52	0
GL	9	12	5	9	10	2	2	2	294
Total	498	209	89	342	271	70	69	57	324
Overall accuracy (OA) 84% **Kappa coefficient (κ) 0.81**									

Table 3.9: The user and producer accuracy performance of random forest (RF) and support vector machine (SVM) using various datasets; SD—sand dunes, BS—bare soil, WB—water bodies, WV—woody vegetation, MI—millet, GN—groundnuts, VE—vegetables, TO—tobacco, GL—grassland, S2—Sentinel-2, VI—vegetation index, VNIR—visible and near-infrared, VSWIR—visible and shortwave, RF—random forest, SVM—support vector machine. 10 S2 bands used— B2, B3, B4, B5, B6, B7, B8, B8A, B11, B12; 8 VIs used— normalised difference vegetation index (NDVI), enhanced vegetation index (EVI), soil-adjusted vegetation index (SAVI), green-normalised difference vegetation index (GNDVI, weighted Difference vegetation index (WDVI), red edge NDVI (NDVIre), ratio-vegetation index (RVI), and normalised difference infrared index (NDII).

	(a) RF Producers Accuracy					**(b) RF Users Accuracy**				
Class	10 S2 bands	10 S2 bands+8 VIs	VNIR bands	VSWIR bands	8 VIs	10 S2 bands	10 S2 bands + 8 VIs	VNIR bands	VSWIR bands	8 VIs
SD	0.98	0.98	0.98	0.98	0.95	0.98	0.98	0.98	0.98	0.91
BS	0.96	0.94	0.95	0.95	0.80	0.94	0.92	0.93	0.93	0.86
WB	0.98	100	0.98	0.97	0.97	0.96	0.96	0.95	0.96	0.92
WV	0.97	0.95	0.95	0.96	0.88	0.96	0.95	0.96	0.95	0.86
MI	0.96	0.97	0.98	0.96	0.92	0.97	0.94	0.94	0.93	0.88
GN	0.98	0.93	0.94	0.91	0.83	0.98	0.94	0.97	0.97	0.88
VE	0.93	0.94	0.93	0.93	0.87	0.94	0.97	0.97	0.97	0.91
TO	0.95	0.93	0.95	0.91	0.83	0.96	0.95	0.96	0.98	0.83
GL	0.96	0.93	0.95	0.98	0.86	0.97	0.95	0.97	0.98	0.91
	(a) SVM Producers Accuracy					**(a) SVM Users Accuracy**				
SD	0.96	0.97	0.96	0.97	0.95	0.95	0.99	0.93	0.95	0.89
BS	0.90	0.94	0.89	0.86	0.78	0.88	0.90	0.90	0.89	0.84
WB	0.91	0.88	0.94	0.92	0.89	0.94	0.93	0.92	0.93	0.85
WV	0.95	0.92	0.94	0.94	0.88	0.92	0.94	0.94	0.90	0.85
MI	0.94	0.91	0.94	0.90	0.89	0.95	0.94	0.95	0.91	0.89
GN	0.90	0.91	0.88	0.84	0.81	0.91	0.93	0.90	0.88	0.87
VE	0.87	0.96	0.89	0.87	0.82	0.95	0.92	0.92	0.94	0.91
TO	0.86	0.86	0.88	0.88	0.82	0.94	0.97	0.94	0.96	0.88
GL	0.91	0.96	0.91	0.91	0.83	0.93	0.91	0.93	0.91	0.91

Table 3.10: F1 scores class-wise performance of random forest (RF) and support vector machine (SVM) algorithms using five different datasets; SD—sand dunes, BS—bare soil, WB—water bodies, WV—woody vegetation, MI—millet, GN—groundnuts, VE—vegetables, TO—tobacco, GL—grassland, S2—Sentinel-2, VI—vegetation index, VNIR—visible and near-infrared, VSWIR—visible and shortwave. 10 S2 bands used—B2, B3, B4, B5, B6, B7, B8, B8A, B11, B12; 8 VIs used—normalised difference vegetation index (NDVI), enhanced vegetation index (EVI), soil-adjusted vegetation index (SAVI), green-normalised difference vegetation index (GNDVI, weighted Difference vegetation index (WDVI), red edge NDVI (NDVIre), ratio-vegetation index (RVI), and normalised difference infrared index (NDII).

Class	Random forest (RF)					Support vector machine (SVM)				
	10 S2 bands	10 S2 bands + 8 VIs	VNIR	VSWIR	8 VIs	10 S2 bands	10 S2 bands + 8 VIs	VNIR	VSWIR	8 VIs
SD	0.98	0.98	0.98	0.98	0.93	0.95	0.98	0.94	0.95	0.92
BS	0.95	0.93	0.93	0.93	0.83	0.89	0.92	0.89	0.87	0.81
WB	0.97	0.90	0.96	0.95	0.94	0.92	0.90	0.92	0.92	0.87
WV	0.96	0.95	0.95	0.96	0.87	0.93	0.93	0.94	0.91	0.86
MI	0.96	0.95	0.95	0.94	0.89	0.94	0.92	0.94	0.90	0.89
GN	0.98	0.93	0.95	0.93	0.85	0.90	0.92	0.88	0.85	0.84
VE	0.93	0.95	0.94	0.94	0.89	0.90	0.94	0.90	0.90	0.86
TO	0.95	0.94	0.95	0.93	0.83	0.90	0.91	0.90	0.91	0.85
GL	0.96	0.93	0.95	0.97	0.88	0.92	0.93	0.91	0.91	0.87

3.4 Discussion

This study aimed to use Google Earth Engine (GEE) to compute metrics used in mapping crop types in North Darfur State, Sudan, using datasets extracted from high-resolution Sentinel-2 (S2) data. Two machine learning (ML) classification algorithms, i.e., random forest (RF) and support vector machine (SVM), were used. The application of ML algorithms in mapping the spatial distribution of crops has increased in the last three decades (Loukika *et al.*, 2021; Rao *et al.*, 2021). However, mapping crops in highly heterogeneous arid environments is difficult due to the similarity of the reflectance value of the pixels (Ozdogan, 2010). Also, remote sensing (RS) data for agriculture monitoring faces high-cost constraints (Khanal *et al.*, 2020). Open access RS datasets and the computing power of the GEE platform provide free access to vast volumes of satellite data and facilitate powerful processing of big geo data covering large areas (Abubakar *et al.*, 2023; Pimple *et al.*, 2018; Shelestov *et al.*, 2017; Sujud *et al.*, 2021).

The successful launch of the satellite constellation of Sentinel-2A & B by the European Space Agency (ESA) has provided unprecedented high spatial, temporal and spectral resolution data for land applications and has shown their potential in diverse applications such as agriculture (Bontemps *et al.*, 2015; Defourny *et al.*, 2019; Segarra *et al.*, 2020; Vuolo *et al.*, 2018). The visible and near-infrared (VNIR) bands of S2 represent a promising data source for mapping crop types in regions characterized by small field areas (Tran *et al.*, 2022). The S2'S VNIR and the ten S2 bands (B2, B3, B4, B5, B6, B7, B8, B8A, B11, B12) datasets reported relatively higher classification accuracies than the other datasets for the RF classifier, i.e., 97.1% and 97%, respectively (Tables 3.7 and 3.8). An integrated dataset comprising ten S2 bands and eight vegetation indices (VIs) achieved the same overall accuracy (OA) as the VSWIR dataset, i.e., 96.5%. Therefore, VIs in the ten S2 bands/VIs dataset improved the negative effects associated with large sets of correlated variables and decreased the classification accuracies (Tables 3.7, 3.8 and 3.10). The eight VIs dataset reported the lowest classification accuracies reported by both RF and SVM. Hence, the classification accuracies for the VIs dataset did not achieve the highest levels, as indicated in the studies by Kobayashi *et al*. (Kobayashi *et al.*, 2020) and Zhang *et al*. (Zhang *et al.*, 2020); but the findings of the current study agree with (Pasternak *et al.*, 2022). Also, SWIR (shortwave infrared) bands had the same effect because of redundant information. Hence, the utilization of additional variables does not necessarily improve classification accuracy (Pasternak and Pawluszek-Filipiak, 2022).

The results of this study are in line with previous studies conducted by Praticò et al.; Rao et al., (Praticò *et al.*, 2021; Rao *et al.*, 2021) whom reported that the optical images was able to map cropland types at the field-scale with high accuracy in smallholder systems. Also the study results are in agreement with Sujud *et al.*(Sujud *et al.*, 2021) who achieved high classification accuracies using machine learning classifiers while mapping crop types using S2 data.

Overall, the RF algorithm offered the best model for mapping crops than SVM, although the gap between the two was not significant. The RF combine numerous soft linear boundaries at the surface of decision, while SVM performs well with sparse training, making it a better choice when less data are available (Shetty, 2019). Random Forest algorithm is resilient and less affected by parameters, while SVM is more sensitive to hyperparameters (Chang *et al.*, 2019). Considering the total area occupied by each crop type (Tables 3.5 and 3.6), it can observed that the two classifiers produced quite different results. Based on the classified maps, the results show that there existed confusion among classes; due to similarity of reflectance by different classes, e.g., tobacco and vegetables. Based on results presented in Tables 3.9 and 3.10, millet recorded highest producer accuracy (PA), user accuracy (UA), and F1 scores, followed by groundnuts; the reason could be due to their unique reflectance characteristics, and higher number of ground reference data, especially for millet (groundnuts class had comparatively fewer sample data collected in the field).

3.5 Conclusion

Accurate spatial distribution information for crops is important for agricultural management and food security. In this research, the mapping of crop types in North Darfur State was carried out using random forest (RF) and support vector machine (SVM) classifiers with the Sentinel-2 (S2) optical dataset within the Google Earth Engine (GEE) environment. By analysing and comparing classification performance, RF and SVM algorithms could map crops in the study area; the classifiers produced acceptable results. To enhance classification accuracy, images from key growth periods for each type of crop cultivated should be considered when designing methodologies for crop type mapping. However, data gaps in optical time series existed because of cloud contamination. Furthermore, reliable cloud and cloud shadow detection

algorithms are lacking. Future research will consider optical images from alternative sources, and the incorporation of radar images, which remain unaffected by time of day or weather conditions; data integration and more sophisticated data fusion techniques are required. Additionally, the reliance on error matrices to estimate classification accuracy based on field-collected samples introduces bias in conclusions. Consequently, future research will evaluate model performance using metrics such as balanced accuracy, bias score, Matthew's Correlation Coefficient, and others.

CHAPTER FOUR

Spatio-temporal Analysis of Drought and Impact on Millet Production across North Darfur State Using Standardized Precipitation Index (SPI) and Reconnaissance Drought Index (RDI)

This Chapter based on:
Altoom, M.B., Adam, E., & Ali, K.A. (under review). Spatio-temporal Analysis of Drought and Impact on Millet Production across North Darfur State Using Standardized Precipitation Index (SPI) and Reconnaissance Drought Index (RDI)

Abstract

Drought severely affects the agricultural sector, and it has been made worse by the global warming climate scenario. Drought has been chiefly studied globally and often overlooked at the local or regional scale. Therefore, accurate and timely characterization of agricultural drought at a local or regional scale is essential for developing adaptation and mitigation strategies. This study analyzed the spatio-temporal trend of drought events and their impact on millet production in North Darfur State, Sudan, from 1981 to 2020. The Standardized Precipitation Index (SPI) and the Reconnaissance Drought Index (RDI) for the 3-month (June-August), 6-month (June-November), and 9-month (June-February) timescales were used to assess the drought events. The drought-yield relationships were assessed using the Pearson correlation coefficients (r). Results indicate that the RDI index is more sensitive to rainfall variabilities than the SPI index for detecting drought trends. Drought events affected North Darfur over broad spatial extents, particularly in 1989, 1990, 1992, 1999, and 2001; an extreme drought event was in 2003. The correlation coefficient analysis (r) between the SPI and RDI, and the standardized variable of crop yield (SVCY) for millet grain yield showed a strong agreement between them. Moderate to extreme reductions in millet crop yield occurred in 1992, 1999, 2001, and 2003, corresponding to the moderate to extreme drought indicated by the RDI. Severe crop losses were in Kabkabiya and Umm Kadadda. This study contributes to a clearer understanding of drought impacts on the local scale and thus to insights into developing more effective and targeted management strategies and to enhancing crop resilience.

Keywords: North Darfur State, drought trends, millet yield, RDI, SPI, standardized variable of crop yield

4.1 Introduction

Drought is one of the most costly and little understood natural disasters, and it impedes long-term socioeconomic growth (Jiao *et al.*, 2019). Drought, one of the most common natural disasters, significantly impacts the agricultural economy (Yao *et al.*, 2018), vegetation degradation, and changes in the soil properties (Hedo de Santiago *et al.*, 2016; Zarch *et al.*, 2015). Depending on their different impacts, droughts are categorized into four drought types: agricultural, meteorological, hydrological, and socioeconomic droughts (Elhag and Zhang, 2018). Agricultural drought occurs due to soil moisture deficit at a critical time of the growing season, while meteorological drought results from reduced precipitation over an area (Hasan *et al.*, 2019). Hydrological drought arises from a reduction in groundwater and stream flow, and socioeconomic drought refers to the adverse effects of the above types of droughts on the lives of the human population (Hasan *et al.*, 2021; Heim Jr, 2002).

Droughts are slow-onset disasters—they neither have a clear beginning nor end—it is a creeping phenomenon that operates on different time scales and severely impacts economies. Drought causes more damage to agricultural productivity than other common disasters. Globally, from 1964 to 2007, crop yield was reduced by about 10% due to droughts (Lesk *et al.*, 2016). Studying droughts is crucial for evaluating agricultural production in countries that heavily rely on rainfed agriculture (Masupha *et al.*, 2018). Most sub-Saharan African countries, including Sudan, are adversely affected by recurrent droughts. Small-scale farming in Sudan is rainfed and, therefore, heavily relies on soil moisture and fertility (Edreira *et al.*, 2018; Elhag and Zhang, 2018). Sudan suffered from severe drought events during the 20th century, i.e., from 1972 to 1979 and 1980 to 1984 (Atiem *et al.*, 2022; Teklu *et al.*, 1992). Sudan experienced its worst drought in 1984, which led to a significant drop in crop production, and 4.5 million people suffered from hunger (Elhag and Zhang, 2018; Osman and Shamseldin, 2002). Sudan's Darfur region experiences exacerbated variability/reduction in rainfall, leading to frequent droughts and crop failure (Atiem *et al.*, 2022; Mohmmed *et al.*, 2018).

Several studies have demonstrated that droughts and subsequent land degradation in the Darfur region have led to resource conflicts (Dagne, 2009; Faris, 2007; Karamalla-Gaiballa and El-Kafafi, 2021). Therefore, , there is a need to evaluate drought impacts on agricultural

production and facilitate climate adaptation measures in the region (Selby *et al.*, 2014). Previous studies have examined the spatio-temporal patterns of drought status in the wide world using meteorological indicators (Abdelmalek *et al.*, 2020; Atiem *et al.*, 2022; Marini *et al.*, 2019b; Mohmmed *et al.*, 2018; Zarch *et al.*, 2015). Therefore, many indices are used for studying, evaluating, and monitoring drought. The Standardized Precipitation Index (SPI) has widely been used in characterizing drought on various time scales (McKee *et al.*, 1993). The SPI compares the amount of rainfall measured in a given location over several months to the distribution of precipitation in the long term for that time period. The Palmer Drought Severity Index (PDSI) utilizes precipitation and mean temperature to estimate long-term dryness (Palmer, 1965). PDSI timescale of about nine months makes it to inaccurately detect drought because it lacks long-term continuous soil moisture data and actual evapotranspiration. Also, PDSI assumes that all precipitation is rain (Yu *et al.*, 2019). The standardized water-level Index (SWI)) is computed using precipitation and PET (Bhuiyan *et al.*, 2006). To characterize drought, the Reconnaissance Drought Index (RDI) is calculated using precipitation and temperature data (Tigkas *et al.*, 2016; Zarch *et al.*, 2015). Determining a suitable drought index is vital in evaluating drought risk (Atiem *et al.*, 2022; Feng *et al.*, 2020). In regions with scarce and/or sparse meteorological stations, droughts are estimated by applying statistical methods by spatially interpolating spatial data. However, the interpolation process is affected by several factors, leading to high uncertainties (Rhee *et al.*, 2010).

Therefore, this study used SPI and RDI to assess drought events in North Darfur between 1981 and 2020. The RDI is best for smaller spatial-scale studies, while SPI is suited for comparing varying time scales (Merabti *et al.*, 2018). Although there are different indices in use today, SPI is widely accepted on the basis of its straightforward structure and because it uses solely precipitation data. Due to its being able to simulate the intensity of drought on spatial-temporal dimension, the World Meteorological Organization (WMO) in 2010 made the SPI a key meteorological drought indicator (Svoboda *et al.*, 2012). The temperature variations (minimum and maximum) and PET used to compute RDI play a role in determining the response of different crop varieties to drought (Peña-Gallardo *et al.*, 2019). Furthermore, PET is considered the main factor for agricultural studies (Adnan *et al.*, 2017). The RDI includes PET because drought severity may be as a result of other factors such as changes in temperature, speed of wind, humidity, and PET. The impact of drought on millet crop yield was assessed by examining the correlation between SPI-3, SPI-6, SPI-9, as well as RDI-3, RDI-

6, and RDI-9 values and the Standardised variable of crop yield (SVCY) from 1998 to 2020. The 3, 6, and 9 represent the months of June-August, June-November, and June-February, respectively.

4.2 Materials and Methods

4.2.1 Study area.

North Darfur State is situated in western Sudan at latitude 11° 45′ 49″-20° 00′ 30″ N and longitude 22° 46′ 47″-27° 29′ 47″ E as shown in (Figure 4.1). The State of North Darfur covers about half the territory of the Darfur—it borders West Darfur, South Darfur, East Darfur, Central Darfur, Northern, West Kordofan, and North Kordofan states. Also, North Darfur has a common border with Chad and Libya. The state has an area of *c*. 296,420 km^2 and an estimated population of 2.8 million in 2023. North Darfur has five districts, namely, Umm Kadadda, Kabkabiya, Kutum, Mellit, and AL Fashir (Mohmmed *et al.*, 2018; Young *et al.*, 2005). North Darfur includes part of the Mara Range (*Jebel Mara*), which dominates most of the west of the south. The state covers more than 50% of the territory of the Darfur region. Rainfall is slightly higher in the south, with variables of temperature and the crops grown include millet, maize, and peanuts. The northern region of the state is entirely a desert. The climate is predominantly hot, with long summers (Mohmmed *et al.*, 2018; Siddig, 2010).

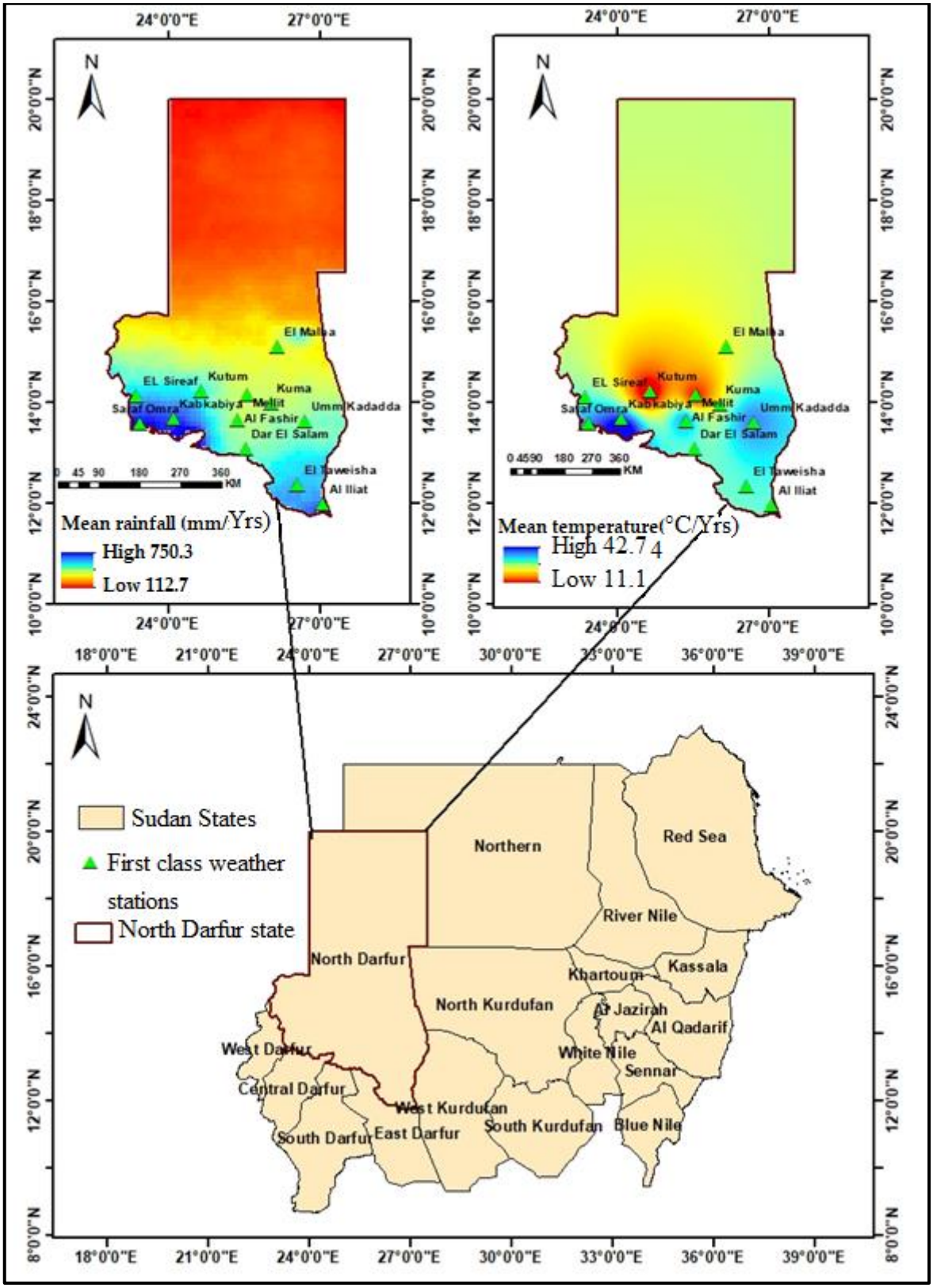


Figure 4.1. Map of the study area showing districts and distribution of first class weather stations in North Darfur State, Sudan, showing mean rainfall and mean temperature in the study area during the study period.

The distribution of precipitation in the region is characterized by high variability both temporally and spatially. The rainy season spans from June to October, with 70% of the rain in July and August. The growth season for millet extends from late June to October. The average annual rainfall in North Darfur ranges from 152 mm in EL Malha in the north to 630 mm in AL Liait in the south. During the summer, temperatures can reach a maximum of 42°C, while below 11°C in winter (Altoom *et al.*, 2023; Mohmmed *et al.*, 2018).

Rainfed agriculture is the primary livelihood for about 80% of the population in Darfur, and millet, a drought-resistant crop, serves as a major food and cash crop (Siddig, 2010; Young *et al.*, 2005). The soils in the south, low in fertility, are known as *goz* sands (Ibrahim, 1982; Siddig, 2010).

4.2.2 Dataset

Meteorological data from 1981 to 2020 from 11 weather stations distributed across five districts in North Darfur State were obtained from the Ministry of Agriculture (Figure 4.1). The data included monthly rainfall and minimum and maximum temperature. The missing monthly data in all weather stations amounted to less than 1%, and the missing data were interpolated using inverse distance weighting (IDW). Table 4. 1, shows briefly describes the 11 weather stations used in this study. The production data for Millet in tons ha−1 from 1998 to 2020 for the five districts was also obtained from the Ministry of Agriculture in North Darfur.

Table 4.1: Characteristics of first class weather stations in North Darfur State from which meteorological data used in this study was obtained for the period from 1981-2020.

ID	Name	Data type	Period	Latitude	Longitude	Elevation masl (m)
1	Al Fashir	Monthly	1981-2020	13° 38'	25° 20'	740
2	Kutum	Monthly	1981-2020	14° 21'	24° 40'	1160
3	Mellit	Monthly	1981-2020	14° 13'	25° 55'	900
4	Kabkabiya	Monthly	1981-2020	13° 39'	24° 5'	1120
5	EL Malha	Monthly	1981-2020	15° 09'	26° 15'	900
6	Umm Kadadda	Monthly	1981-2020	13° 59'	26° 14'	595
7	ELTawiesha	Monthly	1981-2020	12° 29'	26° 59'	591
8	AL Liait	Monthly	1981-2020	11° 57'	27° 04'	587
9	Saraf Omra	Monthly	1981-2020	13° 47'	23° 30'	1105
10	Kuma	Monthly	1981-2020	13° 39'	26° 01'	875
11	Dar EL Salam	Monthly	1981-2020	13° 05'	25° 53'	817

Source: the ministry of agriculture North Darfur State, Sudan

4.2.3 Methods

The study used the Mann-Kendall test and the Standardized Precipitation Index (SPI) and Reconnaissance Drought Index (RDI), to analyse drought patterns and trends over the past four decades in North Darfur State. The SPI and RDI can be computed using different monthly time scales, generally from 1 to 48 months (Eze *et al.*, 2022). The time series of ≤ 3 months is most appropriate for basic monitoring of drought, while ≤ 6 months can be used to monitor agricultural impacts, and ≥ 12 months is ideal for hydrological impacts (Raziei *et al.*, 2009; Svoboda *et al.*, 2016). Therefore, SPI-3 (June-August), SPI-6 (June-November), and SPI-9 (June- February)—the RDI used the same timescales—were used to assess drought events between 1981 and 2020. The DrinC—Drought Indices Calculator (Lab. of RW & WRM, NTUA, Athens, Greece) software was used to compute SPI, RDI, and potential evapotranspiration (PET)—the three have relatively small data requirements. The DrinC software can calculate drought indices across multiple time scales and generates output as an Excel spreadsheet (Tigkas *et al.*, 2016).

4.2.3.1 Standardized Precipitation Index (SPI)

The SPI, by McKee *et al*.(McKee *et al.*, 1993) is a widely accepted quantitative measure of drought. The index responds well to dry and/or wet weather conditions (Adhyani *et al.*, 2017). The SPI compares the rainfall amount recorded in a locality for a specific number of months with the long-term distribution of precipitation for the same number of months (Sirdaş *et al.*, 2003). The SPI does not account for the temperature component in detecting droughts because water balance and use are not accounted for (Eze *et al.*, 2022). The index is calculated monthly, with rainfall accumulation periods typically 1, 3, 6, 9, 12, 24, or 48 months. The corresponding SPIs are denoted as SPI-1, SPI-3, SPI-6, SPI-9, SPI-12, SPI-24, and SPI-48. However, it is better to use in a short time, like 3-6 months, to detect agricultural drought (Raziei *et al.*, 2009). In this study, the SPI was focused on SPI-3, SPI-6, and SPI-9, corresponding to the precipitation data in the past 3, 6, and 9 months, respectively, to investigate the Spatio-temporal variability of drought from 1981 to 2020. The multiple SPIs are very useful in differentiating between types of droughts and are thus crucial in quantifying the impacts of rainfall deficit on water-usable sources. The rainfall data was first applied to calculate SPI to obtain the estimated gamma parameters. Then, gamma fitting on the precipitation distribution was performed. The gamma probability density function is defined by Equation 4.1:

$$g(x) = \frac{1}{\beta^{\alpha}\Gamma(\alpha)} x^{\alpha-1} e^{-\frac{x}{\beta}} \quad (4.1)$$

Where x (> 0), β (> 0), and α (> 0) are the precipitation, scale parameter, and shape parameter, respectively.

The range of SPI values is from -3 (dry condition) to +3 (wet condition), and its severity consists of several classes (McKee *et al.*, 1993; Zhong *et al.*, 2019) (Table 3.2).

4.2.3.2 Reconnaissance Drought Index (RDI)

The Reconnaissance Drought Index (RDI) is recommended by the World Meteorological Organization (WMO) as an index for drought characteristics (Hayes *et al.*, 2011). It was also selected for this study because it is highly reliable and broadly accepted by researchers (Vangelis *et al.*, 2013). It is calculated based on rainfall and PET data, making RDI sensitive to climatic variability. The PET is calculated using the following equation (Hargreaves *et al.*, 1985).

$$PET = 0.00231 \times Ra \times (Tmean + 17.8) \times TR^{0.5} \quad (4.2)$$

Where *Ra* is the extra-terrestrial radiation, and *TR* is the daily temperatures difference between the daily maximum (*Tmax*) and daily minimum (*Tmin*) in °C (*Tmax–Tmin*).

The standardized RDI used in this study was calculated using Equation 4.3.

$$RDI_{(std)}^{(i)} = \frac{y_k^{(i)} - \bar{y}_K}{\sigma_{y_K}} \quad (4.3)$$

Where y_k,$\bar{y}_k$, and σ_{y_k} are the $ln(\alpha^{(i)}{}_k)$, arithmetic mean of y_k and standard deviation, respectively.

The values of α_k follow gamma as well as ln distributions—but the former is the most in diverse study locations and time series (Zarch *et al.*, 2017). Therefore, the gamma probability density function was applied to fit the frequency distribution of α_k (Tsakiris *et al.*, 2008). The RDI positive values indicate the wet period, while negative values indicate the dry period in comparison to the ordinary conditions of the locality (Table 4.2).

4.2.3.3 Drought Trend Analysis

The Mann-Kendall test (Kendall, 1975; Mann, 1945) and Sen's slope (Sen, 1968) were used for drought trend analysis. Mann Kendall is a non-parametric method widely used to detect trends in climate and hydro-meteorological variables such as precipitation, temperature, and stream flow. In addition, the Sen method is suitable for estimating the slope of a linear trend. Therefore, the Sen slope determines the magnitude of change of climatic variables in time series models (Lettenmaier *et al.*, 1994). The Mann-Kendall test is based on two hypotheses—null (H_0) expresses the existence of no trend, while alternative (H_1) expresses the existence of a linear trend. Using a significant level of 5%, if the P value ≤ 0.05, H_1 is not rejected, meaning the existence of a trend in the data, while if the *P* value ≥ 0.05, H_0 will be not rejected, which shows lack of a trend in the data. Positive values of *Q* indicate an increasing trend, while negative values indicate a decreasing trend. Values of *Z* greater than 1.96 are an indication of a significant increasing trend, whereas *Z* values less than -1.96 indicate a significant decreasing trend (Marini *et al.*, 2019a).

This study-evaluated drought trends using SPI-3, SPI-6, SPI-9, RDI-3, RDI-6, and RDI-9 for Umm Kadadda, Kabkabiya, Kutum, Mellit, and AL Fashir districts. If the time series showed a linear trend, then the Sen Slope was applied to determine its slope and the change rate of the SPIs and RDIs values.

4.2.3.4 Crop yield analysis

The most efficient way to assess how droughts affect agriculture is to evaluate agricultural productivity (Foster *et al.*, 2015; Madadgar *et al.*, 2017). Since rain-fed agriculture is majorly practiced in the study area, precipitation and PET significantly determine the rise or drop in crop production. Years of low-yield are indicated by negative deviations from normal

productivity—confirming the existence of drought (Dutta *et al.*, 2015). Therefore, the standardized variable of crop yield (SVCY) was used to assess the effects of drought on agricultural production. The yield per hectare data was used to compute SVCY for each of the regions within North Darfur in all districts (Equation 4.4)(Eze *et al.*, 2022):

$$SVCY = \frac{(Y_j - \bar{y})}{\sigma} \tag{4.4}$$

The SVCY was used to compute the crop yield loss ratio (YLR) of the each district (Equation 4.5):

$$YLR = \frac{(\bar{y} - Y_j)}{\bar{y}} \times 100\% \tag{4.5}$$

Where Y_j,$\bar{y}$, and σ are the crop yield in j year for the state, long-term average crop yield, and standard deviation of Y, respectively.

Table 4.2: Drought and yield classification based on SPI, RDI, and SVCY values.

SPI/RDI/ values	Drought class	SVCY values	Yield class
≥ 2.0	Extremely wet	1.0 ≥	No yield losses
1.5 to 1.99	Very wet	0 to - 0.49	Normal yield
1.0 to 1.49	Moderately wet	-0.5 to -0.99	Low yield losses
-0.99 to 0.99	Near normal	-1.0 to -1.49	Moderate yield losses
-1.00 to -1.49	Moderately dry	-1.5 to -1.99	Severe yield Losses
-1.50 to -1.99	Severely dry	≤ - 2.0	Extreme yield losses
≤ -2.0	Extremely dry		

4.2.3.5 Relationship between droughts and crop yield

To assess the impact of drought on agricultural production in North Darfur, the SVCY was correlated with SPI-3, SPI-6, SPI-9, RDI-3, RDI-6, and RDI-9 in Umm Kadadda, Kabkabiya, Kutum, Mellit, and AL Fashir districts. The main millet crop areas were Kutum, Kabkabiya, and portions of Al Fashir. The Pearson correlation coefficient (*r*) was implemented to analyse

the relationships. Interpretation of the strength of association among variables was guided by Table 4.3, according to the groupings of (Cohen *et al.*, 2013).

Table 4.3: Interpretation of correlation coefficients.

Positive relationship		**Negative relationship**	
Coefficients	Strength	Coefficients	Strength
0.10 to 0.29	Weak	-0.10 to -0.29	Weak
0.30 to 0.49	Moderate	-0.30 to -0.49	Moderate
0.50 to 1.00	Strong	-0.50 to -1.00	Strong

4.3 Results

4.3.1 Spatio-temporal distributions of droughts in North Darfur State from 1981 to 2020

The drought analysis shows drought status in negative SPI and RDI values and vice versa. The spatial distribution of drought using RDI-3 shows that 1983, 1990, 1992, 1999, and 2001 predominantly experienced moderate drought events—but 1983, 1990, and 1999 also had pockets of severe drought (Figure 4.2). The SPI-3 reported moderate drought in 1990, and a relatively small area in Umm Kadadda experienced severe drought.

Generally, during the study period, the RDI-3 and SPI-3 showed that only 11 and 9 drought events were reported, respectively. Both SPI-6 and RDI-6 reported 12 incidences of drought during the study period. The SPI-6 recorded eight events of predominantly moderate drought, i.e., 1989, 1990, 1992, 1999, 2000, 2001, 2002, and 2008—the RDI-6 reported only 7, i.e., 1989, 1990, 1992, 1999, 2001, 2002, and 2009. Still, both indices recorded severe drought in parts of Kabkabiya in 1989, Umm kaddada in 1990, and Kutum and Kabkabiya in 1999.

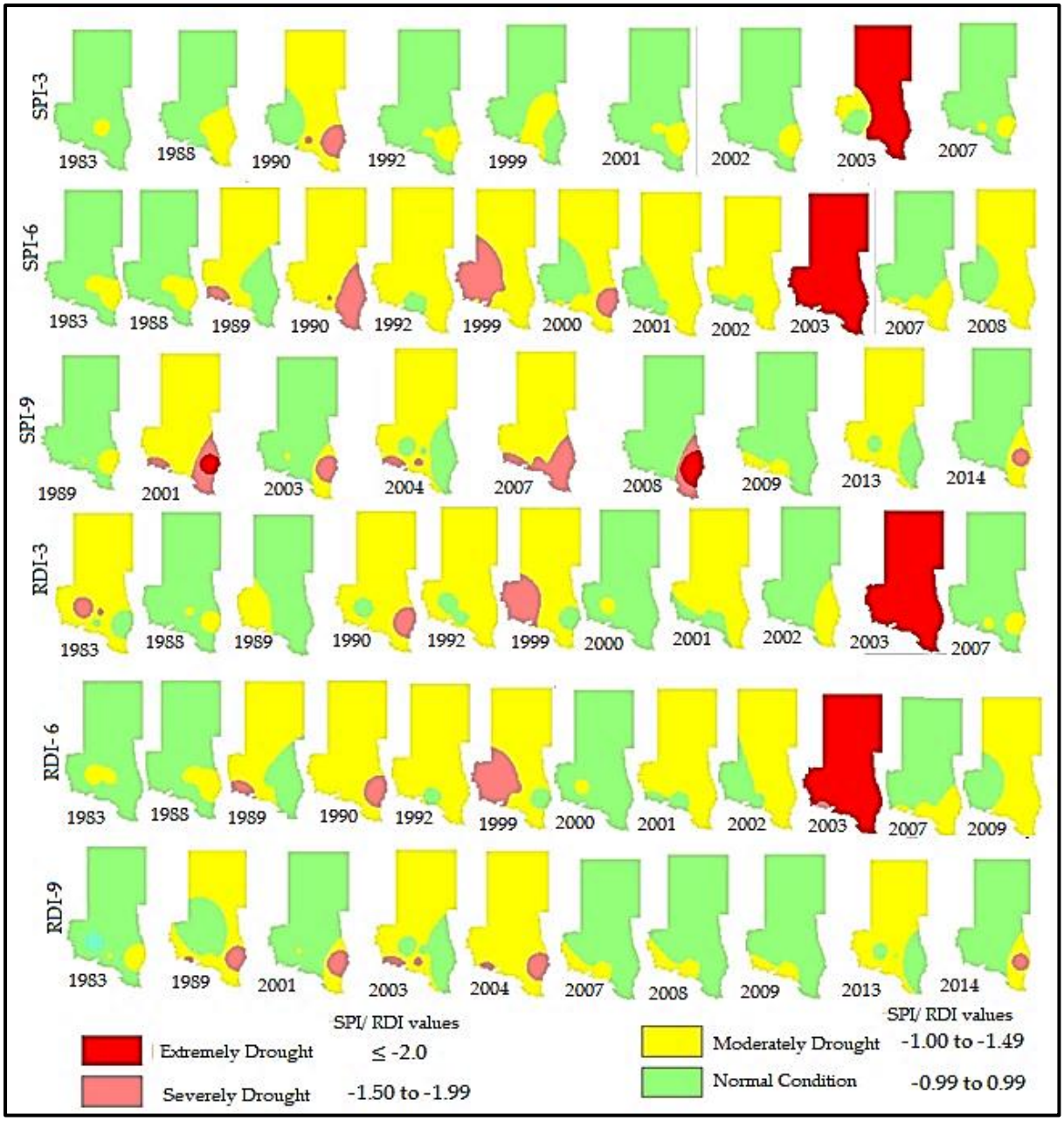


Figure 4.2. Spatial patterns of drought in North Darfur State from 1981 to 2020 based on Standardized Precipitation Index (SPI) and Reconnaissance Drought Index (RDI), in those years not visible on the map, North Darfur did not experience any form of drought.

The SPI-9 reported moderate droughts in 2001, 2004, 2007, and 2013, while the RDI-9's were in 1989, 2003, 2004, and 2013. Both indices and their respective months recorded events of extreme drought in 2003. Overall, the RDI index detected more years of drought than the SPI index. In 2003, the extreme drought experienced in North Darfur was more intense in Kutum and Mellit districts (Figure 4.3). Generally, more drought events were in Al Fashir, Kabkabiya, and Umm Kadadda, compared to Kutum and Mellit districts.

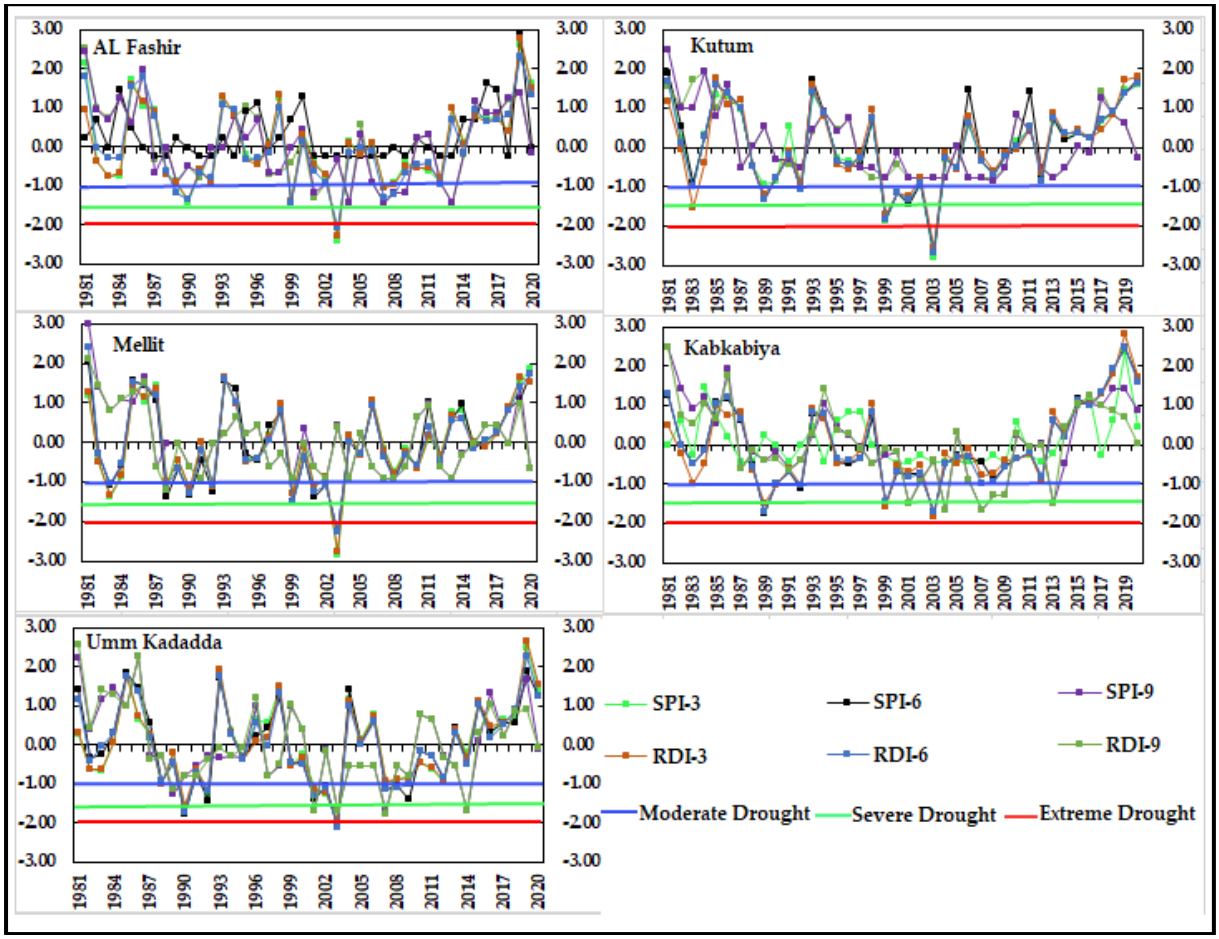


Figure 4.3. Standardized Precipitation and Reconnaissance Drought Indices values in North Darfur State at three timescales (3-months, 6-months and 9-months from 1981-2020).

4.3.2 Trend analysis of drought in North Darfur State

The Mann-Kendall test and Sen's slope estimator results are summarized in Table 4.4 and show drought trends were not significant at 5% in the five districts of North Darfur State. A positive trend indicates increased precipitation and vice versa. The SPI and RDI trend (Kendall Tau-b) ranges from 0.262 to -0.255 (Table 4.4). The Sen's slope ranges from 0.028 to -0.022. The correlation of SPI and RDI trend (Kendall Tau-b) for the 3-month timescale for the SPI and RDI showed a positive trend for all five districts. The same applied for the 6-month timescale for all districts except Kutum, which had a -0.233 for the SPI, symbolising rising drought intensity. The 9-month timescale for the SPI shows a positive trend for all districts, but the RDI shows a negative trend—therefore, the RDI is pointing out an increasing drought intensity in all five districts. Numbered lists can be added as follows:

Table 4.4: The statistical trend test results for different timescales of SPI and RDI over the period 1981-2020 of the five districts.

District	MK (Z)			*P*-Value[a]-months			Sen's Slope Estimate (Q)		
	SPI-3	**SPI-6**	**SPI-9**	**SPI-3**	**SPI-6**	**SPI-9**	**SPI-3**	**SPI-6**	**SPI-9**
Al Fashir	0.103	0.114	0.023	0.009	0.038	0.017	0.018	0.000	0.006
Kutum	0.146	-0.233	0.074	0.106	0.087	0.023	0.000	0.018	0.012
Mellit	0.152	0.168	0.082	0.118	0.101	0.022	0.021	0.017	0.012
Kabkabiya	0.262	0.006	0.131	0.151	0.139	0.028	0.000	0.019	0.022
Umm Kadadda	0.121	0.125	0.062	0.060	0.073	0.016	0.016	0.008	0.010
	RDI-3	**RDI-6**	**RDI-9**	**RDI-3**	**RDI-6**	**RDI-9**	**RDI-3**	**RDI-6**	**RDI-9**
Al Fashir	0.103	0.049	-0.130	0.357	0.666	0.244	0.017	0.008	-0.021
Kutum	0.146	0.100	-0.255	0.188	0.370	0.024	0.023	0.017	-0.022
Mellit	0.172	0.113	-0.243	0.121	0.311	0.030	0.022	0.016	-0.022
Kabkabiya	0.262	0.154	-0.135	0.018	0.166	0.226	0.028	0.020	-0.019
Umm Kadadda	0.121	0.049	-0.136	0.279	0.666	0.221	0.016	0.007	-0.012

4.3.3 Impact of drought on millet production

The spatial and severity variability of droughts also led to variability in a drop in millet crop yield in the five districts of North Darfur. Based on the threshold values listed in Table.3.2, extreme crop losses, SVCY ≤ - 2.0, were not recorded in any district during the study period, while severe crop losses, -1.5 <SVCY> -1.99, were recorded in Al Fashir, Kabkabiya, and Umm Kadadda districts in 2003. Furthermore, moderate crop losses, -1.0 <SVCY>-1.49, were recorded in Kabkabiya and Umm Kadadda in 2000, 2001, 2003, 2004, 2005, 2007, 2009 and 2015. All districts recorded low crop losses, -0.5 <SVCY> -0.99, as shown in Figure 4.4. By comparing SPI and RDI for the respective timescales for the five districts in North Darfur, overall, their values have positive relationship with crop yield, i.e., an increase in the indices resulted to a rise in crop yield and vice versa.

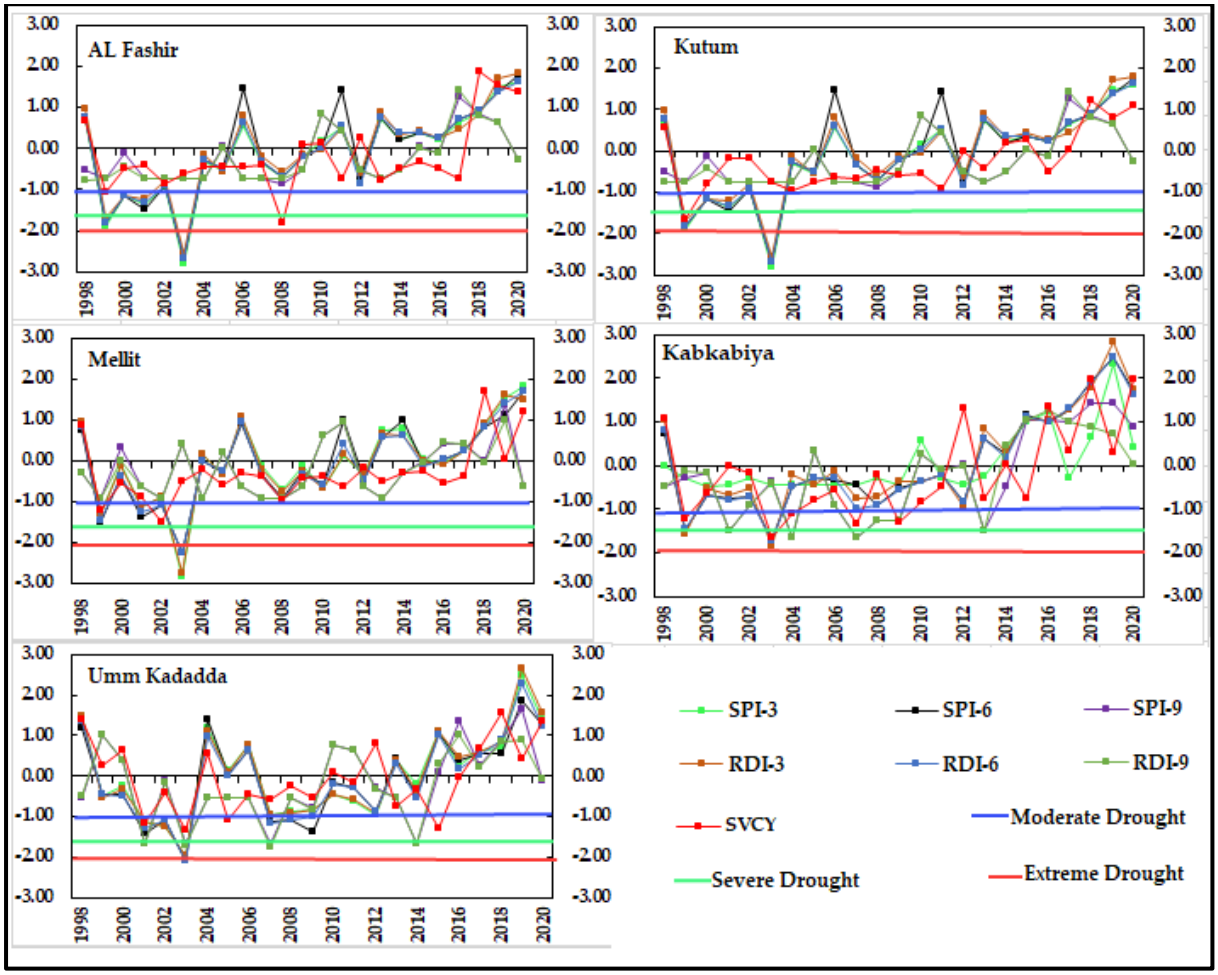


Figure 4.4. Drought and crop yield analysis of Um kadada, Kabkabiya, Kutum, Mellit, and Al Fasher districts, the North Darfur from 1998-2020.

The statistical relationship between SVCY and drought trend using the SPI and RDI using the Pearson correlation coefficient (r) is shown in Table 4.5. The results depict a moderate to strong relationship between drought and SVCY for the indices for all timescales used in the study for all districts, except Mellit (SPI- and RDI-9) which showed a weak relationship. In general, the results show that droughts impacted millet yield in North Darfur State.

Table 4.5: Statistical relationship between SVCY and drought trend using SPI and RDI, using Pearson correlation coefficient

SVCY/Indices	SPI-3	SPI-6	SPI-9	RDI-3	RDI-6	RDI-9
Al Fashir	0.57	0.50	0.43	0.58	0.55	0.38
Kutum	0.65	0.55	0.38	0.66	0.65	0.36
Mellit	0.63	0.64	0.14	0.63	0.68	0.15
Kabkabiya	0.40	0.63	0.55	0.62	0.65	0.47
Umm Kadadda	0.49	0.51	0.50	0.48	0.51	0.48

4.4 Discussion

This study was performed a spatio-temporal analysis of drought and how drought had affected millet yield in North Darfur using the Standardized Precipitation Index (SPI) and the Reconnaissance Drought Index (RDI). The nonparametric Mann-Kendall test and Sen's slope approach were utilized to investigate the long-term trend of droughts in the study area. The Pearson correlation (*r*) was used in the analysis of the relationship between drought and millet crop yield.

Rainfall and minimum and maximum temperatures covering about 40 years were used to calculate the drought indices, i.e., SPI and RDI, used to detect drought in the study area. The indices were calculated at varying timescales (3, 6, and 9 months) between 1981 and 2020. Only drought events were examined even though the SPI and RDI time series included both drought and non-drought statuses. The main periods of drought, according to the SPI, were 1989, 1990, 1992, 1999, 2000, 2001, 2002, 2004, 2003, 2007, 2008, and 2013. The RDI reported droughts in 1983, 1989, 1990, 1992, 1999, 2000, 2001, 2002, 2004, 2003, 2009, and 2013 (Figure 4.2). The results of the drought analysis in this study agree with previous studies such as Elhag and Zhang. (Elhag and Zhang, 2018) and Mohamed *et al*.(Mohmmed *et al.*, 2018). The analysis depicted normal conditions and drought status using the positive and negative SPI and RDI values—positive values indicated wetness, while negative values were related to dryness (Figure 4.3). This analysis shows that drought is a frequent phenomenon in the study area. Even though the SPI and RDI values showed that drought intensity and frequency faded in some years, they recurred within a few years. Differences were evident between the SPI and RDI for the respective timescales. The spatial analysis shows the variability of drought patterns across the state over the years. Parts of Umm Kadadda and Kabkabiya districts were the most affected by drought—even during years when other parts of North Darfur were under normal conditions, some places in Umm Kadadda and Kabkabiya were experiencing drought, e.g., RDI-3 (1989), SPI-3 (1992), and SPI-6 (2007). When other places experienced moderate drought, parts of Umm Kadadda and Kabkabiya would still experience severe drought, e.g., RDI-3 (1999) and SPI-6 (1999). Drought trend in short-term, i.e., based on 3- months for SPI and RDI, showed that North Darfur State was affected by extreme, severe, and moderate drought conditions. Short-term drought events are linked to El Nino/Southern Oscillation (ENSO) (Elhag and Zhang, 2018). This study found that the RDI index is more sensitive to variabilities than the SPI index for detecting drought trends. For

example, the SPI index results showed that 1999 and 2003 were normal conditions in Kabkabiya and AL Fashir districts. Still, compared with the RDI values, the results showed that Kabkabiya and Al Fashir were severe to extreme droughts. This sensitivity is due to an effect of the temperature element in PET used to calculate the RDI (Peña-Gallardo *et al.*, 2019). This consideration is consistent with several studies worldwide reported that PET is considered the main factor for agricultural studies (Abdelmalek and Nouiri, 2020; Abubakar *et al.*, 2020; Adnan *et al.*, 2017).

Droughts have persisted in North Darfur and threaten agricultural productivity (Mohmmed *et al.*, 2018). Results of the impact of drought on millet crop yield showed that droughts led to decreased production in North Darfur State. Severe crop losses occurred in Umm Kadadda, AL Fashir, and Kabkabiya in 2003. Moderate losses in crop yield were in Umm Kadadda and Kabkabiya in 2000, 2001, 2003, 2004, 2005, 2007, 2009, and 2015. The five districts of North Darfur recorded low crop losses during the study period as shown in Figure 4.4. These results agree with a study conducted in Sudan by Elhag and Zhang. (Elhag and Zhang, 2018). According to Liu *et al*. (Liu *et al.*, 2018), short- to medium-term droughts could impact Millet yield in North Darfur State. Overall, the correlation analysis between the standardized variable of crop yield (SVCY) and drought depicts a moderate to strong relationship between them for the SPI and RDI for all timescales. The SPI and RDI values showed positive relationships with crop yield—a decrease in the indices' values resulted in a fall in crop yield, while an increase in the SPI and RDI values meant a rise in crop yield (Figure 4.4). Therefore, this highlights the role drought plays in controlling the vulnerability of agricultural communities in the study area—it makes North Darfur State susceptible to droughts and climate change.

The North Darfur State experiences extreme temperatures, fluctuating rainfall, and drought. The unreliable rain combined with the drought makes North Darfur highly vulnerable to the slightest decrease in rainfall or a temperature rise (Cheeseman, 2016). The temperature increases have resulted in a decline in precipitation. Indeed, under its current climate, North Darfur is faced with recurrent food insecurity and water scarcity, decreasing soil fertility, and absence of physical security, triggered and/or exacerbated by climate variability, which alters agricultural productivity (Twongyirwe *et al.*, 2019). Therefore, drought, the main determining factor in crop yield—the low soil moisture content and high PET losses reduced crop

productivity. Low precipitation has contributed to the increased drought in the study area severely affecting rainfed agriculture mainly practiced in North Darfur (Mohmmed *et al.*, 2018). If no significant adaptations are made, climate change will put the livelihoods of those living in most of the study area at increased risk from drought. Thus, farmers should use techniques that minimize soil moisture loss and be informed about probable planting dates in each new season. Farmers should also implement appropriate measures if the weather forecasting systems indicate an unreliable rainfall year. North Darfur is very vulnerable to drought impacts due to its high exposure and sensitivity (Mohmmed *et al.*, 2018). Natural meteorological conditions, as well as the low level of socioeconomic development in the study area, have contributed to the vulnerability (Noureldeen *et al.*, 2020). Aggravating droughts and related hazards will increase across North Darfur (Arias *et al.*, 2021; Gizaw *et al.*, 2017). The drought trend analysis showed that the RDI indicated an increasing drought intensity over the last 40 years in all five districts of North Darfur. As much as adaptations to climate change are implemented in a timely and effective way, controlling population growth could be better in mitigating drought risk because it improves socioeconomic vulnerability, which can reduce potential exposure to drought (Mohmmed *et al.*, 2018).

4.5 Conclusions

Climate change has led to more intense local and regional droughts and related impacts—North Darfur is no exception. Quantifying and understanding drought occurrence and its consequences on agricultural production and ecosystems is particularly important. This study carried out a spatio-temporal analysis of drought and the effect of drought on rainfed millet crop production in North Darfur State in Sudan, using the Standardized Precipitation Index (SPI) and the Reconnaissance Drought Index (RDI), and the standardised variable of crop yield (SVCY). Climate change has significantly threatened human well-being and food security in North Darfur. Generally, the results of this study will provide a better understanding of the spatio-temporal evolution of drought in North Darfur State to decision-makers to help mitigate the devastating impacts of droughts. Therefore, local and international future development programs concentrating on adaptation and mitigation of climate change effects could be based on these results, targeting the most vulnerable agricultural areas. This study suggests improving the drought severity mapping by comprehensively comparing different spatial estimation approaches to develop an efficient drought-monitoring system.

CHAPTER FIVE

Mapping and monitoring spatio-temporal patterns of rainfed agriculture lands of North Darfur State, Sudan, using earth observation data

This Chapter based on:

Altoom, M.B., Adam, E., & Ali, K.A. (2023). Mapping and monitoring spatio-temporal patterns of rainfed agriculture lands of North Darfur State, Sudan, using earth observation data. *Land, 12*, 307: https://doi.org/10.3390/land12020307

Abstract

Rainfed agriculture in northern Darfur is influenced by erratic seasonal and decadal rainfall patterns and frequent droughts. Understanding the spatio-temporal variation in rainfed agriculture is crucial for promoting food security, socio-economic stability and protecting vulnerable ecosystems. This study aimed to investigate the spatio-temporal dynamics of rainfed agriculture in North Darfur State from 1984 to 2019 using multitemporal Landsat observation data. Using the random forest (RF) technique, multitemporal images were classified into common land use/ land cover (LULC) classes and rainfed agriculture on goz (sandy) and wadi (seasonal river) lands. Overall accuracies (OA) were assessed using confusion matrices. Results revealed that OAs were in the range of 94.7-96.9%, while the kappa statistics (κ) were greater than 0.90. The results showed that goz land used for rainfed agriculture increased by 889,622.46 ha over the 1994-1999 period, while it decreased by 658,568.61 ha between 2004 and 2009 south of the 232.9 mm isohyet. Rainfed cultivation of wadi lands expanded significantly by 580,515.03 ha over the 2014-2019 period and decreased by 182,701.8 ha over the 1994-1999 period, especially in the 362.8-477.2 mm isohyets—which is beyond the climate-adapted 500 mm isohyet agronomic dry limit. These spatial trends need further investigation as they may exacerbate both regional land degradation and disputes among farmers over scarce wadi lands. This study provides essential spatial data which are lacking owing to ongoing conflicts—this can help decision-makers formulate sustainable land use monitoring systems.

Keywords: Remote sensing, Sudan, Change detection, Random forest classifier, Land cover.

5.1 Introduction

Rainfed agriculture plays an essential role in food security in most regions worldwide (Elagib *et al.*, 2019). Around 75–82% of the total cropland areas in the world are under rainfed agriculture (Bradford *et al.*, 2017; Elagib *et al.*, 2019; Laux *et al.*, 2010). This crucial sector of agriculture usually depends on the physical environment and, most importantly, the variability and distribution of rainfall. Therefore, rainfed farming is vulnerable to climate-related hazards, and the crop yield is unreliable and difficult to predict (Rockström *et al.*, 2010; Sohoulande *et al.*, 2019). Sudan in north-eastern Africa is among the sub-Saharan African countries that depend on rainfed agriculture. More than 90% of cultivated land comprises rainfed farming, accounting for one-third of the GDP (Siddig *et al.*, 2018; Siddig *et al.*, 2020a). The rainfed agriculture subsector essentially encompasses private mechanised farming distributed to the east and west of the Nile River banks and its tributaries. Unfortunately, these parts are characterised by environmental and socio-economic hazards such as frequent droughts, unpredictable low, poorly distributed, and highly variable monthly/ seasonal rainfall, population pressure; social change; deforestation; soil erosion; salinisation, and water depletion.

For example, Darfur, a semi-arid region in western Sudan, witnessed three droughts between 1950 and 1990. The drought was mild in the mid-1960s but relatively severe between 1972 and 1975. The region experienced a catastrophic drought between 1982 and 1984 when average rainfall was reduced by 50% or more in many areas (Fuller, 1987a; Ibrahim, 1984). Hence, Darfur has been described as a hotspot of land and environmental degradation, experiencing among the most prominent natural threats in the region. Despite the high rainfall variability and persistent drought, rainfed agriculture and livestock are the primary sources of livelihood for 80–90% of the population of the Darfur region (Osman *et al.*, 2013; Siddig *et al.*, 2020a). This crucial agriculture sector usually depends on the physical environment and, most importantly, the amount and distribution of rainfall. Therefore, rainfed agriculture is vulnerable to climate-related hazards, including variability, and the crop yield is thus unreliable and difficult to predict. Persistent drought and associated impacts on rainfed agricultural practices contribute to regional social and/or political instability (Abdelaziz *et al.*, 2010; Ali *et al.*, 2016; Brauch, 2006; Osman, 2012; Osman, 2007).

Rainfed agriculture in North Darfur State lies between the 250 mm and 600 mm isohyets. The region is characterised by rainfall variability in both time and space, high maximum temperatures, significant temperature differences between day and night, strong winds, and low humidity. This complex climate condition is reflected in an increased vapour pressure deficit with implications for water use efficiency, transpiration, and evaporation. Therefore, the rainfed agriculture system is largely a function of climate and cultural practices, with more emphasis on climatic variables.

There are two farming systems in North Darfur State. The first and most widespread is rainfed cultivation by smallholder farmers—mostly of bulrush millet and secondary cash crops include groundnuts and sesame on goz (sandy) soils. This type of farming system starts with removing the sparse trees and grassland covering the land to be cultivated, then seeds are planted traditionally by hand, using a hoe or digging stick, shortly after the first rains. Farmers weed the fields assiduously until the harvesting season between September and December to maintain the soil moisture and allow the crops to flourish. Owing to population increase, sandy soils are repeatedly farmed without fallow periods, and cultivation has expanded into less fertile and ecologically vulnerable areas. This ultimately destroys the region's vulnerable ecological system and vegetation cover in the region. Furthermore, due to the high spatial and temporal rainfall variability, farmers prepare their fields and plant in advance in different areas near their homesteads and hope for rain (Ibrahim, 1978; Ibrahim, 1984). The vegetation removal from goz soils has intensified soil erosion and further deteriorated soil fertility, resulting in low land productivity and crop yields. Therefore, farmers have been forced to cultivate larger areas and extend into the rangeland and ecologically vulnerable areas. This has resulted in environmental degradation and has fomented local tensions between pastoralist groups and the farming communities (Mohammed *et al.*, 2013; Mohmmed *et al.*, 2018; Siddig *et al.*, 2020a).

The second farming system is practiced in the clay soils found along alluvial and seasonal valleys, known as wadis, originating from the Jebel Marra volcanic massif and the surrounding Precambrian Basement Complex hills. This farming system combines rainfed, flood retreat and small-scale irrigation, using either hand or diesel-powered pumps. The wadi soils are relatively rich in alluvial loam and are more productive than farming on the goz—they are therefore used for growing tobacco and vegetables (Osman and Cohen, 2014; Young *et al.*,

2005). Understanding the spatio-temporal dynamic of rainfed agriculture and the determining climatic factors in the study area can play a key role in promoting food security and socio-political stability, as well as in protecting and restoring ecosystem services (De Marinis *et al.*, 2021; Elagib *et al.*, 2021; Thyagharajan *et al.*, 2019).

The lack of availability of spatial data for monitoring trends in rainfed agriculture is not only a threat to food security but also an impediment to understanding the study area's environment, climatic hazards, and socio-economic dynamics. Owing to political instability in some parts of the study area, traditional approaches to agricultural monitoring, such as expert scouting estimates, crop cut information, field assessment, and surveys, pose extreme danger to field teams, in addition to significant financial costs (Nakalembe *et al.*, 2021; Sahajpal *et al.*, 2020). Nowadays, most of these events can be predicted, and data and tools can provide early warning and impact assessment; this underscores the importance of timely and accurate production forecasts and near-real-time agricultural monitoring (Nakalembe *et al.*, 2021; Sahajpal *et al.*, 2020). Satellite remote sensing (RS) offers useful analysis tools in several technical-scientific fields and has been used widely worldwide for monitoring the changes that occur in the environment and the identification of their magnitude at different space-temporal resolutions (Carella *et al.*, 2022; Orusa *et al.*, 2021; Orusa *et al.*, 2020). In addition, satellite remote sensing is crucial in monitoring rainfed agriculture since its data has continuous spatial coverage, is freely accessible, and can be acquired at high temporal resolutions. This is particularly relevant in areas where ground data are insufficient, lacking, or unsafe to obtain (Melaas *et al.*, 2013; Rembold *et al.*, 2019; Schaefer *et al.*, 2019; Yang *et al.*, 2012). Therefore, various types of remotely sensed data have been used to map and monitor rainfed agriculture, such as Moderate-resolution Imaging Spectro-radiometer (MODIS), used to map rainfed wheat (Sabzchi-Dehkharghani *et al.*, 2021), SPOT-VEGETATION, with high spatial resolution, Sentinel 1 and 2, and Landsat (Colombo *et al.*, 2011; Nakalembe *et al.*, 2021; Rembold *et al.*, 2019). Since 1972, Landsat has been freely available (Schaefer and Thinh, 2019). Launching medium-resolution Landsat sensors has offered unprecedented opportunities to study the change in agricultural lands at higher spatial resolution.

This study aimed to map and monitor the spatio-temporal patterns of rainfed agriculture in North Darfur State from 1984 to 2019 using RF supervised classifier and multitemporal Landsat data. The specific objectives were: (a) to quantify the transformation of rainfed agricultural land for significant land cover classes using change detection, and (b) to identify

and detect spatio-temporal trends in changes in LULC, particularly for rainfed agriculture lands in North Darfur State. The outcomes of this study are essential for decision-makers to adopt suitable strategies for sustainable agricultural land use management and planning.

5.2 Materials and Methods

5.2.1 Study Area

The North Darfur State is located in North-western Sudan, covering an area of about 30 million hectares (ha)—the state occupies more than half of the Darfur region. North Darfur State consists of twelve districts, i.e., El Malha, Mellit, and Kutum in the north, Kuma and Umm Kaddada in the east, Dar El Salam, El Tawiesha, and Al Liait in the south. Kabkabiya, Saraf Omra, and EL Siseaf are in the west, while Al Fashir, the state's capital city, is placed centrally (Figure 5.1) (Mohmmed *et al.*, 2018).

North Darfur extends between at latitude 11° 45′ 49″-20° 00′ 30″ N and longitude 22° 46′ 47″-27° 29′ 47″ E and supports typical Sahelian vegetation. The highest point is Marrah mountain (3,042 m above sea level) (Ibrahim, 1984). Hot, arid and semi-arid climatic conditions characterise the area. The rainfall pattern is mono-modal, falling in the summer (i.e., from May to October) with an average annual rainfall ranging from 152 mm per annum in the north to 530 mm per annum in the south. About 85% of the rainfall occurs in July and August. The average maximum and minimum temperatures are 42 ° C and 11 ° C, respectively (Mohmmed *et al.*, 2018). Rainfed agriculture is the main economic activity for 85% of the population in the area. Millet and groundnuts are grown mainly in goz lands, while tomato, onion, and okra are grown in wadi lands. These crops are significant sources of food security, and their productivity depends on soil fertility and rainfall occurrence (Fadul, 2004).

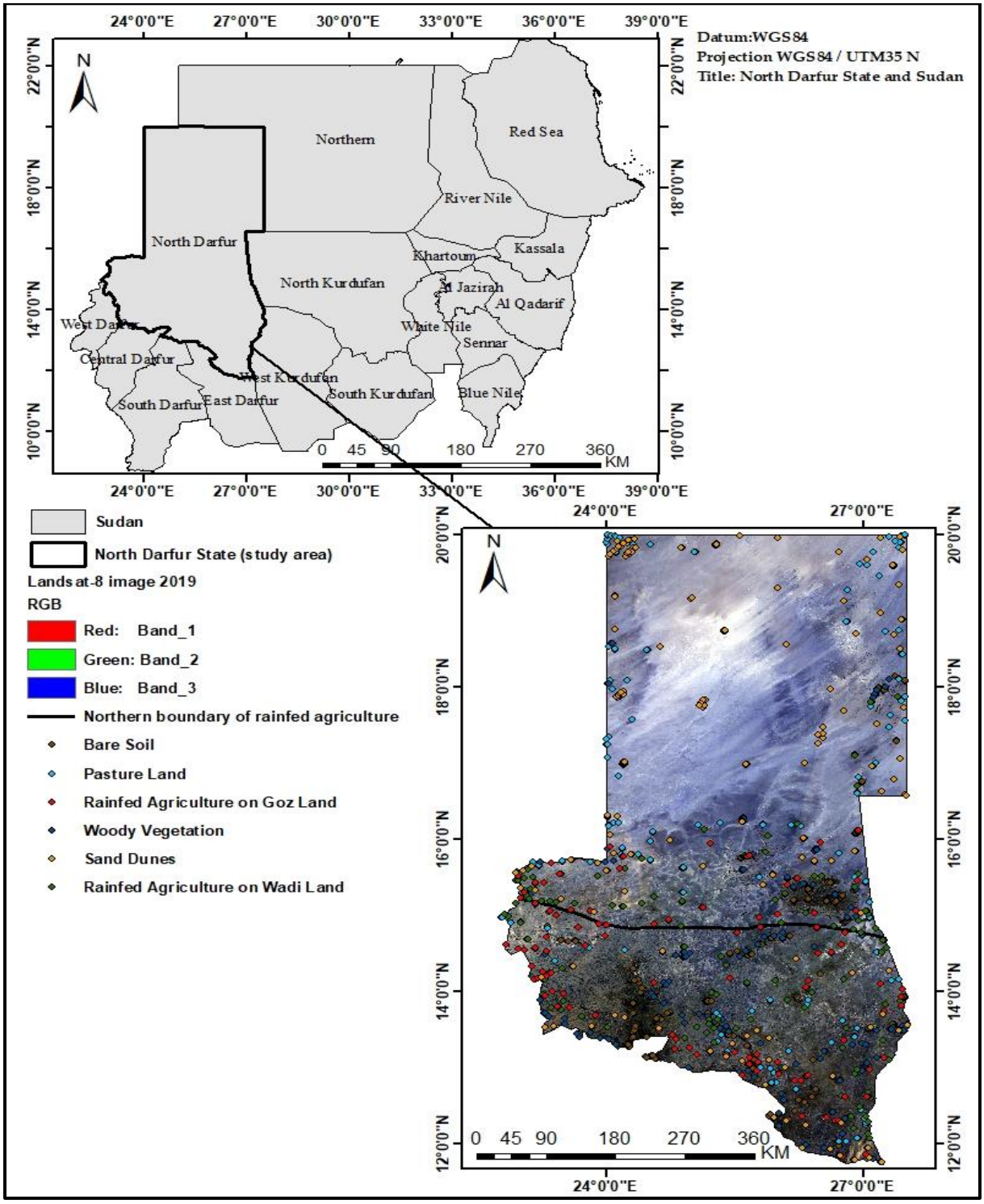


Figure 5.1. Location of the study area with spatial distribution of the samples in Landsat-8 image 2019. The northern boundary for rainfed agriculture was identified in 1984 using field observation.

According to the recent National Census of Sudan conducted in 2008, the population of North Darfur is approximately 1.7 million compared with 1.1 million in the 1984 census. The population density was estimated to be 9.1 persons per km^2 (Ali Ahmed, 2008).

5.2.2 Remote Sensing Data Acquisition and Pre-Processing

The image acquisition date was selected based on the availability of satellite imagery and the rainfed agriculture growing season. In all, 176 scenes were used corresponding to four main sensors, i.e., Landsat Multispectral Scanner (MSS) at 60 m resolution acquired in 1984; Landsat Thematic Mapper (TM) at 30 m resolution acquired in 1989, 1994, and 1999; Landsat Enhanced Thematic Mapper Plus (ETM^+) at 30 m resolution acquired in 2004 and 2009; and Landsat Operational Landsat Imageries (OLI) at 30 m resolution acquired in 2014 and 2019. All images for October and November, under cloud-free conditions, were obtained from the United States Geology Survey Earth Explorer Website (https://earthexporer.usgs.gov/) (ID data see in supplementary material).

In this study, all images were radiometrically and geometrically corrected using the FLAASH module in ENVI® software, Version 5.1. FLAASH tool 5.1 was developed by ENVI 5.1 Tool. FLAASH atmospheric correction is used to solve atmospheric disturbance problems. To standardise the spatial resolution of the Landsat data, Landsat Multispectral Scanner (MSS) images for 1984 were resampled to 30 m spatial resolution using the nearest neighbour method (Lossou *et al.*, 2019). In addition, the 22 scenes of each year were mosaicked into a new raster image, and then the area of interest was subset based on rainfed agriculture that took place in the study area. Finally, all Landsat imageries used in this study were projected into the Universal Transverse Projection system zone 35N and datum of World Geodetic System 84 (WGS84) using ArcMap10.5 software and ERDAS Imagine 2020 software.

5.2.2 Reference Data

The reference data were derived from satellite images and Google Earth—the latter is very helpful in providing ground truth data when fieldwork cannot be done, and the features on satellite images are unclear (Levi, 2010). The six most common land use and land cover classes (LULC) were identified in the study area. These are bare soil, pastureland, and rainfed agriculture on goz land, sand dunes, woody vegetation and rainfed agriculture on wadi land—the typical image of each land use class is shown in Table 5.1. The reference data were digitised

for each LULC class on the multitemporal images. The number of training points varies based on class size and visibility. We used Google Earth to verify the classes visually. The reference data were then divided into 30% for the testing data set and 70% for the training data set.

Table 5.1: Description of the land use and land cover (LULC) classes in the study area.

No.	Class name	Typical image of land use class	Description
1	Bare soil		Wasteland and fallow lands with rocks and gravel. Bare soil is situated in mountainous terrain in the west and some north part of the study area.
2	Pastureland		Vast areas are covered with grassland and shrub used for grazing livestock.
3	Rainfed agriculture on goz land		Goz areas comprise undulating sandy accumulations of old and stabilised dune belts used for farming millet, sorghum and groundnut.
4	Sand dunes		Areas covered with large masses of shifting sand and un-vegetated old dunes with low levels of organic matter and nitrogen. They occupy most parts of the study area.
5	Woody vegetation		Areas covered with woody vegetation, mostly Acacia tree species.
6	Rainfed agriculture on wadi land		Wadi areas are generally wetter areas for growing vegetables (on clay soils) and tobacco (on alluvial soils).

Typical images of rainfed agriculture and common LULC were taken during the field survey to study area in August 2020

5.2.3 Classification of Images

This study used a random forest (RF) machine learning algorithm developed on ERDAS Imagine 2020 software to classify the six LULC classes on the multitemporal Landsat images. RF employs a bagging (bootstrap aggregation) operation where several trees (*ntree*) are constructed based on a random subset of samples derived from the training data. Each tree is independently grown to maximum size based on a bootstrap sample from the training dataset without pruning. Each node is split using the best among a subset of input variables (*mtry*) (Breiman, 2001). The multiple classification trees then vote by plurality on the correct classification. In addition, at each node, variables are randomly selected from all predictor variables, and one of them is chosen as the splitting criteria. When the bootstrap sample set is drawn by sampling with a replacement for each tree in the forest building process, about one-third of the original instances are left out (Tsoumakas *et al.*, 2009). This set of instances is called OOB (out-of-bag) data (Breiman, 2001). Each tree has its own OOB data set, which is used for error estimation of individual trees in the forest, and by averaging the OOB error rates from all trees, the random forest algorithm gives an error rate called the OOB classification error for each input variable. The RF was selected for this study owing to its reliability. It requires limited parameters to be optimised and obtains classification results rapidly (Puissant *et al.*, 2014). A critical feature of the RF approach is the ability to rank predictors according to an internal measure of variable importance (Verikas *et al.*, 2011).

The two parameters, i.e., *ntree and mtry,* were optimised to improve the accuracy of the LULC classification using a grid search and a 10-fold cross-validation method. The default number of trees (*ntree*) is 500, while the default number of variables (*mtry*) is the square root of the total number of spectral bands used in the study, i.e., $\sqrt{P}$ (Colombo *et al.*, 2011). The grid search values for the *ntree* were set to vary between 500 and 10,000, with an interval of 1,000, while the grid search value for the *mtry* parameter was 2.

5.2.4 Change Detection

In remote sensing, change detection is the process of identifying changes/differences in geographical surface phenomena by comparing scenes of the same location acquired at different times (Singh, 1989). A variety of change detection algorithms have been developed

in the last few years, such as matrix comparison, principal component analysis, post-classification comparison, and image differencing (Kumar *et al.*, 2020). In this study, the image differencing change detection method was used to map LULC change in hectares in North Darfur State for the years 1984-1989, 1994-1999, 2004-2009 and 2014-2019. Transition statistics were generated by the image differencing method. For more information on transition statistics see (Islam *et al.*, 2018; Kumar and Jain, 2020).

5.2.5 Accuracy Assessment

An error matrix is the most common technique to represent the classification accuracy of data. In this study, 70% of the dataset was used to train the classification model, and 30% was used to develop the confusion matrix for the accuracy assessment. The confusion matrix was used to calculate the overall accuracies (OAs), user's and producer's accuracies (UAs and PAs, respectively), and kappa coefficient (κ). The κ was computed as follows in Equation 5.1:

$$\frac{N\ \sum_{i=1}^{r} Xii\ -\ \sum_{i=1}^{r}(\times i +\ *X+i)}{N2-\ \sum_{i=1}^{r}(Xi+*X+i)} \qquad (5.1)$$

Where *N* is the total number of observed pixels, *r* is the number of rows; *Xi* is the number of observations in row *I* and column *i*, *Xi+* and *X+i* are the marginal totals of row and column (Congalton, 1991; Lossou *et al.*, 2019).

5.3 Results

5.3.1 Spatial Distribution of Rainfed Agriculture and Other Land Cover Classes

The rainfed agriculture and common land cover classification maps were obtained using multi-temporal analysis of Landsat imageries using RF classification. Figure 5.2 and Table 5.2 show the spatial distribution of rainfed agriculture and other LULC classes for 1984, 1989, 1994 and 1999. The 1984 classified map shows that the most dominant class, sand dunes, covered 48.8% (15,491,287.71 ha) of the study area, followed by pastureland at 19.19% (6,087,037.68 ha), and rainfed agriculture on goz land 12.6% (3,997,107.09 ha), whereas woody vegetation took up 10.2% (3,255,871.68 ha). Rainfed agriculture on wadi land covered only 6.5% (2,063,802.42 ha), while 2.6% (829,963.35 ha) of the area was covered by bare soil. The 1989 LULC map shows that about 47.2% (15,001,726.86 ha) of the area for that year was covered

by sand dunes, followed by pastureland at 16.75% (5,316,714.45 ha), with rainfed agriculture on goz land at 12.99% (4,120,391.79 ha) and mostly in the vicinity of villages. The analysis also indicated that 9.95% (3,155,611.14 ha) of the study area was covered by woody vegetation. An area of 3,038,405.4 ha (9.58%) of North Darfur State was occupied by rainfed agriculture on wadi land, and bare soil covered 3.44% (1,092,219.57 ha) of the area.

The 1994 LULC map of North Darfur State shows that 55.43% (17,586,085.59 ha) of the area was under sand dunes, 13.33% (4230, 389.88 ha) was under pastureland, and 12.35% (3,919,095.54 ha) of the area was covered by rainfed agriculture on goz land. However, the area of woody vegetation accounted for 8.86% (2,809,914.39 ha). Rainfed agriculture on wadi land occupied 8.14% (2,582,809.29 ha), and the proportion with bare soil was 1.88% (596,770.74 ha). The results for the 1999 classified map indicate that the dominant class of land cover was sand dunes covering 58.49% (18,438,988.41 ha), followed by rainfed agriculture in goz land estimated at 15.25% (48, 087, 18.01 ha), and pastureland estimated at 10.04% (3,165,771.51 ha). Rainfed agriculture on wadi land covered 7.61% (2,400,107.49 ha), and woody vegetation covered 6.83% (2,155,598.64), while the bare soil accounted for 1.76% (554,768.19 ha). Figure 5.3 and Table 5.2 show the spatial distribution of rainfed agriculture and other LULC classes in 2004, 2009, 2014 and 2019.

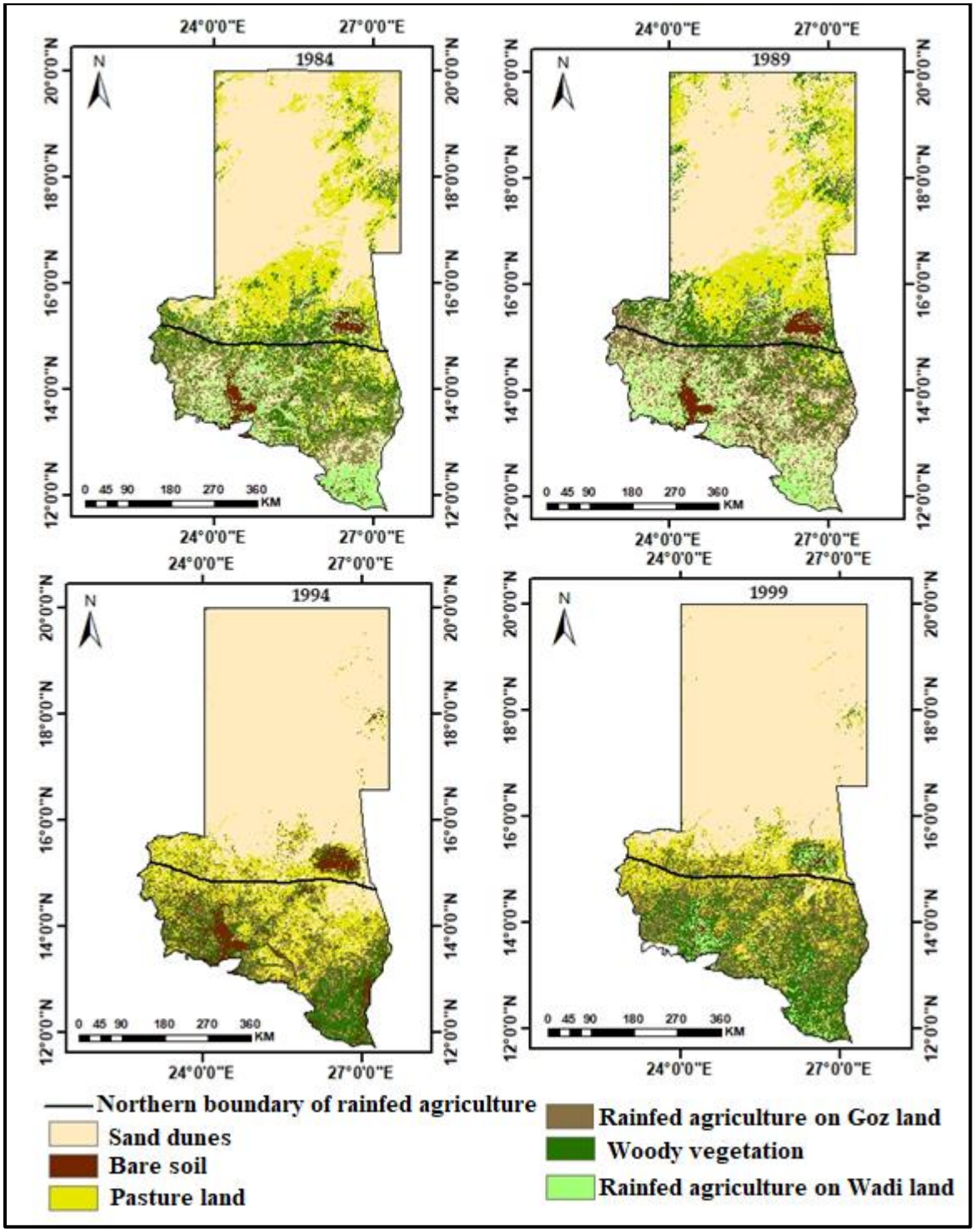


Figure 5.2. Spatial distribution of the rainfed agriculture and other LULC classes in 1984, 1989, 1994 and 1999. The classification was obtained using Landsat-5 MSS, Landsat-5TM, and random forest classifier.

The 2004 classified map shows that the sand dunes covered 49.10% (15,579,090.63 ha) of the study area, followed by pastureland at 17.56% (5,572,342.98 ha). Rainfed agriculture on goz land covered 12.88% (4,085,995.14 ha), woody vegetation was 8.15% (2,586,354.75 ha), and

coverage by rainfed agriculture on wadi land was 8.99% (2,852,367.39 ha), with bare soil taking up 3.3% (1,048,919.04 ha) of the area.

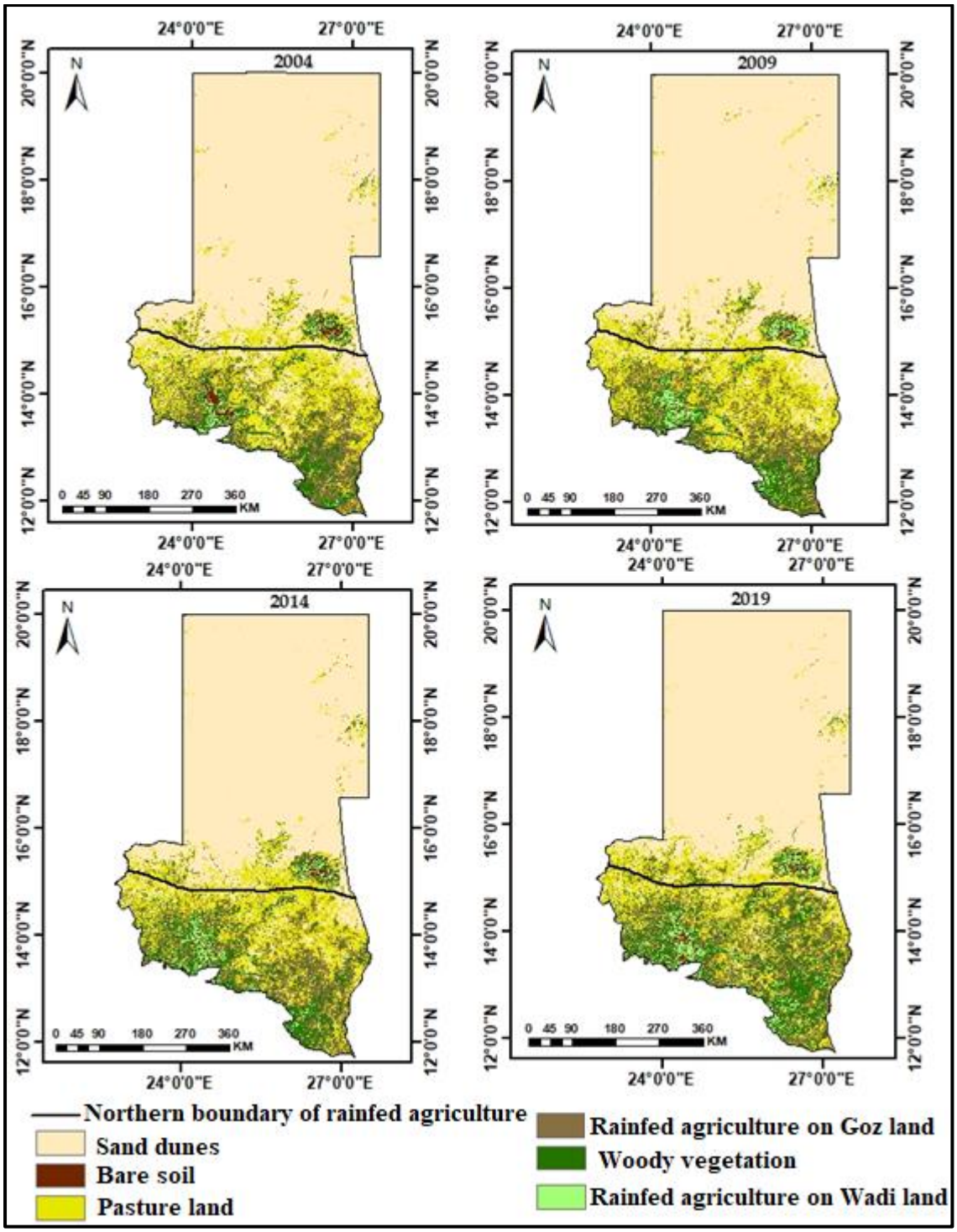


Figure 5.3. Spatial distribution of the rainfed agriculture and other LULC classes in 2004-2009 and 2014-2019. The classification was obtained using Landsat-7 ETM+, Landsat-8 OLI, and random forest classifier.

The 2009 classified map shows that 47.69% (15,128,433.0 ha) of the area was under sand dunes, 19.15% (6075850.59 ha) under pastureland, and 10.8% (3,427,426.53 ha) of the area was under rainfed agriculture in goz land, and woody vegetation occupied 7.87% (2,497,371.93 ha). Further, 10.49% (3327608.88 ha) of North Darfur State was under rainfed agriculture on wadi land, and bare soil covered 4% (1,268,379 ha). In 2014, the classified map of North Darfur State shows that sand dunes covered 53.90% (17,098,441.11 ha), followed by pastureland at 13.03% (4,135,044.24 ha), while rainfed agriculture on goz land accounted for 12.46% (3,952,211.58 ha) of the area. Woody vegetation covered 10.96% (3,478,485.15 ha), and rainfed agriculture on wadi land occupied 6.56% (2,082,289.68 ha). The bare soil took up at least 3.09% (978,837.93 ha) of the study area.

The 2019 classified map shows that around 54.09% (17,161,364.97 ha) of North Darfur State was covered by sand dunes, followed by pastureland, which was estimated at 13.13% (4,164,688.62 ha). In contrast, rainfed agriculture on goz land covered 12.34% (3,917,382.48 ha), and woody vegetation took up 8.58% (2,722,680.9 ha) of the area. The map shows that the rainfed agriculture on wadi land covered 8.39% (2,662,804.71 ha), and bare soil comprised 3.46% (1,096,148.25 ha) of the area.

Table 5.2: Area coverage in hectares of rainfed agriculture and other LULC classes for the period between 1984 and 2019.

Class	1984 Area (ha)	1989 Area (ha)	1994 Area (ha)	1999 Area (ha)	2004 Area (ha)	2009 Area (ha)	2014 Area (ha)	2019 Area (ha)
BS	829,963.35	1,092,219.57	596,770.74	554,768.19	1,048,919.04	1,268,379.0	978,837.93	1,096,148.25
PL	6,087,037.68	5,316,714.45	4230, 389.88	3,165,771.51	5,572,342.98	6075850.59	4,135,044.24	4,164,688.62
RG	3,997,107.09	4,120,391.79	3,919,095.54	48, 087,18.01	4,085,995.14	3,427,426.53	3,952,211.58	3,917,382.48
SD	15,491,287.71	15,001,726.86	17,586,085.59	18,438,988.41	15,579,090.63	15,128,433.0	17,098,441.11	17,161,364.97
WV	3,255,871.68	3,155,611.14	2,809,914.39	2,155,598.64	2,586,354.75	2,497,371.93	3,478,485.15	2,722,680.9
RW	2,063,802.42	3,038,405.4	2,582,809.29	2,400,107.49	2,852,367.39	33,276,08.88	2,082,289.68	2,662,804.71

NOTE: BS = bare soil, PL = pastureland, RG = rainfed agriculture on goz land, SD = sand dunes, WV = woody vegetation, RW = rainfed wadi land

5.3.2 Accuracy Assessment

The classification accuracies were calculated using a confusion matrix and the test dataset (30%). The results are shown in Figure 5.4. The overall classification accuracies ranged from 94% to 97%, and the kappa statistics ranged from 0.96 to 0.93. Notably, the 1994 image classification had the highest overall accuracy of 96.9 and a Kappa statistics value of 0.96%. The classification accuracy for the 2009 image was relatively lower, with an overall accuracy of 94.7 and a Kappa statistics value of 0.94% compared to other classified images. Table 5.3 shows the PA and UA for rainfed agriculture on goz land, rainfed agriculture on wadi land and other LULC in the study area.

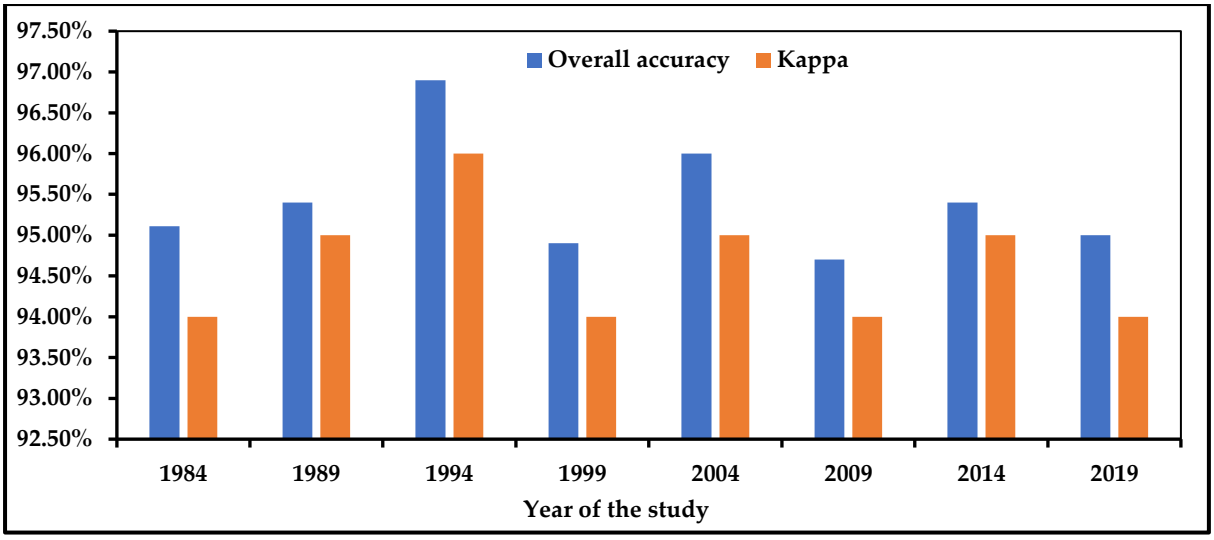


Figure 5.4. The overall accuracy and kappa coefficient achieved by random forest classifier for mapping rainfed agriculture and other LULC classes for the period between 1984 and 2019 with five years interval.

User's accuracies (UAs) for the rainfed agriculture class ranged from 89.7% to 98.2%, and PAs ranged from 87.9% to 98.3%. User's accuracy (UA) for the land cover classes was over 89%. The highest UA was achieved by rainfed agriculture on wadi land (RW) at 98.2% in 1994 and sand dunes (SD) at 97.8% in 2004 as compared to the other land cover classes. The lowest UA was recorded by bare soil (BS) at 89.7% in 2019. Similarly, all land use-land cover (LULC) classes achieved over 85% PA. The highest PA was recorded for sand dunes (SD) at 98.1% in 2004 and for rainfed agriculture on wadi land (RW) at 98.3% in 1994. The lowest PA was reported for pasture land (PL) at 87.9% in 1984 (Table 5.3).

Table 5.3: User and producer accuracies for mapping rainfed agriculture and other LULC classes for the period between 1984 and 2019 in five-year intervals. The accuracies were calculated using the test dataset (30%) and the confusion matrix.

Years\Accuracy Types	BS	PL	RG	SD	WV	RW
1984 Producer	95.7	87.9	96.2	96.6	95.7	96.0
1984 User	93.1	90.1	95.8	95.9	95.3	97.2
1989 Producer	92.7	94.5	96.9	95.8	95.4	95.9
1989 User	91.6	96.5	96.5	95.8	96.3	94.4
1994 Producer	96.4	97.6	95.8	96.1	97.4	98.3
1994 User	97.4	96.7	96.7	96.5	93.8	98.2
1999 Producer	93.8	90.5	95.1	98.1	92.4	95.8
1999 User	92.4	93.7	95.5	96.8	95.5	94.9
2004 Producer	94.7	96.1	97.2	98.1	92.1	96.2
2004 User	97.4	95	96.3	97.8	92.3	97.4
2009 Producer	89.5	92.8	94.7	98.2	96.3	93.2
2009 User	92.3	94.8	95.4	95.6	94.1	95.8
2014 Producer	93.7	96.3	95.1	97.7	94.4	95.6

2014 User	97.2	95.9	95.8	94.9	91.7	96.9
2019 Producer	94.6	96.8	95.1	98.5	93.6	92.7
2019 User	89.7	95.2	95.9	94.9	96.4	96.2

NOTE: BS = bare soil, PL = pasture land, RG = rainfed agriculture on goz land, SD = sand dunes, WV = woody vegetation, RW = rainfed agriculture on wadi land.

5.3.3 Spatio-temporal trends of the rainfed agriculture and other land cover classes

The classification results were compared to determine the magnitude of changes in rainfed agricultural land use and other LULC classes (Figure 5.5). The Figure indicates that there have been significant changes and transitions among various land use/cover classes over the last four decades (1984 to 2019). The main changes and transitions are among agricultural land types and vegetation cover.

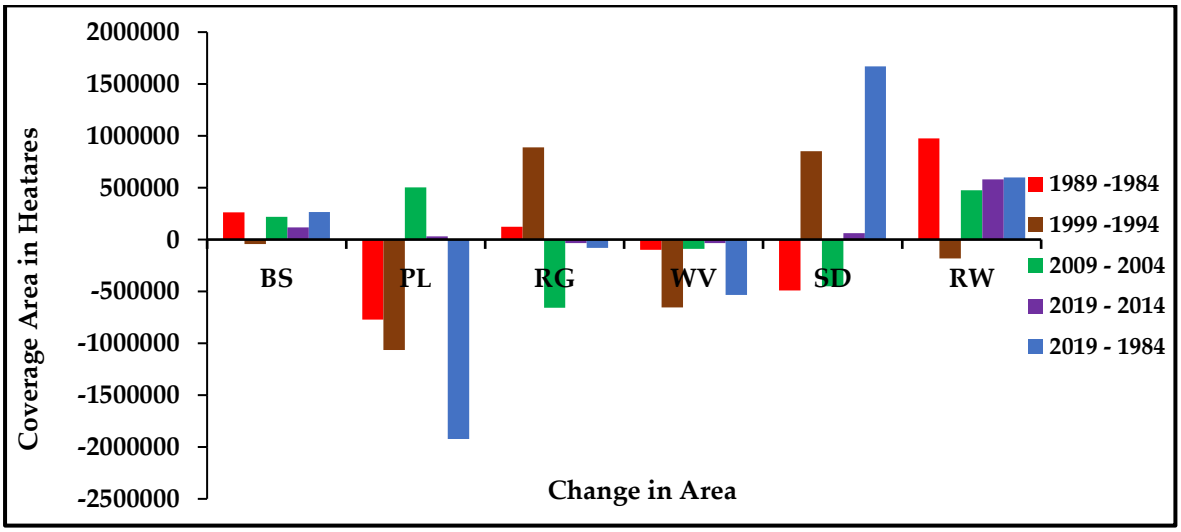


Figure 5.5. The magnitude of change for rainfed agriculture lands and other LULC types (BS = bare soil, PL = pastureland, RG = rainfed agriculture on goz land, SD = sand dunes, WV = woody vegetation, RW = rainfed agriculture on wadi land) of North Darfur from 2019-1984.

5.3.3.1 Trends in rainfed agriculture and other land cover classes from 1984 to 1989

In this period, rainfed agriculture on goz land maintained 159,112.00 ha of its initial area and expanded by 123,284.7 ha into new areas between 1984 and 1989 by gaining 418.7 ha from sand dunes, 279.9 ha from woody vegetation, and 61,651.4 ha from rainfed agriculture on wadi land. Rainfed agriculture on wadi land maintained 117,497.7 ha of the initial area and increased by an area of 974,602.98 ha because it gained 283.03 ha from woody vegetation, 2,872.98 ha from pastureland, and 1,445.50 ha from sand dunes (Figure 5.5 and Table 5.4.). It is also

interesting to note that the bare soil maintained 15,046.8 ha of its initial area, expanding to 262,256.22 ha, and gaining 29.81 ha from pastureland. It further gained 122.23 ha from rainfed agriculture on goz land and 486.23 ha from woody vegetation. Meanwhile, pastureland maintained 208,773.2 ha of its initial area but decreased by 770,323.23 ha during these five years, whereas 29.8 ha changed into bare soil, and 2,872.9 ha was converted into rainfed agriculture on wadi land. A further 5.13 ha changed from pastureland into woody vegetation (Figure 5.5 and Table 5.4.)

Table 5.4: Change matrix of the rainfed agriculture and other LULC types in hectares of North Darfur State from 1984 to 1989. The bold values in the change matrix indicate unchanged land types between the initial and final years.

		INITIAL STATE 1984						
		BS	**PL**	**RG**	**SD**	**WV**	**RW**	**Total**
FINAL STATE 1989	**BS**	**15,046.80**	29.81	122.23	804.90	486.23	1,507.02	17996.98
	PL	72.1	**208,773.20**	85,505.09	11,589.50	13.00	15,124.68	321077.57
	RG	95.43	41,758.94	**159,112.00**	418.70	279.97	61,651.45	263316.5
	SD	1,297.30	43,977.31	32,404.27	**48,065.40**	31.28	3,772.72	129,520.1
	WV	1,111.82	5.13	53.80	351.31	**171.40**	497.412	2,190.873
	RW	979.22	2,872.98	41,783.83	1,445.50	283.03	**117,497.70**	164,862.3
	Total	18,537.77	297,417.40	318,981.20	62,675.31	1,236.761	200,051.00	898,899.4
	Image difference	-48.88	23,595.31	-55,664.73	68,134.91	603.15	-36,619.76	

NOTE: BS = bare soil, PL = pastureland, RG = rainfed agriculture on goz land, SD = sand dunes, WV = woody vegetation, RW = rainfed agriculture on wadi land.

5.3.3.2 Trends in rainfed agriculture and other land cover classes from 1994 to 1999

The rainfed agriculture on goz land retained 88,305.13 ha of its initial area and increased 889,622.46 ha via 158.7 from the transformation of bare soil, 3,098.0 ha from pastureland, 663.6 ha from sand dunes, and 37,301.7 ha from rainfed agriculture on wadi land. However, the rainfed agriculture on wadi land maintained 72,346.17 ha of the initial cover area but decreased by around 182,701.8 ha (with 1,060.0 ha lost to bare soil, 37,301.0 ha into rainfed agriculture on goz land and 694.1 ha to sand dunes (Figure 5.5 and Table 5.5). During this period, bare soil maintained 18,385.5 ha and decreased by 42,002.55 ha, with 21.2 ha changed to pastureland and 158.7 ha transformed into rainfed agriculture on goz land. There was further a loss of 5,591.4 ha to sand dunes. Pastureland maintained 52,827.9 ha of the initial classification and decreased by an area of 1,064,618.37 ha (with 2,133.99 ha changed into sand dunes, 118.48 ha transformed into bare soil, and 3,098 ha on goz land becoming rainfed

agricultural land, and a further 910.37 ha transformed into woody vegetation (Figure 5.5 and Table 5.5).

Table 5.5: Change matrix of the rainfed agriculture and other LULC types of North Darfur State in hectares from 1994 to 1999. The bold values in the change matrix indicate unchanged land types between the initial and final years.

		INITIAL STATE 1994						
		BS	**PL**	**RG**	**SD**	**WV**	**RW**	**Total**
FINAL STATE 1999	**BS**	**18,385.5**	118.48	570.41	9,165.10	3,986.31	1,060.09	33,285.89
	PL	21.22	**52,827.90**	16,730.92	9,785.05	352.81	3,090.45	82,808.35
	RG	158.71	3,098.00	**88,305.13**	663.55	4,034.80	37,301.67	161,443.90
	SD	5,591.4	2,133.99	393.12	**5,517.13**	231.90	694.10	1,4561.64
	WV	6,854.67	910.37	2,147.27	632.94	**30,085.10**	17,869.56	58,499.91
	RW	1,845.35	5,410.52	41,580.27	1,069.50	19,959.00	**72,346.17**	142,210.80
	Total	32,856.85	92,381.26	149,727.10	26,833.27	58,649.92	132,362.00	475,637.67
	Image difference	429.04	-9,572.91	11,716.74	-12,271.60	-150.01	9,848.77	

NOTE: BS = bare soil, PL = pastureland, RG = rainfed agriculture on goz land, SD = sand dunes, WV = woody vegetation, RW = rainfed wadi land.

5.3.3.3 Trends in rainfed agriculture and other land cover classes from 2004 to 2009

This period shows a significant decline in rainfed agriculture on goz land (658,568.61 ha) and maintaining just 131,389.00 ha of its initial state. This decline was the result of 868.71 ha lost to woody vegetation, 21,091.70 ha transformed into rainfed agriculture on wadi land, and 63,336.03 ha becoming pastureland, while rainfed agriculture on wadi land maintained 72,582.91 ha while also showing an increment of 475,241.49 ha. This increment was 1,489.39 ha from pastureland, 21,091.70 ha from rainfed agriculture on goz land, and 14,348.10 ha gained woody vegetation (Figure 5.5 and Table 5.6). Bare soil maintained 17,032.80 ha but increased by 219,459.96 ha, gained by 10.40 h from pastureland, 320.57 ha from rainfed agriculture on wadi land and 6,807.70 ha from woody vegetation. In contrast, pastureland maintained 31,568.5 ha of its initial state while increasing by 503,507.61 ha (resulting from gains of 63,336.03 ha from rainfed agriculture on goz land and 140.052 ha from woody vegetation (Figure 5.5 and Table 5.6).

Table 5.6: Change matrix of the rainfed agriculture and other LULC types of North Darfur State in hectares from 2004 to 2009. The bold values in the change matrix indicate unchanged land types between the initial and final years.

		INITIAL STATE 2004						
		BS	**PL**	**RG**	**SD**	**WV**	**RW**	**Total**
FINAL STATE 2009	**BS**	**17,032.80**	10.40	24.312	91,873.10	6,807.70	320.57	116,068.9
	PL	13.05	**141,499.50**	63,336.03	5,872.80	140.052	5,328.17	216,189.6
	RG	431.25	25,311.30	**131,389.00**	2,011.46	1,449.68	44,494.65	204,699.2
	SD	192.10	42,262.14	3,720.20	**41,957.00**	907.90	210.88	89,250.2
	WV	4,004.68	715.02	868.71	7,561.90	**31,568.50**	9,117.55	53,192.8
	RW	1,489.39	1,469.56	21,091.70	1,754.07	14,348.10	**72,582.91**	112,735.7
	Total	22,775.15	210,624.4	220,430.0	151,030.3	55,221.93	132,054.7	792,136.5
	Image difference	93,293.73	5,565.20	-15,730.7	-61,780.1	-2,029.08	-19,319.0	

NOTE: BS = bare soil, PL = pasture land, RG = rainfed agriculture on goz land, SD = sand dunes, WV = woody vegetation, RW = rainfed agriculture on wadi land.

5.3.3.4 Trends of rainfed agriculture and other land cover classes from 2014 to 2019

The rainfed agriculture on goz land maintained 91,644.91 ha of the initial area and decreased by 34,829.1 ha. This reduction resulted from a loss of 485.17 ha to bare soil, 1,625.43 ha to woody vegetation, 1,222.68 ha to sand dunes and 16,800.80 ha transformed into rainfed agriculture on wadi land. The rainfed agriculture on wadi land maintained 79,704.27 ha and showed an increment of 580,515.03 ha (resulting from 2,247.70 ha gained from bare soil, 1,779.92 ha from pastureland and 716.4 ha from sand dunes) (Figure 5.5 and Table 5.7). The bare soil maintained 22,383.1 ha of its initial area and expanded by 117,310.32 ha (84.61 ha from pastureland, 485.17 ha from rainfed agriculture on goz land, and 9,172.8 ha from sand dunes). Similarly, the pastureland maintained 25,370.4 ha of its initial area and extended by 29,644.38 ha (17,985.62 ha from rainfed agriculture on Goz land, 160.18 ha from woody vegetation, 7,579.45 ha from sand dunes, and 160.18 ha from woody vegetation) (Figure 5.5 and Table 5.7).

Table 5.7: Change matrix of the rainfed agriculture and other LULC types of North Darfur State in hectares from 2014 to 2019. The bold values in the change matrix indicate unchanged land types between the initial and final years.

		INITIAL STATE 2014						
		BS	**PL**	**RG**	**SD**	**WV**	**RW**	**Total**
FINAL STATE 2019	**BS**	**22,383.1**	84.61	485.17	9,172.8	3,810.49	685.50	36,621.67
	PL	88.8	**25,370.4**	17,985.62	7,579.45	160.18	110.1	51,294.55
	RG	99.28	1,7951.2	**91,644.91**	686.31	3,627.22	39,411.50	15,3420.4
	SD	187.14	4,890.45	1,222.68	**14,668.8**	42.2	101.50	21,112.77

WV	1,027.6	295.69	1,625.43	2071.4	**47,767.8**	11,759.44	64,547.36
RW	2,247.70	1,779.92	16,800.80	716.4	34,313.0	**79,704.27**	135,562.1
Total	26,033.62	50,372.27	129,764.6	34,895.16	89,720.89	131,772.3	462,558.9
Image difference	10,588.05	922.28	23,655.81	-13,782.4	-25,173.5	3,789.78	

NOTE: BS = bare soil, PL = pastureland, RG = rainfed agriculture on goz land, SD = sand dunes, WV = woody vegetation, RW = rainfed agriculture on wadi land

The general trends of rainfed agriculture from 1984 to 2019 are summarised in Figure 5.6. Variability in the rainfall results in variability in total areas of rainfed agriculture in both wadi and goz land, although this is especially high in wadi lands.

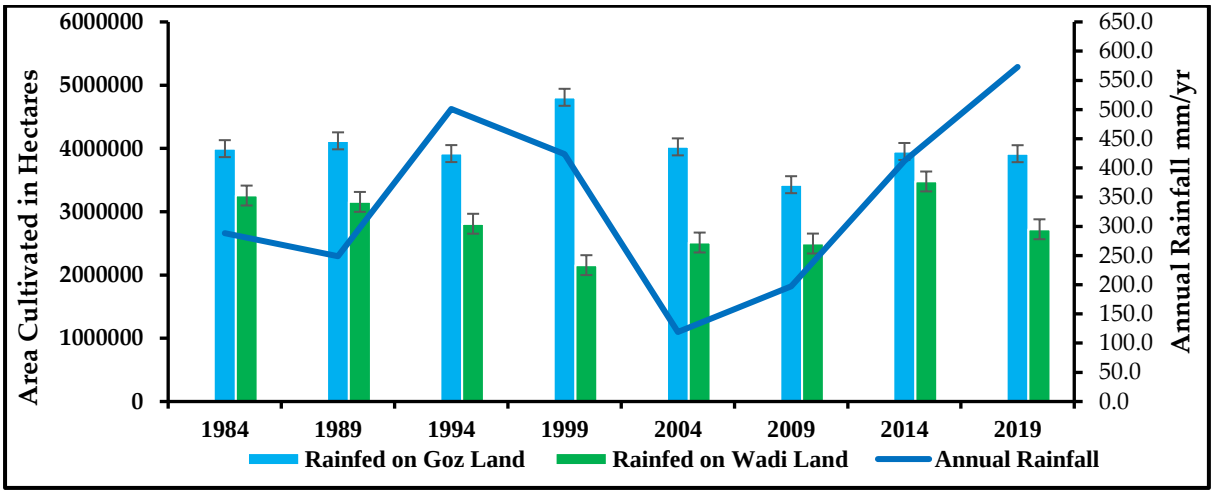


Figure 5.6. Compare area coverage by rainfed agriculture on goz land (RG) and on wadi lands (RW) and mean annual rainfall from 1984 to 2019.

5.4 Discussion

This research attempted to map and monitor the patterns of rainfed agriculture in North Darfur State over the last 35 years using a supervised classifier algorithm, i.e., random forest (RF) and multitemporal Landsat images. This is critically important in providing up-to-date information about agricultural lands (Figures 5.2 and 5.3) and the spatial distribution of crops, which decision-makers and planners could be used to estimate food production. The lack of spatial data infrastructure at all levels of government in the Darfur States has been reported as a major barrier to quick access to data availability and sharing for effective management (Nakalembe *et al.*, 2021). The state usually conduct two traditional field-based surveys to estimate the crops, especially millet. These two surveys run through informal interviews with the farmers after

planting and post-harvesting. Owing to poor accessibility, civil wars, and time-consuming interview methods, the field survey approach is ordinarily incomplete and unreliable. Despite this, this study shows the potential of earth observation techniques in mapping and monitoring rainfed agriculture in a hot civil war area. Despite the challenge of the rainfed agriculture spectral signature due to the small scale of the farms, low crop density, and open canopies, the study obtained high overall accuracies ranging between 94.7% and 96.9%. The accuracies achieved are comparable to previous studies conducted in a similar landscape, such as those by Ibrahim, (Ibrahim, 1984) which investigated land use land cover (LULC) changes over four decades in the Ghubaysh area, Sudan. Their study achieved overall accuracies (OAs) ranging from 89.6% to 98.2%. Furthermore, high OAs ranging from 86% to 96% were reported by Biro *et al*. (Biro *et al.*, 2013) in mapping LULC changes in the Northern part of the Gadarif region, Sudan. More specifically, the user's and the producer's accuracies obtained in this study for rainfed agriculture compare favourably with another study in a semi-arid environment in the Niger Delta Region (Nababa *et al.*, 2020).

Results of this study revealed that rainfed agriculture on goz and wadi lands in North Darfur State underwent significant changes, as shown in Figures 5.2 and 5.3 and Table 5.2. These changes have varied over time, space, and magnitude. The changes in agricultural land use can be attributed to population growth and climate change, specifically spatial and temporal rainfall variability. Studies have shown that the Sahel zone, in general, is overpopulated, even though the average population density in the Sahel zone is less than ten inhabitants per square kilometre (Ibrahim, 1978). This is owing to two reasons; first, the population is concentrated in regions where the drinking water supply is secured. Second, soil productivity is comparatively low. To compensate for lower yields resulting from high spatial and temporal variability in the rainfall and the loss of soil productivity, the farmers tend to cultivate a larger area falling in different locations better to meet their respective families' food security needs. This practice helps ensure that some fields get sufficient rainfall, even if others do not receive rain due to the variability. Similarly, in polygamous households, different wives would be responsible for cultivating different plots located far from each other as a risk-spreading strategy (Ibrahim, 1982). This was confirmed by Osman (Osman and Cohen, 2014), who, in their 2014 study, observed that there had been an expansion in rainfed agricultural land use in North Darfur State since the 1960s.

The findings of this study reveal that rainfed agriculture on wadi land (RW) has shown ongoing expansion since 1994. In particular, from 2004 to 2009, the extent and location of rainfed agriculture on wadi and goz lands changed significantly. There was an increase of 475,241.49 ha in wadi land and a decline of 658,568.61 ha in goz land, as shown in (Figure 4.5). This is confirmed by Osman (Osman, 2012), who stated that the land tenure system and rainfall variability have greatly affected rainfed agriculture in North Darfur State. This could be attributed to a decline in soil fertility in goz land from over-cultivation, desertification and the expansion of sand dunes (Ali and Mohamedain, 2016). Over-cultivation can also be seen throughout the multitemporal images in the surroundings of settlements, where the soil is also exhausted, and there is a concentration of desertification phenomena. The farmers have long realised the importance of the fertile alluvial soil in the wadi lands for cultivating vegetables and snuff tobacco to compensate for the yield reduction in the goz lands. Thus, the noticeable expansion from 1994 in rainfed agriculture on wadi land (as observed in this study) is hardly surprising. Of concern, however, is that only a few farmers have access to the fertile wadi lands—many studies have indicated that the limited access to fertile soil, such as the wadi bed land, contributes significantly to the current conflict in North Darfur (Abdul-Jalil *et al.*, 2013; Osman and Cohen, 2014). Local communities have adopted different strategies to cope with the current deterioration in the productivity and the profitability of rainfed agriculture in the goz lands. For example, farmers have intensified cultivation to compensate for lower yields. This can be seen in the study area in the widespread cultivation that extends beyond the climatically adapted agronomic dry limit, where the average rainfall is less than 500 mm (Ibrahim, 1984). Rainfed cultivation in inappropriate areas has led to cumulatively impoverishing the environment. Prior to tilling the land, farmers aggressively clear the land of vegetation, further reducing the fallow period. Losing vegetation over ever-larger ecologically vulnerable areas makes the sandy soil more susceptible to wind erosion and dune movement toward the northern part of the region (Fuller, 1987a). The spread of the dunes can be seen in the classified images for the study years, particularly 2014 and 2019 (Figure 5.3). Many studies have therefore concluded that rainfed cultivation is potentially the main factor contributing to desertification in Darfur (Ali and Mohamedain, 2016; Ibrahim, 1982). With the intensive current rainfed cultivation and the scarcity of unused arable land, it remains unclear how the region will be able to increase its agricultural production and thus keep pace with population growth.

We have seen the expansion of rainfed cultivation in the southern part owing to the relatively high rainfall. Therefore, since the early 1970s, there has been some population movement from North Darfur to South Darfur. However, the acute drought periods experienced most intensely in the area, during years including 1983, 1985 and 1994, have greatly accelerated the population movement into Northern Darfur from South Darfur. The massive "agro-migrant" and occupation of lands in Northern Darfur have escalated the overall conflict and the emergence of extreme dilemmas in the socio-political landscape, which are proving difficult to engage in a sustainable peace process.

Although the study provides a basis for constructing reliable spatial information on rainfed agriculture and other land cover patterns, it also has some limitations. Some concerns should be addressed when the proposed method is used in real-world applications. The reference data used to classify and validate the histological images need to be strengthened by some more ground data. The ground and higher spatial resolution data, such as Sentinel-2, would better enhance the rainfed agriculture mapping to the crop type level in the sand dune and Goz lands.

5.5 Conclusions

Understanding the spatio-temporal dynamic of rainfed agriculture in the North Darfur region is particularly crucial, but challenging. This study aimed to test the ability of earth observation data to assess the trends of rainfed agricultural lands and other common LULC types in the North Darfur region. The results show that Landsat images are promising in monitoring the Spatiotemporal patterns of rainfed agriculture in both the goz and wadi areas and other land cover classes, with overall accuracies ranging from 94% to 97% and the kappa statistics ranging from 0.93 to 0.96. A high spatial and temporal variability characterises the rainfed agriculture patterns. The cultivation areas have been extended beyond the climate-adapted agronomic dry limit of less than 500 mm of average rainfall to compensate for lower yields. Such widespread cultivation in ecologically vulnerable areas may contribute to land degradation. The study also shows that since 1994, the rainfed agriculture on wadi land has significantly extended. Unfortunately, the wadi lands are limited, which may foment disputes between local communities. Our work sheds some light on the Spatio-temporal pattern of rainfed agriculture

in the Northern Darfur State, where spatial data on environmental and socio-economic activities is lacking owing to ongoing conflicts.

Further studies may need to be conducted to understand better the factors that drive the spatial distribution of rainfed agriculture and their environmental impacts. This could contribute to developing effective strategies for sustainable agricultural land use.

CHAPTER SIX

Synthesis

6.1 Introduction

Rainfed agriculture supports approximately 60% of the world's population and is the primary source of food and nutrition (Biradar *et al.*, 2009). Almost 80% of the agricultural land worldwide is under rainfed agriculture, characterised by low yield levels and high on-farm water losses (Rockström *et al.*, 2003). In Sub-Saharan Africa, more than 95% of the farmed land is rainfed agriculture, especially in arid and semi-arid regions (Tubiello *et al.*, 2013; Wani *et al.*, 2009). On average, rainfed agriculture contributes about 35% of gross domestic product (GDP) and employs 70% of the population (Wani *et al.*, 2009). North Darfur State, Sudan depends on rainfed agriculture, the principal source of income and livelihood for 60% to 80% of the population (Elgali *et al.*, 2010; Siddig *et al.*, 2018).

Understanding the spatio-temporal dynamic of rainfed agriculture and its underlying climatic factors plays a key role in promoting food security and socio-political stability, and the preservation and restoration of ecosystem services (De Marinis *et al.*, 2021; Thyagharajan and Vignesh, 2019). The lack of availability of spatial data for monitoring trends in rainfed agriculture is not only a threat to food security but also an impediment to understanding the study area's environment, climatic hazards, and socio-economic dynamics. Owing to political instability in some parts of North Darfur State, traditional approaches to agricultural monitoring, such as expert scouting estimates, crop cut information, field assessment, and surveys, pose extreme danger to field teams, in addition to significant financial costs (Nakalembe *et al.*, 2021). Satellite remote sensing (RS) offers useful analysis tools for monitoring rainfed agriculture since its data has continuous spatial coverage, is freely accessible, and can be acquired at high temporal resolutions (Schaefer and Thinh, 2019).

This research work aimed to map and monitor rainfall variability impacts on rainfed agriculture in arid environments, using different remote sensing datasets, including satellite precipitation products data, Sentinel-2 MSI Level-1C TOA reflectance images and multitemporal Landsat observation dataset. The objectives of this thesis were as follows:

1. To evaluate the feasibility of satellite precipitation products (SPPs) in estimating the spatio-temporal rainfall variability across North Darfur State, Sudan.
2. To mapping crop types in a highly heterogeneous semi-arid Environment using Sentinel-2 datasets and machine learning (ML) algorithms on the Google Earth Engine (GEE) cloud.

3. To analyse spatio-temporal drought trends and impact on millet crop production across North Darfur State using standardized precipitation index (SPI) and reconnaissance drought index (RDI).
4. To map and monitor spatio-temporal patterns of rainfed agricultural lands of North Darfur State, Sudan, using earth observation data (EOD).

6.2 Evaluating satellite precipitation products in capturing the spatio-temporal rainfall variability across North Darfur State, Sudan.

Rainfall is essential for the Earth's water cycle, which interconnects the land, atmosphere, and oceans and significantly influences the planet's climate system (Choubin *et al.*, 2019; Wedajo *et al.*, 2021). Reliable rainfall measurement is the key of understanding the spatio-temporal variability of rainfall at various time scales and its effect on agriculture monitoring, hydrology, and ecosystem functioning (Ayehu *et al.*, 2018). Usually, rain gauge observations have been used to analysis the spatio-temporal variability of rainfall (Zambrano-Bigiarini *et al.*, 2017a). Due to various reasons, rainfall data is often unavailable, and the quality is poor or inaccessible (Field and Barros, 2014). Remote sensing provides an alternative approach to ground-based rainfall measurement and monitoring methods. Rainfall data can be collected from satellite-based products (Ayehu *et al.*, 2018). Hence, there is a need to identify a satellite product with abilities to detect rainfall variability. This study, therefore, aimed to estimate rainfall variability across North Darfur State at daily, monthly and annual timescales using various satellite precipitation products (SPPs) to inform decisions in water management and agriculture monitoring.

The feasibility of six SPPs, i.e. Tropical Rainfall Measuring Mission (TRMM) Multi-satellite Precipitation Analysis (TMPA), African Rainfall Climatology (ARC), Climate Hazards Group Infrared Precipitation with Station Data (CHIRPS), Integrated Multi-satellitE Retrievals for Global Precipitation Measurements (GPM) Final Run (GPMIMERG), Precipitation Estimation from Remote Sensing Information using Artificial Neural Networks-Climate Data Record (PERSIANN-CDR), and the Tropical Applications of Meteorology using SATellite and ground-based observations (TAMSAT) in detecting rainfall variability was evaluated using four categorical indices, i.e., the probability of detection (POD), probability of false alarm (POFA), bias in detection (BID) and Heidke skill score (HSS), and four continuous

indices, i.e., the Pearson correlation coefficient (r), the root mean square error (RMSE), the per cent bias (Pbias), and the Nash-Sutcliffe model efficiency coefficient (NSE) against ground-rain-gauges. This study's results have shown a medium agreement between satellite precipitation products and rain gauge measurements, i.e., the correlation coefficient r ranged from 0.37 to 0.52 and Nash-Sutcliffe model efficiency (NSE) coefficient. Overall, CHIRPS 2.0 was the best-performing product, followed by Tropical Applications of Meteorology using SATellite and ground-based observations (TAMSAT 3.1) at a daily time scale. However, monthly time scale results show reliable agreement between the six SPPs and ground-based rain gauge measurements, with the NSE coefficient ranging from 0.36 to 0.49 and a strong correlation coefficient of $r \geq 0.66$. Based on the statistical analysis, TAMSAT 3.1 performed better in estimating the monthly rainfall in the region. At the annual time scale, the results showed strong agreement between the six SPPs and rain gauge measurements as demonstrated by annual comparisons, which produced NSE coefficients ranging from 0.19 to 0.61 and correlation coefficients (r) ranging from 0.58 to 0.81.

6.3 Mapping crop types in a highly heterogeneous arid Environment using Sentinel-2 datasets and machine learning (ML) algorithms on the Google Earth Engine (GEE) cloud

Satellite RS is an efficient tool for spatio-temporal monitoring crops, i.e., evaluating actual distribution, identifying crop types and assessing nutrient status, and predicting yields—this not only saves time but also conserves resources in agricultural management (Asgarian *et al.*, 2016; Kosari *et al.*, 2020). However, monitoring crops using remote sensing technologies in heterogeneous arid environments such as North Darfur State faces frequent hindrances due to challenges such as high soil background reflectance, the coexistence of green and senescent grasses, limited input datasets, and the prevalence of shrubs in grasslands, which share similar reflective characteristics to cropland (Qader *et al.*, 2021; Tran *et al.*, 2022). The North Darfur State has a heterogeneous arid and semi-arid environment characterised by various land use/land cover such as vast sand dunes, grassland, and open canopy croplands (Mohmmed *et al.*, 2018). The spatial distribution of cropland in North Darfur State lies between the 250 mm and 600 mm isohyets and shows wide disparity on goz (sandy) soils, including millet, Groundnuts and sesame, and in the clay soils located along alluvial and seasonal valleys (known as wadis) originating in the Jebel Marra volcanic massif and the surrounding Basement

Complex hills including Tobacco and vegetables (Osman and Cohen, 2014; Young *et al.*, 2005).

The RF and SVM machine learning (ML) classifiers were used in this work to map cropland and common land use/land cover on the Sentinel-2 (S2) dataset. This study examined the capability of optical data and vegetation indices to mapping cropland and other LULC in a heterogeneous arid environments using high-resolution Sentinel-2 imagery. The RF and SVM effectiveness in classifying crop types in the study area was compared. The results showed that RF and SVM classifiers effectively mapped crop types. The S2's visible and near-infrared (VNIR) bands and the ten S2 bands (B2, B3, B4, B5, B6, B7, B8, B8A, B11, B12) datasets reported relatively higher classification accuracies than the other datasets for the RF classifier, i.e., 97.1% and 97%, respectively. An integrated dataset comprising ten S2 bands and eight vegetation indices (VIs) achieved the same overall accuracy (OA) as the VSWIR dataset, i.e., 96.5%. Therefore, VIs in the ten S2 bands/VIs dataset improved the negative effects associated with large sets of correlated variables and decreased the classification accuracies. The eight VIs dataset reported the lowest classification accuracies reported by both RF and SVM.

6.4 Spatio-temporal analysis of drought and impact on millet crop production across North Darfur State using standardized precipitation index (SPI) and reconnaissance drought index (RDI)

Drought is one of the most common natural disasters, and it significantly impacts the agricultural economy, changes soil properties and vegetation structure (Yao *et al.*, 2018; Zarch *et al.*, 2015). Droughts are slow-onset disasters with neither a clear beginning nor end—they are a creeping phenomenon that operates on different time scales and severely impacts economies. Drought causes more damage to agricultural productivity than other common disasters (Lesk *et al.*, 2016). Studying droughts is crucial for evaluating agricultural production in countries heavily relying on rainfed agriculture (Masupha and Moeletsi, 2018). However, Sudan suffered from severe droughts during the 20th century, i.e., from 1972 to 1979 and 1980 to 1984, which led to a significant drop in crop production and 4.5 million people suffered from hunger (Atiem *et al.*, 2022; Elhag and Zhang, 2018). The study area experiences exacerbated variability in rainfall, leading to frequent droughts and crop failure, therefore it is necessary to assess the drought impacts on rainfed agriculture.

Therefore, the study examined the performance of the standardized precipitation index (SPI) and the reconnaissance drought index (RDI) for the 3-month (June-August), 6-month

(June-November), and 9-month (June-February) timescales in evaluating the spatiotemporal trend of drought events and their impact on millet production in North Darfur State, Sudan, from 1981 to 2020. The Pearson correlation coefficients (r) was used to assess the drought-yield relationship. The results indicated that the RDI is more sensitive to variabilities than the SPI for detecting drought trends. Drought events affected North Darfur over broad spatial extents, particularly in 1989, 1990, 1992, 1999, and 2001—an extreme drought event was in 2003. The correlation coefficient analysis (r) between the SPI and RDI and the standardized variable of crop yield (SVCY) for millet grain yield showed a strong agreement between them. Moderate to extreme reductions in millet crop yield occurred in 1992, 1999, 2001, and 2003, corresponding to the moderate to extreme drought indicated by the RDI. Severe crop losses were in Kabkabiya and Umm Kadadda.

6.5 Mapping and monitoring spatio-temporal patterns of rainfed agriculture lands of North Darfur State, Sudan, using earth observation data

Understanding the spatio-temporal dynamic of rainfed agriculture and its determining climatic factors in the study area can play a key role in promoting food security and socio-political stability, as well as in protecting and restoring ecosystem services (De Marinis *et al.*, 2021; Elagib *et al.*, 2021; Thyagharajan and Vignesh, 2019). The lack of availability of spatial data for monitoring trends in rainfed agriculture is not only a threat to food security but also an impediment to understanding the study area's environment, climatic hazards, and socio-economic dynamics. Owing to political instability in some parts of the study area, traditional approaches to agricultural monitoring, such as expert scouting estimates, crop cut information, field assessment, and surveys, pose extreme danger to field teams, in addition to significant financial costs (Nakalembe *et al.*, 2021; Sahajpal *et al.*, 2020). Nowadays, most of these events can be predicted, and data and tools can provide early warning and impact assessment; this underscores the importance of timely and accurate production forecasts and near-real-time agricultural monitoring (Nakalembe *et al.*, 2021; Sahajpal *et al.*, 2020). Satellite remote sensing (RS) offers useful analysis tools in several technical-scientific fields. Remote sensing (RS) has been used widely worldwide for monitoring the changes in the environment and the identifying their magnitude at different space-temporal resolutions (Carella *et al.*, 2022; Orusa and Borgogno Mondino, 2021; Orusa *et al.*, 2020). In addition, satellite remote sensing is crucial in monitoring rainfed agriculture since its data has continuous spatial coverage, is freely accessible, and can be acquired at high temporal resolutions. This is particularly relevant in

areas where ground data are insufficient, lacking, or unsafe to obtain (Melaas *et al.*, 2013; Rembold *et al.*, 2019; Schaefer and Thinh, 2019; Yang *et al.*, 2012). The North Darfur State heavily depend on rainfed agriculture—more than 90% of cultivated land comprises rainfed farming, which employs 80% of Darfur people, therefore mapping the dynamics of rainfed agriculture is important.

Therefore, the study explored the potential of remote sensing to map and monitor spatio-temporal dynamics of rainfed agriculture in North Darfur State from 1984 to 2019 using multitemporal Landsat observation data. Multitemporal Landsat imagery, i.e. Landsat Multispectral Scanner (MSS), Landsat Thematic Mapper (TM), Landsat Enhanced Thematic Mapper Plus (ETM^{+}) and Landsat Operational Landsat Imageries (OLI) to classify and map dynamics of rainfed agriculture and common land use/ land cover classes in arid desert environment of North Darfur State, using Random forest. The study shows that the Landsat Operational Landsat Imageries (OLI) played the most important data in mapping and monitoring rainfed agriculture, with overall accuracies (OAs) ranging between 94.7% and 96.9%. At the same time, the kappa statistics (κ) were greater than 0.90. The results showed that the high spatial variability in goz land used for rainfed agriculture increased of (889,622.46 ha) over 1994-1999, while it decreased by 658,568.61 ha over the 2004-2009 period south of the 232.9 mm isohyet. Rainfed cultivation of wadi lands expanded significantly by 580,515.03 ha over the 2014-2019 period and decreased by 182,701.8 ha over the 1994-1999 period, especially in the 362.8-477.2 mm isohyets. The findings of this study provide essential spatial data lacking owing to ongoing conflicts—this can help decision-makers formulate sustainable land use monitoring systems.

6.6 Conclusions

The aim of this study was to map and monitor the impacts of rainfall variability on rainfed agriculture patterns in the semi-arid environment of North Darfur State using remote sensing (RS) technology. The outcomes of this study show that RS can be used for mapping and monitor rainfed agriculture in arid environments.

The following conclusions can be made based on main findings made in line with the objectives of the study.

- Several studies have evaluated satellite precipitation products (SPPs) as alternative source rainfall data. Reliable information on precipitation at sufficiently detailed spatio-

temporal scales is essential to assess the impacts on the agricultural economy. However, these studies are mainly conducted at regional scale, encompassing diverse physical and climatic condition across multiple regions.

- The outcomes of this study show that the CHIRPS 2.0 and TAMSAT 3.1 were the best-performing product for detecting rainy days. However, monthly time scale results show reliable agreement between the six SPPs and ground-based rain gauge measurements, with the NSE coefficient ranging from 0.36 to 0.49 and a strong correlation coefficient of $r \geq 0.66$. Based on the statistical analysis, TAMSAT 3.1 performed better than the other SPPs in estimating the monthly rainfall in the region.
- The classification of cropland and coexisting LULC classes in a heterogeneous semi-arid environment using widely machine learning algorithms using optical data S2, the outcomes produced highest accuracies 97% for the RF classifier and 93% for SVM classifier using ten S2 bands (B2, B3, B4, B5, B6, B7, B8, B8A, B11, B12) datasets and produced 97.1% for RF and 93% for SVM using visible bands of S2, while kappa coefficient (κ) range from 0.87–0.96 for RF and range from 0.81–0.94 for SVM.
- Spatio-temporal drought trends evaluated using the reconnaissance drought index (RDI) and the standardized precipitation index (SPI). The study outcomes indicated that (RDI) is more sensitive to variabilities than (SPI) for detecting drought trend events. The outcomes show that the whole of North Darfur State was influenced by extreme drought in 2003.
- Spatio-temporal patterns of rainfed agriculture lands and common LULC classes can be mapped and monitored using earth observation data and produced high accuracies ranging between 94.7% and 96.9%, while the kappa statistics were greater than 0.90 using RF classification algorithm. The results indicated that the high spatial variability in goz land used for rainfed agriculture increased by 889,622.46 ha over between 1994 and 1999, while a decrease of 658,568.61 ha was recorded between 2004 and 2009 south of the 232.9 mm isohyet.

In summary, this study revealed a relatively cost-effective of different techniques for map and monitor rainfed agriculture patterns over large arid environments. The method used in this study can help researchers to repetitively carry out rainfed agriculture surveys and monitoring sites based on spatial analysis. The findings of this study help to understanding spatio-temporal dynamic of rainfed agriculture and quantify specific site of cropland over arid environment of North Darfur.

6.7 The limitation and future research

This work provided good method using for mapping and monitoring rainfed agriculture patterns in arid environment using multitemporal and multispectral Earth observation data. The study recognized that the effective methods and sensors that can using for mapping and monitoring rainfed agriculture in arid areas, several challenges still require the attention of researches.

- In this study four different categorical statistical tools: probability of detection (POD), probability of false alarm (POFA), bias in detection (BID) and Heidke skill score (HSS) were used to assess the ability of each SPPs to correctly detect rainy days , there is require to test other categorises indices (e.g., (fBias) frequency bias and (PC) percent correct) to evaluate the ability of each SPPs to identify different intensities of daily precipitation
- This study was used the Nash-Sutcliffe efficiency (NSE) to evaluate the performance of SPPs to detect spatio-temporal rainfall variability, there need to test other coefficient to assess the SPPs performance i.e., Willmott's index of agreement (d)
- In this study two widely drought indices i.e., reconnaissance drought index (RDI) and the standardized precipitation index (SPI) based on meteorological data were used to evaluate the drought events there is need to utilise other indices based on remote sensing data to monitor the vegetation condition such as Vegetation Condition Index (VCI), indices involving soil moisture information based on microwave remote sensed soil moisture information i.e., Microwave Integrated Drought Index (MIDI) and the Standardized Soil Moisture Index (SSI).
- For the future research to mapping and monitoring rainfed agriculture more reliable could use high-resolution satellite RS images i.e., Quick Bird Worldview (WV-2) and GeEye for improved maps produced accuracies.
- This study was mapped crop types on one grown season using different vegetation indices were extracted from Sentienl-2 multispectral images for monitoring rainfed agriculture in arid environment there is need to apply other method to map crop types such as model and predict crop yield (Bayesian modelling).

References

Abbas, H.and El-Hag, A. 2013. Crop assessment and monitoring for sugarcane crop, Sudan (New Halfa case study) using remote sensing and GIS. ***International Journal of Scientific and Research Publications***, 3(3): 1-10.

Abd Elhamid, A. M.Eltahan, A. M.Mohamed, L. M.and Hamouda, I. A. 2020. Assessment of the two satellite-based precipitation products TRMM and RFE rainfall records using ground based measurements. ***ALEX ENG J***, 59((2)): 1049-1058.

Abdel-Rahman, E.and Ahmed, F. B. 2008. The application of remote sensing techniques to sugarcane (Saccharum spp. hybrid) production: a review of the literature. ***International Journal of Remote Sensing***, 29(13): 3753-3767.

Abdelaziz, H. H.Abdalla, A. A.and AbdelLatif, M. A. 2010. Optimizing the Cropping Pattern in North Darfur State, Sudan: A Study of Dar Elslam District. ***Journal of Applied Sciences Research***, 6(2): 156-164.

Abdelaziz, H.H., Abdalla, A.A. and AbdelLatif, M.A. 2012. Optimizing the cropping mix in North Darfur State, Sudan: A study of Umkdada district. ***Journal of the Saudi Society of Agricultural Sciences***, 11(1): 7-13.

Abdelmalek, M. B.and Nouiri, I. 2020. Study of trends and mapping of drought events in Tunisia and their impacts on agricultural production. ***Science of the Total Environment***, 734: 139311.

Abdul-Jalil, M.and Unruh, J. D. 2013. Land rights under stress in Darfur: A volatile dynamic of the conflict. ***War & Society***, 32(2): 156-181.

Abubakar, G. A.Wang, K.Koko, A. F.Husseini, M. I.Shuka, K. A. M.Deng, J.and Gan, M. 2023. Mapping Maize Cropland and Land Cover in Semi-Arid Region in Northern Nigeria Using Machine Learning and Google Earth Engine. ***Remote Sensing***, 15(11): 2835.

Abubakar, H. B.Newete, S. W.and Scholes, M. C. 2020. Drought characterization and trend detection using the reconnaissance drought index for Setsoto Municipality of the Free State Province of South Africa and the impact on maize yield. ***Water***, 12(11): 2993.

Adam, E.Mutanga, O.Odindi, J.and Abdel-Rahman, E. M. 2014. Land-use/cover classification in a heterogeneous coastal landscape using RapidEye imagery: evaluating the performance of random forest and support vector machines classifiers. ***International Journal of Remote Sensing***, 35(10): 3440-3458.

Adhikari, U.Nejadhashemi, A. P.and Woznicki, S. A. 2015. Climate change and eastern Africa: a review of impact on major crops. ***Food and Energy Security***, 4(2): 110-132.

Adhyani, N.June, T.and Sopaheluwakan, A. 2017. ***Exposure to drought: Duration, severity and intensity (Java, Bali and Nusa Tenggara)***. Paper presented at the IOP conference series: earth and environmental science.

Adnan, S.Ullah, K.Khan, A. H.and Gao, S. 2017. Meteorological impacts on evapotranspiration in different climatic zones of Pakistan. ***Journal of Arid Land***, 9(6): 938-952.

Ageet, S.Fink, A. H.Maranan, M.Diem, J. E.Hartter, J.Ssali, A. L.and Ayabagabo, P. 2022. Validation of Satellite Rainfall Estimates over Equatorial East Africa. ***J Hydrometeorol***, 23(2): 129-151.

Ahmadalipour, A.Moradkhani, H.Castelletti, A.and Magliocca, N. 2019. Future drought risk in Africa: Integrating vulnerability, climate change, and population growth. ***Science of the Total Environment***, 662: 672-686.

Ahmed, A. B.Elmagboul, A.Desougi, M. A.Ali, S. A. M.and Kodeal, G. A. F. 2020. Some Soil physicochemical Characteristics Affected by Land Use Change at El Salaam Locality, South Darfur State, Sudan.

Ahmed, S. M.and Ribbe, L. 2011. Analysis of water footprints of rainfed and irrigated crops in Sudan. ***Journal of Natural Resources and Development***, 1: 20-28.

Ali Ahmed, A. 2008. The Fifth population census in Sudan: A census with a full coverage and a high accuracy. Khartoum: Neelain University, Sudan.

Ali, E.-A. D. M.and Mohamedain, M. S. 2016. Assessment of Desertification at Umm Bayada Basin (Al Maleha Locality North Darfur State-Sudan). ***Int. J. Curr. Microbiol. App. Sci***, 5(5): 94-108.

Altoom, M. B.Adam, E.and Ali, K. A. 2023. Mapping and Monitoring Spatio-Temporal Patterns of Rainfed Agriculture Lands of North Darfur State, Sudan, Using Earth Observation Data. ***Land***, 12(2): 307.

Amani, M.Ghorbanian, A.Ahmadi, S. A.Kakooei, M.Moghimi, A.Mirmazloumi, S. M.Moghaddam, S. H. A.Mahdavi, S.Ghahremanloo, M.and Parsian, S. 2020. Google earth engine cloud computing platform for remote sensing big data applications: A comprehensive review. ***IEEE Journal of Selected Topics in Applied Earth Observations and Remote Sensing***, 13: 5326-5350.

Arias, P.Bellouin, N.Coppola, E.Jones, R.Krinner, G.Marotzke, J.Naik, V.Palmer, M.Plattner, G.-K.and Rogelj, J. 2021. Climate Change 2021: the physical science basis. Contribution of Working Group I to the Sixth Assessment Report of the Intergovernmental Panel on Climate Change; technical summary.

Asadieh, B.and Krakauer, N. Y. 2017. Global change in streamflow extremes under climate change over the 21st century. ***Hydrology and Earth System Sciences***, 21(11): 5863-5874.

Asfaw, A.Simane, B.Hassen, A.and Bantider, A. 2018. Variability and time series trend analysis of rainfall and temperature in northcentral Ethiopia: A case study in Woleka sub-basin. ***Weather and climate extremes***, 19: 29-41.

Asgarian, A.Soffianian, A.and Pourmanafi, S. 2016. Crop type mapping in a highly fragmented and heterogeneous agricultural landscape: A case of central Iran using multi-temporal Landsat 8 imagery. ***Computers and Electronics in Agriculture***, 127: 531-540.

Ashouri, H.Hsu, K.-L.Sorooshian, S.Braithwaite, D. K.Knapp, K. R.Cecil, L. D.Nelson, B. R.and Prat, O. P. 2015. PERSIANN-CDR: Daily precipitation climate data record from multisatellite observations for hydrological and climate studies. ***B Am Meteorol Soc***, 96(1): 69-83.

Atiem, I. A.Siddig, M. S.Hamukwaya, S. L.Ahmed, H. I.Taha, M. M.Ibrahim, S.and Osman, Y. 2022. Assessment of seasonal rainfall drought indices, Nyala City Sudan. ***Agriculture***, 12(7): 1069.

Augustine, D. J. 2010. Spatial versus temporal variation in precipitation in a semiarid ecosystem. ***Landscape ecology***, 25: 913-925.

Ayehu, G. T.Tadesse, T.Gessesse, B.and Dinku, T. 2018. Validation of new satellite rainfall products over the Upper Blue Nile Basin, Ethiopia. ***Atmos Meas Tech***, 11(4): 1921-1936.

Ayugi, B. O.Wen, W.and Chepkemoi, D. 2016. Analysis of spatial and temporal patterns of rainfall variations over Kenya. ***J Environ Earth Sci*** 6(11): 69-83.

Babaousmail, H.Hou, R.Ayugi, B.and Gnitou, G. T. 2019. Evaluation of satellite-based precipitation estimates over Algeria during 1998–2016. ***Journal of Atmospheric and Solar-Terrestrial Physics***, 195: 105139.

Bai, G.Ge, Y.Hussain, W.Baenziger, P. S.and Graef, G. 2016. A multi-sensor system for high throughput field phenotyping in soybean and wheat breeding. ***Computers and Electronics in Agriculture***, 128: 181-192.

Bai, J.Shi, H.Yu, Q.Xie, Z.Li, L.Luo, G.Jin, N.and Li, J. 2019. Satellite-observed vegetation stability in response to changes in climate and total water storage in Central Asia. ***Science of the Total Environment***, 659: 862-871.

Basheer, M.and Elagib, N. A. 2019. Performance of satellite-based and GPCC 7.0 rainfall products in an extremely data-scarce country in the Nile Basin. ***Atmos Res***, 215: 128-140.

Bayissa, Y.Tadesse, T.Demisse, G.and Shiferaw, A. 2017. Evaluation of satellite-based rainfall estimates and application to monitor meteorological drought for the Upper Blue Nile Basin, Ethiopia. ***Remote Sensing***, 9(7): 669.

Beck, H.VAN, D.Levizzani, V.Schellekens, J.Miralles, D. G.Martens, B.and DE, R. 2017. MSWEP: 3-hourly 0.25° global gridded precipitation (1979–2014) by merging gauge, satellite, and reanalysis data. ***HESS***.

Bhuiyan, C.Singh, R.and Kogan, F. 2006. Monitoring drought dynamics in the Aravalli region (India) using different indices based on ground and remote sensing data. ***International Journal of Applied Earth Observation and Geoinformation***, 8(4): 289-302.

Biradar, C. M.Thenkabail, P. S.Noojipady, P.Li, Y.Dheeravath, V.Turral, H.Velpuri, M.Gumma, M. K.Gangalakunta, O. R. P.and Cai, X. L. 2009. A global map of rainfed cropland areas (GMRCA) at the end of last millennium using remote sensing. ***International journal of applied earth observation and geoinformation***, 11(2): 114-129.

Biro, K.Pradhan, B.Buchroithner, M.and Makeschin, F. 2013. Land use/land cover change analysis and its impact on soil properties in the northern part of Gadarif region, Sudan. ***Land Degradation & Development***, 24(1): 90-102.

Bitew, M. M.and Gebremichael, M. 2011. Assessment of satellite rainfall products for streamflow simulation in medium watersheds of the Ethiopian highlands. ***J Hydrol Earth Syst Sc***, 15(4): 1147-1155.

Bofana, J.Zhang, M.Nabil, M.Wu, B.Tian, F.Liu, W.Zeng, H.Zhang, N.Nangombe, S. S.and Cipriano, S. A. 2020. Comparison of different cropland classification methods under diversified agroecological conditions in the Zambezi River Basin. ***Remote Sensing***, 12(13): 2096.

Böhler, J. E.Schaepman, M. E.and Kneubühler, M. 2020. Crop separability from individual and combined airborne imaging spectroscopy and UAV multispectral data. ***Remote Sensing***, 12(8): 1256.

Bontemps, S.Arias, M.Cara, C.Dedieu, G.Guzzonato, E.Hagolle, O.Inglada, J.Matton, N.Morin, D.and Popescu, R. 2015. Building a data set over 12 globally distributed sites to support the development of agriculture monitoring applications with Sentinel-2. ***Remote Sensing***, 7(12): 16062-16090.

Boushaki, F. I.Hsu, K.-L.Sorooshian, S.Park, G.-H.Mahani, S.and Shi, W. 2009. Bias adjustment of satellite precipitation estimation using ground-based measurement: A case study evaluation over the southwestern United States. ***Journal of Hydrometeorology***, 10(5): 1231-1242.

Bradford, J. B.Schlaepfer, D. R.Lauenroth, W. K.Yackulic, C. B.Duniway, M.Hall, S.Jia, G.Jamiyansharav, K.Munson, S. M.and Wilson, S. D. 2017. Future soil moisture and temperature extremes imply expanding suitability for rainfed agriculture in temperate drylands. ***Scientific reports***, 7(1): 1-11.

Brauch, H. G. 2006. Desertification–a new security challenge for the Mediterranean? Policy agenda for recognising and coping with fatal outcomes of global environmental change and potentially violent societal consequences, ***Desertification in the Mediterranean Region. A Security Issue***: 11-85: Springer.

Breiman, L. 2001. Random forests. ***Machine learning***, 45(1): 5-32.

Breiman, L.and Ihaka, R. 1984. ***Nonlinear discriminant analysis via scaling and ACE***: Department of Statistics, University of California Davis One Shields Avenue ….

Brinkhoff, J.Vardanega, J.and Robson, A. J. 2019. Land cover classification of nine perennial crops using sentinel-1 and-2 data. ***Remote Sensing***, 12(1): 96.

Brocca, L.Pellarin, T.Crow, W. T.Ciabatta, L.Massari, C.Ryu, D.Su, C. H.Rüdiger, C.and Kerr, Y. 2016. Rainfall estimation by inverting SMOS soil moisture estimates: A comparison of different methods over Australia. ***J Geophys Res-Atmos***, 121(20): 12,062-012,079.

Bushra, E.-S. E.and Taha, M. O. 2000. A model for the distribution of waters of international rivers among sharing countries. ***Sudan Notes and Records***(4): 159-171.

Camargo, F. F.Sano, E. E.Almeida, C. M.Mura, J. C.and Almeida, T. 2019. A comparative assessment of machine-learning techniques for land use and land cover classification of the Brazilian tropical savanna using ALOS-2/PALSAR-2 polarimetric images. ***Remote Sensing***, 11(13): 1600.

Carella, E.Orusa, T.Viani, A.Meloni, D.Borgogno-Mondino, E.and Orusa, R. 2022. An Integrated, Tentative Remote-Sensing Approach Based on NDVI Entropy to Model Canine Distemper Virus in Wildlife and to Prompt Science-Based Management Policies. ***Animals***, 12(8): 1049.

Cassman, K. G. 1999. Ecological intensification of cereal production systems: yield potential, soil quality, and precision agriculture. ***Proceedings of the National Academy of Sciences***, 96(11): 5952-5959.

Castro, L. M.Miranda, M.and Fernández, B. 2015. Evaluation of TRMM multi-satellite precipitation analysis (TMPA) in a mountainous region of the central Andes range with a Mediterranean climate. ***J Hydrol Res***, 46(1): 89-105.

Cavalcante, R. B. L.Ferreira, D. B. D.Pontes, P. R. M.Tedeschi, R. G.da Costa, C. P. W.and de Souza, E. B. 2020. Evaluation of extreme rainfall indices from CHIRPS precipitation estimates over the Brazilian Amazonia. ***Atmos Res***, 238: 104879.

Chabalala, Y.Adam, E.and Ali, K. A. 2022. Machine Learning Classification of Fused Sentinel-1 and Sentinel-2 Image Data towards Mapping Fruit Plantations in Highly Heterogenous Landscapes. ***Remote Sensing***, 14(11): 2621.

Chabalala, Y. Adam, E. and Ali, K.A. 2023. Exploring the Effect of Balanced and Imbalanced Multi-Class Distribution Data and Sampling Techniques on Fruit-Tree Crop Classification Using Different Machine Learning Classifiers. ***Geomatics***, 3(1): 70-92.

Chang, K.-T.Merghadi, A.Yunus, A. P.Pham, B. T.and Dou, J. 2019. Evaluating scale effects of topographic variables in landslide susceptibility models using GIS-based machine learning techniques. ***Scientific reports***, 9(1): 12296.

Cheema, M. J. M.and Bastiaanssen, W. G. 2012. Local calibration of remotely sensed rainfall from the TRMM satellite for different periods and spatial scales in the Indus Basin. ***Int J Remote Sens***, 33(8): 2603-2627.

Cheeseman, J. 2016. Food security in the face of salinity, drought, climate change, and population growth, ***Halophytes for food security in dry lands***: 111-123: Elsevier.

Chong, L.LIU, H.-j.LU, L.-p.LIU, Z.-r.KONG, F.-c.and ZHANG, X.-l. 2021. Monthly composites from Sentinel-1 and Sentinel-2 images for regional major crop mapping with Google Earth Engine. ***Journal of Integrative Agriculture***, 20(7): 1944-1957.

Choubin, B.Khalighi-Sigaroodi, S.Mishra, A.Goodarzi, M.Shamshirband, S.Ghaljaee, E.and Zhang, F. 2019. A novel bias correction framework of TMPA 3B42 daily precipitation data using similarity matrix/homogeneous conditions. ***Science of the Total Environment***, 694: 133680.

Cohen, J.Cohen, P.West, S. G.and Aiken, L. S. 2013. ***Applied multiple regression/correlation analysis for the behavioral sciences***: Routledge.

Colombo, R.Busetto, L.Meroni, M.Rossini, M.and Panigada, C. 2011. Optical remote sensing of vegetation water content, in hyperspectral indices and image classifications for agriculture and vegetation. ***CRC Press/Taylor and Francis groud USA***:227-244.

Congalton, R. G. 1991. A review of assessing the accuracy of classifications of remotely sensed data. ***Remote sensing of environment***, 37(1): 35-46.

Craparo, A.Van Asten, P. J.Läderach, P.Jassogne, L. T.and Grab, S. 2015. Coffea arabica yields decline in Tanzania due to climate change: Global implications. ***Agricultural and Forest Meteorology***, 207: 1-10.

Cui, J.Zhu, M.Liang, Y.Qin, G.Li, J.and Liu, Y. 2022. Land use/land cover change and their driving factors in the Yellow River Basin of Shandong Province based on google earth Engine from 2000 to 2020. ***ISPRS International Journal of Geo-Information***, 11(3): 163.

Dagne, T. S. 2009. Sudan: The crisis in Darfur and status of the north-south peace agreement: Washington DC ***Congressional Research Service***. 30: 1

De Marinis, P.De Petris, S.Sarvia, F.Manfron, G.Momo, E. J.Orusa, T.Corvino, G.Sali, G.and Borgogno, E. M. 2021. Supporting Pro-Poor Reforms of Agricultural Systems in Eastern DRC (Africa) with Remotely Sensed Data: A Possible Contribution of Spatial Entropy to Interpret Land Management Practices. ***Land***, 10(12): 1368.

Defourny, P.Bontemps, S.Bellemans, N.Cara, C.Dedieu, G.Guzzonato, E.Hagolle, O.Inglada, J.Nicola, L.and Rabaute, T. 2019. Near real-time agriculture monitoring at national scale at parcel

resolution: Performance assessment of the Sen2-Agri automated system in various cropping systems around the world. ***Remote sensing of environment***, 221: 551-568.

Delavarpour, N.Koparan, C.Nowatzki, J.Bajwa, S.and Sun, X. 2021. A technical study on UAV characteristics for precision agriculture applications and associated practical challenges. ***Remote Sensing***, 13(6): 1204.

Dembélé, M.and Zwart, S. J. 2016. Evaluation and comparison of satellite-based rainfall products in Burkina Faso, West Africa. ***Int J Remote Sens***, 37(17): 3995-4014.

Devendra, C. 2012. Rainfed areas and animal agriculture in Asia: the wanting agenda for transforming productivity growth and rural poverty. ***Asian-Australasian journal of animal sciences***, 25(1): 122.

Dezfuli, A. K.Ichoku, C. M.Huffman, G. J.Mohr, K. I.Selker, J. S.Van De Giesen, N.Hochreutener, R.and Annor, F. O. 2017. Validation of IMERG precipitation in Africa. ***Journal of Hydrometeorology***, 18(10): 2817-2825.

Di Paola, F.Casella, D.Dietrich, S.Mugnai, A.Ricciardelli, E.Romano, F.and Sanò, P. 2012. Combined MW-IR Precipitation Evolving Technique (PET) of convective rain fields. ***Natural Hazards and Earth System Sciences***, 12(11): 3557-3570.

Diem, J. E.Hartter, J.Ryan, S. J.and Palace, M. W. 2014. Validation of satellite rainfall products for western Uganda. ***Journal of Hydrometeorology***, 15(5): 2030-2038.

Dinku, T.Ceccato, P.Grover-Kopec, E.Lemma, M.Connor, S. J.and Ropelewski, C. F. 2007. Validation of satellite rainfall products over East Africa's complex topography. ***Int J Remote Sens***, 28(7-8): 1503-1526.

Duhan, D.and Pandey, A. 2013. Statistical analysis of long term spatial and temporal trends of precipitation during 1901–2002 at Madhya Pradesh, India. ***Atmos Res***, 122: 136-149.

Dupree, L. 1977. ***USAID [United States Agency for International Development] and Social Scientists Discuss Afghanistan's Development Prospects***: Am. Univ. Field Staff.

Dutta, D.Kundu, A.Patel, N.Saha, S.and Siddiqui, A. 2015. Assessment of agricultural drought in Rajasthan (India) using remote sensing derived Vegetation Condition Index (VCI) and Standardized Precipitation Index (SPI). ***The Egyptian Journal of Remote Sensing and Space Science***, 18(1): 53-63.

Ebert, E. E.Janowiak, J. E.and Kidd, C. 2007. Comparison of near-real-time precipitation estimates from satellite observations and numerical models. ***B Am Meteorol Soc***, 88(1): 47-+.

Edreira, J. I. R.Guilpart, N.Sadras, V.Cassman, K. G.van Ittersum, M. K.Schils, R. L.and Grassini, P. 2018. Water productivity of rainfed maize and wheat: A local to global perspective. ***Agricultural and forest meteorology***, 259: 364-373.

Eklund, L.Abdi, A.and Islar, M. 2017. From producers to consumers: the challenges and opportunities of agricultural development in Iraqi Kurdistan. ***Land***, 6(2): 44.

El-Amin, K. 2002. Drought and the evolution of well-irrigated Wadi agriculture: implications for sustainable food security systems in Northern Darfur, Sudan.

Elagib, N. A. 2009. Assessment of drought across central Sudan using UNEP dryness ratio. ***Hydrology Research***, 40(5): 481-494.

Elagib, N. A.Al Zayed, I. S.Saad, S. A. G.Mahmood, M. I.Basheer, M.and Fink, A. H. 2021. Debilitating floods in the Sahel are becoming frequent. ***Journal of Hydrology***, 599: 126362.

Elagib, N. A.Khalifa, M.Rahma, A. E.Babker, Z.and Gamaledin, S. I. 2019. Performance of major mechanized rainfed agricultural production in Sudan: Sorghum vulnerability and resilience to climate since 1970. ***Agricultural and Forest Meteorology***, 276: 107640.

Elgali, M. B.Mustafa, R. H.and Bauer, S. 2010. Development of the agricultural crops trade sector of Sudan under the increasing world food prices. ***African Association of Agricultural Economists (AAAE) and 48th Agricultural Economists Association of South Africa (AEASA) Conference, Cape Town, South Africa, September 19-23.***

Elhag, K. M.and Zhang, W. 2018. Monitoring and assessment of drought focused on its impact on sorghum yield over Sudan by using meteorological drought indices for the period 2001–2011. ***Remote Sensing***, 10(8): 1231.

Eze, E.Girma, A.Zenebe, A.Okolo, C. C.Kourouma, J. M.and Negash, E. 2022. Predictors of drought-induced crop yield/losses in two agroecologies of southern Tigray, Northern Ethiopia. ***Scientific Reports***, 12(1): 6284.

Fadul, A. A. 2004. ***Natural resources management for sustainable peace in Darfur***. Paper presented at the Environmental Degradation as a Cause of Conflict in Darfur, conference proceedings.

Faris, S. 2007. The real roots of Darfur. ***Atlantic Monthly***, 299(3): 67.

Felegari, S.Sharifi, A.Moravej, K.Amin, M.Golchin, A.Muzirafuti, A.Tariq, A.and Zhao, N. 2021. Integration of sentinel 1 and sentinel 2 satellite images for crop mapping. ***Applied Sciences***, 11(21): 10104.

Feng, K.Su, X.Zhang, G.Javed, T.and Zhang, Z. 2020. Development of a new integrated hydrological drought index (SRGI) and its application in the Heihe River Basin, China. ***Theoretical and Applied Climatology***, 141: 43-59.

Fenta, A. A.Yasuda, H.Shimizu, K.Ibaraki, Y.Haregeweyn, N.Kawai, T.Belay, A. S.Sultan, D.and Ebabu, K. 2018. Evaluation of satellite rainfall estimates over the Lake Tana basin at the source region of the Blue Nile River. ***Atmos Res***, 212: 43-53.

Field, C. B.and Barros, V. R. 2014. ***Climate change 2014–Impacts, adaptation and vulnerability: Regional aspects***: Cambridge University Press.

Foley, J. A.Ramankutty, N.Brauman, K. A.Cassidy, E. S.Gerber, J. S.Johnston, M.Mueller, N. D.O'Connell, C.Ray, D. K.and West, P. C. 2011. Solutions for a cultivated planet. ***Nature***, 478(7369): 337-342.

Foody, G. M. 2002. Status of land cover classification accuracy assessment. ***Remote sensing of environment***, 80(1): 185-201.

Forkuor, G.Conrad, C.Thiel, M.Zoungrana, B. J.and Tondoh, J. E. 2017. Multiscale remote sensing to map the spatial distribution and extent of cropland in the Sudanian Savanna of West Africa. ***Remote Sensing***, 9(8): 839.

Foster, T.Brozović, N.and Butler, A. 2015. Why well yield matters for managing agricultural drought risk. ***Weather and Climate Extremes***, 10: 11-19.

Frampton, W. J.Dash, J.Watmough, G.and Milton, E. J. 2013. Evaluating the capabilities of Sentinel-2 for quantitative estimation of biophysical variables in vegetation. ***ISPRS journal of photogrammetry and remote sensing***, 82: 83-92.

Friedman, J. H. 2002. Stochastic gradient boosting. ***Computational statistics & data analysis***, 38(4): 367-378.

Fuller, T. D. 1987a. Resettlement as a desertification control measure: A case study in Darfur Region, Sudan—Part I: Review of the problem. ***Agricultural Administration and Extension***, 25(4): 215-234.

Fuller, T.D. 1987b. Resettlement as a desertification control measure: A case study in Darfur Region, Sudan—Part II: Recommendations. ***Agricultural Administration and Extension***, 26(1): 39-55.

Funk, C.Verdin, A.Michaelsen, J.Peterson, P.Pedreros, D.and Husak, G. 2015. A global satellite-assisted precipitation climatology. ***Earth Syst Sci Data***, 7(2): 275-287.

Gadouali, F.and Messouli, M. 2020. Evaluation of multiple satellite-derived rainfall products over Morocco. ***Int J Hydrol Sci Tec***, 10(1): 72-89.

Gbangou, T.Ludwig, F.van Slobbe, E.Greuell, W.and Kranjac-Berisavljevic, G. 2020. Rainfall and dry spell occurrence in Ghana: Trends and seasonal predictions with a dynamical and a statistical model. ***Theoretical and Applied Climatology***, 141: 371-387.

Ge, Y.Bai, G.Stoerger, V.and Schnable, J. C. 2016. Temporal dynamics of maize plant growth, water use, and leaf water content using automated high throughput RGB and hyperspectral imaging. ***Computers and Electronics in Agriculture***, 127: 625-632.

Gebremichael, M.Krajewski, W. F.Morrissey, M. L.Huffman, G. J.and Adler, R. F. 2005. A detailed evaluation of GPCP 1 daily rainfall estimates over the Mississippi River Basin. ***Journal of Applied Meteorology and Climatology***, 44(5): 665-681.

Genuer, R.Poggi, J.-M.and Tuleau-Malot, C. 2015. VSURF: an R package for variable selection using random forests. ***The R Journal***, 7(2): 19-33.

Gilbertson, J. K.and Van Niekerk, A. 2017. Value of dimensionality reduction for crop differentiation with multi-temporal imagery and machine learning. ***Computers and Electronics in Agriculture***, 142: 50-58.

Girma, D. 2021. Evaluation and Bias correction of Tropical Applications of Meteorology using SATellite (TAMSAT) daily rainfall estimates over the data-scarce region of Southern Ethiopia. ***J. Civ. Eng***, 121: 2-7.

Gislason, P. O.Benediktsson, J. A.and Sveinsson, J. R. 2006. Random forests for land cover classification. ***Pattern recognition letters***, 27(4): 294-300.

Gitelson, A. A.Kaufman, Y. J.and Merzlyak, M. N. 1996. Use of a green channel in remote sensing of global vegetation from EOS-MODIS. ***Remote sensing of Environment***, 58(3): 289-298.

Gizaw, M. S.and Gan, T. Y. 2017. Impact of climate change and El Niño episodes on droughts in sub-Saharan Africa. ***Climate Dynamics***, 49(1-2): 665-682.

Godfray, H. C. J.Beddington, J. R.Crute, I. R.Haddad, L.Lawrence, D.Muir, J. F.Pretty, J.Robinson, S.Thomas, S. M.and Toulmin, C. 2010. Food security: the challenge of feeding 9 billion people. ***science***, 327(5967): 812-818.

Gorelick, N.Hancher, M.Dixon, M.Ilyushchenko, S.Thau, D.and Moore, R. 2017. Google Earth Engine: Planetary-scale geospatial analysis for everyone. ***Remote sensing of Environment***, 202: 18-27.

Gourlay, S.Kilic, T.and Lobell, D. 2017. Could the debate be over? errors in farmer-reported production and their implications for the inverse scale-productivity relationship in Uganda. ***Errors in Farmer-Reported Production and Their Implications for the Inverse Scale-Productivity Relationship in Uganda (September 12, 2017). World Bank Policy Research Working Paper***(8192).

Grimes, D.Pardo-Iguzquiza, E.and Bonifacio, R. 1999. Optimal areal rainfall estimation using raingauges and satellite data. ***Journal of hydrology***, 222(1-4): 93-108.

Grist, J. P.and Nicholson, S. E. 2001. A study of the dynamic factors influencing the rainfall variability in the West African Sahel. ***Journal of climate***, 14(7): 1337-1359.

Gwambene, B. 2007. Climate change and variability adaptation strategies and its implication on land resources in Rungwe District, Tanzania. ***A Master of Science Dissertation, University of Dar es Salaam, Dar es Salaam***.

Haile, A. T.Habib, E.and Rientjes, T. 2013. Evaluation of the climate prediction center (CPC) morphing technique (CMORPH) rainfall product on hourly time scales over the source of the Blue Nile River. ***J Hydrol Process***, 27(12): 1829-1839.

Håland, G. 1991. Systems of agricultural production in western Sudan. In: Craig, G.M. (Ed.), The Agriculture of the Sudan. ***Oxford University Press, Oxford:*** 230–251.

Hao, P.Löw, F.and Biradar, C. 2018. Annual cropland mapping using reference Landsat time series—a case study in Central Asia. ***Remote Sensing***, 10(12): 2057.

Hargreaves, G. H.and Samani, Z. A. 1985. Reference crop evapotranspiration from temperature. ***Applied engineering in agriculture***, 1(2): 96-99.

Hasan, H. H.Mohd Razali, S. F.Muhammad, N. S.and Ahmad, A. 2019. Research trends of hydrological drought: A systematic review. ***Water***, 11(11): 2252.

Hasan, H. H.Mohd Razali, S. F.Muhammad, N. S.and Mohamad Hamzah, F. 2021. Assessment of probability distributions and analysis of the minimum storage draft rate in the equatorial region. ***Natural Hazards and Earth System Sciences***, 21(1): 1-19.

Hatfield, J. L.Prueger, J. H.Sauer, T. J.Dold, C.O'Brien, P.and Wacha, K. 2019. Applications of vegetative indices from remote sensing to agriculture: Past and future. ***Inventions***, 4(4): 71.

Hayes, M.Svoboda, M.Wall, N.and Widhalm, M. 2011. The Lincoln declaration on drought indices: universal meteorological drought index recommended. ***Bulletin of the American Meteorological Society***, 92(4): 485-488.

Hedo de Santiago, J.Lucas-Borja, M. E.Wic-Baena, C.Andrés-Abellán, M.and de las Heras, J. 2016. Effects of thinning and induced drought on microbiological soil properties and plant species diversity at dry and semiarid locations. ***Land Degradation & Development***, 27(4): 1151-1162.

Heim Jr, R. R. 2002. A review of twentieth-century drought indices used in the United States. ***Bulletin of the American Meteorological Society***, 83(8): 1149-1166.

Hsu, K. L.Gao, X. G.Sorooshian, S.and Gupta, H. V. 1997. Precipitation estimation from remotely sensed information using artificial neural networks. ***Journal of Applied Meteorology***, 36(9): 1176-1190.

Huete, A.Didan, K.Miura, T.Rodriguez, E. P.Gao, X.and Ferreira, L. G. 2002. Overview of the radiometric and biophysical performance of the MODIS vegetation indices. ***Remote sensing of environment***, 83(1-2): 195-213.

Huete, A. R. 1988. A soil-adjusted vegetation index (SAVI). ***Remote sensing of environment***, 25(3): 295-309.

Huffman, G. J.Adler, R. F.Arkin, P.Chang, A.Ferraro, R.Gruber, A.Janowiak, J.McNab, A.Rudolf, B.and Schneider, U. 1997. The Global Precipitation Climatology Project (GPCP) Combined Precipitation Dataset. ***B Am Meteorol Soc***, 78(1): 5-20.

Huffman, G. J.Bolvin, D. T.Braithwaite, D.Hsu, K.Joyce, R.Xie, P.and Yoo, S.-H. 2015. NASA global precipitation measurement (GPM) integrated multi-satellite retrievals for GPM (IMERG). ***J ATBD***, 4(26): 36-37.

Huffman, G. J.Bolvin, D. T.Nelkin, E. J.Wolff, D. B.Adler, R. F.Gu, G.Hong, Y.Bowman, K. P.and Stocker, E. F. 2007. The TRMM Multisatellite Precipitation Analysis (TMPA): Quasi-global, multiyear, combined-sensor precipitation estimates at fine scales. ***Journal of hydrometeorology***, 8(1): 38-55.

Ibrahim, A. H.Molla, D. D.and Lohani, T. K. 2022. Performance evaluation of satellite-based rainfall estimates for hydrological modeling over Bilate river basin, Ethiopia. ***World Journal of Engineering***. 21(1):1-15.

Ibrahim, F. 1978. Anthropogenic causes of desertification in Western Sudan. ***GeoJournal***, 2(3): 243-254.

Ibrahim, F. N. 1982. The role of women peasants in the process of desertification in Western Sudan. ***GeoJournal***, 6(1): 25-30.

Ibrahim, F.N. 1984. Ecological imbalance in the Republic of the Sudan: with reference to desertification in Darfur, ***Bayreuther Geowissenschaftliche Arbeiten Ed. Bayreuth: Druckhaus Bayreuth Verlagsgesellschaft.6***

Inglada, J.Arias, M.Tardy, B.Hagolle, O.Valero, S.Morin, D.Dedieu, G.Sepulcre, G.Bontemps, S.and Defourny, P. 2015. Assessment of an operational system for crop type map production using high temporal and spatial resolution satellite optical imagery. ***Remote Sensing***, 7(9): 12356-12379.

Inoue, S.Ito, A.and Yonezawa, C. 2020. Mapping Paddy fields in Japan by using a Sentinel-1 SAR time series supplemented by Sentinel-2 images on Google Earth Engine. ***Remote Sensing***, 12(10): 1622.

IPCC, C. C. 2014. Impacts, Adaptation, and Vulnerability. Part A: Global and Sectoral Aspects. Contribution of Working Group II to the Fifth Assessment Report of the Intergovernmental Panel on Climate Change. ***Cambridge University Press, Cambridge, United Kingdom and New York, NY, USA***, 1132.

Islam, K.Jashimuddin, M.Nath, B.and Nath, T. K. 2018. Land use classification and change detection by using multi-temporal remotely sensed imagery: The case of Chunati wildlife sanctuary, Bangladesh. ***The Egyptian Journal of Remote Sensing and Space Science***, 21(1): 37-47.

Jiao, W.Tian, C.Chang, Q.Novick, K. A.and Wang, L. 2019. A new multi-sensor integrated index for drought monitoring. ***Agricultural and forest meteorology***, 268: 74-85.

Jony, R. I.Woodley, A.Raj, A.and Perrin, D. 2018. ***Ensemble classification technique for water detection in satellite images***. Paper presented at the 2018 Digital Image Computing: Techniques and Applications (DICTA).

Jordan, C. F. 1969. Derivation of leaf-area index from quality of light on the forest floor. ***Ecology***, 50(4): 663-666.

Kang, Y.and Özdoğan, M. 2019. Field-level crop yield mapping with Landsat using a hierarchical data assimilation approach. ***Remote sensing of environment***, 228: 144-163.

Kaptué, A. T.Hanan, N. P.Prihodko, L.and Ramirez, J. A. 2015. Spatial and temporal characteristics of rainfall in A frica: S ummary statistics for temporal downscaling. ***Water Resources Research***, 51(4): 2668-2679.

Karamalla-Gaiballa, N.and El-Kafafi, S. 2021. The Impact of Conflicts on Natural Resources–The Case of Sudanese Darfur Region. ***Polish Political Science Yearbook***, 50(1): 1-12.

Karst, I. G.Mank, I.Traoré, I.Sorgho, R.Stückemann, K.-J.Simboro, S.Sié, A.Franke, J.and Sauerborn, R. 2020. Estimating yields of household fields in rural subsistence farming systems to study food security in Burkina Faso. ***Remote Sensing***, 12(11): 1717.

Katiraie-Boroujerdy, P.-S.Asanjan, A. A.Hsu, K.-l.and Sorooshian, S. 2017. Intercomparison of PERSIANN-CDR and TRMM-3B42V7 precipitation estimates at monthly and daily time scales. ***Atmos Res***, 193: 36-49.

Kendall, M. 1975. Rank Correlation Methods, Charles Griffin, London (1975).

Kevane, M.and Gray, L. 2008. Darfur: rainfall and conflict. ***J Environ Res Lett***, 3(3): 034006.

Kganyago, M.Mhangara, P.and Adjorlolo, C. 2021. Estimating crop biophysical parameters using machine learning algorithms and Sentinel-2 imagery. ***Remote Sensing***, 13(21): 4314.

Khanal, S.Kc, K.Fulton, J. P.Shearer, S.and Ozkan, E. 2020. Remote sensing in agriculture—accomplishments, limitations, and opportunities. ***Remote Sensing***, 12(22): 3783.

Kidd, C.and Huffman, G. 2011. Global precipitation measurement. ***Meteorological Applications***, 18(3): 334-353.

Kidd, C.and Levizzani, V. 2022. Satellite rainfall estimation, ***Rainfall***: 135-170: Elsevier.

Kimani, M. W.Hoedjes, J. C. B.and Su, Z. B. 2017. An Assessment of Satellite-Derived Rainfall Products Relative to Ground Observations over East Africa. ***Remote Sensing***, 9(5): 430.

Kimes, D.Markham, B.Tucker, C.and McMurtrey III, J. 1981. Temporal relationships between spectral response and agronomic variables of a corn canopy. ***Remote Sensing of Environment***, 11: 401-411.

Kistner, E.Kellner, O.Andresen, J.Todey, D.and Morton, L. W. 2018. Vulnerability of specialty crops to short-term climatic variability and adaptation strategies in the Midwestern USA. ***Climatic change***, 146: 145-158.

Knapp, A. K.and Smith, M. D. 2001. Variation among biomes in temporal dynamics of aboveground primary production. ***Science***, 291(5503): 481-484.

Kobayashi, N.Tani, H.Wang, X.and Sonobe, R. 2020. Crop classification using spectral indices derived from Sentinel-2A imagery. ***Journal of Information and Telecommunication***, 4(1): 67-90.

Kolecka, N.Ginzler, C.Pazur, R.Price, B.and Verburg, P. H. 2018. Regional scale mapping of grassland mowing frequency with Sentinel-2 time series. ***Remote Sensing***, 10(8): 1221.

Kosari, A.Sharifi, A.Ahmadi, A.and Khoshsima, M. 2020. Remote sensing satellite's attitude control system: rapid performance sizing for passive scan imaging mode. ***Aircraft Engineering and Aerospace Technology***, 92(7): 1073-1083.

Koubi, V. 2019. Sustainable development impacts of climate change and natural disaster. ***Background Paper Prepared for Sustainable Development Outlook***: 1-55.

Kumar, L.and Mutanga, O. 2018. Google Earth Engine applications since inception: Usage, trends, and potential. ***Remote sensing***, 10(10): 1509.

Kumar, S.and Jain, K. 2020. A Multi-Temporal Landsat Data Analysis for Land-use/Land-cover Change in Haridwar Region using Remote Sensing Techniques. ***Procedia Computer Science***, 171: 1184-1193.

Kyere, I.Astor, T.Graß, R.and Wachendorf, M. 2019. Multi-temporal agricultural land-Cover mapping using single-year and multi-year models based on Landsat imagery and IACS data. ***Agronomy***, 9(6): 309.

Laux, P.Jäckel, G.Tingem, R. M.and Kunstmann, H. 2010. Impact of climate change on agricultural productivity under rainfed conditions in Cameroon—A method to improve attainable crop yields by planting date adaptations. ***Agricultural and Forest Meteorology***, 150(9): 1258-1271.

Legates, D. R.and McCabe Jr, G. J. 1999. Evaluating the use of "goodness-of-fit" measures in hydrologic and hydroclimatic model validation. ***Water resources research***, 35(1): 233-241.

Lesk, C.Rowhani, P.and Ramankutty, N. 2016. Influence of extreme weather disasters on global crop production. ***Nature***, 529(7584): 84-87.

Lettenmaier, D. P.Wood, E. F.and Wallis, J. R. 1994. Hydro-climatological trends in the continental United States, 1948-88. ***Journal of Climate***, 7(4): 586-607.

Levi, P. 2010. Digitising the past: The beginning of a new future at the Royal Tropical Institute of The Netherlands. ***Program***, 44(1): 39-47.

Liu, X.Pan, Y.Zhu, X.Yang, T.Bai, J.and Sun, Z. 2018. Drought evolution and its impact on the crop yield in the North China Plain. ***Journal of hydrology***, 564: 984-996.

Liu, X. M.Yang, T. T.Hsu, K. L.Liu, C. M.and Sorooshian, S. 2017. Evaluating the streamflow simulation capability of PERSIANN-CDR daily rainfall products in two river basins on the Tibetan Plateau. ***J Hydrol Earth Syst Sc***, 21(1): 169-181.

Lobell, D. B.Di Tommaso, S.You, C.Djima, I. Y.Burke, M.and Kilic, T. 2019. Sight for sorghums: Comparisons of satellite-and ground-based sorghum yield estimates in Mali. ***Remote Sensing***, 12(1): 100.

Lobell, D. B.Schlenker, W.and Costa-Roberts, J. 2011. Climate trends and global crop production since 1980. ***Science***, 333(6042): 616-620.

Longobardi, A.and Villani, P. 2010. Trend analysis of annual and seasonal rainfall time series in the Mediterranean area. ***International journal of Climatology***, 30(10): 1538-1546.

Lossou, E.Owusu-Prempeh, N.and Agyemang, G. 2019. Monitoring Land Cover changes in the tropical high forests using multi-temporal remote sensing and spatial analysis techniques. ***Remote Sensing Applications: Society and Environment***, 16: 100264.

Loukika, K. N.Keesara, V. R.and Sridhar, V. 2021. Analysis of land use and land cover using machine learning algorithms on google earth engine for Munneru River Basin, India. ***Sustainability***, 13(24): 13758.

Löw, F.Michel, U.Dech, S.and Conrad, C. 2013. Impact of feature selection on the accuracy and spatial uncertainty of per-field crop classification using support vector machines. ***ISPRS journal of photogrammetry and remote sensing***, 85: 102-119.

Lu, X.Wang, L.Pan, M.Kaseke, K. F.and Li, B. 2016. A multi-scale analysis of Namibian rainfall over the recent decade–comparing TMPA satellite estimates and ground observations. ***Journal of Hydrology: Regional Studies***, 8: 59-68.

LUO, H.-x.DAI, S.-p.LI, M.-f.LIU, E.-p.ZHENG, Q.HU, Y.-y.and YI, X.-p. 2020. Comparison of machine learning algorithms for mapping mango plantations based on Gaofen-1 imagery. ***Journal of Integrative Agriculture***, 19(11): 2815-2828.

Madadgar, S.AghaKouchak, A.Farahmand, A.and Davis, S. J. 2017. Probabilistic estimates of drought impacts on agricultural production. ***Geophysical Research Letters***, 44(15): 7799-7807.

Mahalanobis, A.Kumar, B. V.and Sims, S. R. F. 1996. Distance-classifier correlation filters for multiclass target recognition. ***Applied Optics***, 35(17): 3127-3133.

Maidment, R.Grimes, D. I.Allan, R. P.Greatrex, H.Rojas, O.and Leo, O. 2013. Evaluation of satellite-based and model re-analysis rainfall estimates for Uganda. ***Meteorological Applications***, 20(3): 308-317.

Maidment, R. I.Grimes, D.Allan, R. P.Tarnavsky, E.Stringer, M.Hewison, T.Roebeling, R.and Black, E. 2014. The 30 year TAMSAT African rainfall climatology and time series (TARCAT) data set. ***Journal of Geophysical Research: Atmospheres***, 119(18): 10,619-610,644.

Maidment, R. I.Grimes, D.Black, E.Tarnavsky, E.Young, M.Greatrex, H.Allan, R. P.Stein, T.Nkonde, E.and Senkunda, S. 2017. A new, long-term daily satellite-based rainfall dataset for operational monitoring in Africa. ***Scientific data***, 4(1): 1-19.

Malenovský, Z.Rott, H.Cihlar, J.Schaepman, M. E.García-Santos, G.Fernandes, R.and Berger, M. 2012. Sentinels for science: Potential of Sentinel-1,-2, and-3 missions for scientific observations of ocean, cryosphere, and land. ***Remote Sensing of environment***, 120: 91-101.

Mann, H. B. 1945. Nonparametric tests against trend. ***Econometrica: Journal of the econometric society***: 245-259.

Marini, G.Fontana, N.and Mishra, A. K. 2019a. Investigating drought in Apulia region, Italy using SPI and RDI. ***Theoretical and applied climatology***, 137: 383-397.

Marini, G., Fontana, N. and Mishra, A.K. 2019b. Investigating drought in Apulia region, Italy using SPI and RDI. ***Theoretical and applied climatology***, 137(1): 383-397.

Mashala, M. J.Dube, T.Mudereri, B. T.Ayisi, K. K.and Ramudzuli, M. R. 2023. A Systematic Review on Advancements in Remote Sensing for Assessing and Monitoring Land Use and Land Cover Changes Impacts on Surface Water Resources in Semi-Arid Tropical Environments. ***Remote Sensing***, 15(16): 3926.

Masupha, T. E.and Moeletsi, M. E. 2018. Analysis of potential future droughts limiting maize production, in the Luvuvhu River catchment area, South Africa. ***Physics and Chemistry of the Earth, Parts A/B/C***, 105: 44-51.

Maxwell, A. E.Warner, T. A.and Fang, F. 2018. Implementation of machine-learning classification in remote sensing: An applied review. ***International journal of remote sensing***, 39(9): 2784-2817.

Mazarire, T. T.Ratshiedana, P. E.Nyamugama, A.Adam, E.and Chirima, G. 2020. Exploring machine learning algorithms for mapping crop types in a heterogeneous agriculture landscape using Sentinel-2 data. A case study of Free State Province, South Africa. ***South African Journal of Geomatics***, 9(2): 333-347.

McCollum, J. R.Gruber, A.and Ba, M. B. 2000. Discrepancy between gauges and satellite estimates of rainfall in equatorial Africa. ***Journal of Applied Meteorology***, 39(5): 666-679.

McKee, T. B.Doesken, N. J.and Kleist, J. 1993. ***The relationship of drought frequency and duration to time scales***. Paper presented at the Proceedings of the 8th Conference on Applied Climatology.

Mekonnen, K.Velpuri, N. M.Leh, M.Akpoti, K.Owusu, A.Tinonetsana, P.Hamouda, T.Ghansah, B.Paranamana, T. P.and Munzimi, Y. 2023. Accuracy of satellite and reanalysis rainfall estimates over Africa: A multi-scale assessment of eight products for continental applications. ***Journal of Hydrology: Regional Studies***, 49: 101514.

Melaas, E. K.Friedl, M. A.and Zhu, Z. 2013. Detecting interannual variation in deciduous broadleaf forest phenology using Landsat TM/ETM+ data. ***Remote Sensing of Environment***, 132: 176-185.

Memorandum, S. C. E. 2015. *Sudan Country Economic Memorandum*: Realizing the Potential for Diversified Development. World Bank Group.

Mengistu, A. G.Tesfuhuney, W. A.Woyessa, Y. E.and van Rensburg, L. D. 2020. Analysis of the spatio-temporal variability of precipitation and drought intensity in an arid catchment in South Africa. ***Climate***, 8(6): 70.

Merabti, A.Meddi, M.Martins, D. S.and Pereira, L. S. 2018. Comparing SPI and RDI applied at local scale as influenced by climate. ***Water resources management***, 32(3): 1071-1085.

Meza, I.Rezaei, E. E.Siebert, S.Ghazaryan, G.Nouri, H.Dubovyk, O.Gerdener, H.Herbert, C.Kusche, J.and Popat, E. 2021. Drought risk for agricultural systems in South Africa: Drivers, spatial patterns,

and implications for drought risk management. ***Science of the Total Environment***, 799: 149505.

Mirzabaev, A.Sakketa, T.Sylla, M. B.Dimobe, K.Sanfo, S.Admassie, A.Abebaw, D.Coulibaly, O. N.Adamou, R.and Ibrahim, B. 2021. Land, Climate, Energy, Agriculture and Development in the Sahel: Synthesis paper of case studies under the Sudano-Sahelian Initiative for Regional Development, Jobs, and Food Security. **University of Bonn, Center for Development Research (ZEF), Bonn: 204**

Mohammed, A. J.and Inoue, M. 2013. Forest-dependent communities' livelihood in decentralized forest governance policy epoch: case study from West Shoa zone, Ethiopia. ***Journal of Natural Resources Policy Research***, 5(1): 49-66.

Mohmmed, A.Zhang, K.Kabenge, M.Keesstra, S.Cerdà, A.Reuben, M.Elbashier, M. M.Dalson, T.and Ali, A. A. 2018. Analysis of drought and vulnerability in the North Darfur region of Sudan. ***Land degradation & development***, 29(12): 4424-4438.

Molden, D.Vithanage, M.De Fraiture, C.Faures, J.Gordon, L.Molle, F.and Peden, D. 2011. 4.21-Water availability and its use in agriculture. ***Treatise on Water Science. Elsevier, Oxford***: 707-732.

Muchow, R. C.and Bellamy, J. A. 1991. ***Climatic Risk in Crop Production: Models and Management for the Semiarid Tropics and Subtropics: Proceedings of the International Symposium on Climatic Risk in Crop Production: Models and Management for the Semiarid Tropics and Subtropics Held in Brisbane, Australia, 2-6 July, 1990***: CAB international.

Muthoni, F. K.Odongo, V. O.Ochieng, J.Mugalavai, E. M.Mourice, S. K.Hoesche-Zeledon, I.Mwila, M.and Bekunda, M. 2019. Long-term spatial-temporal trends and variability of rainfall over Eastern and Southern Africa. ***Theoretical and Applied Climatology***, 137: 1869-1882.

Nababa, I. I.Symeonakis, E.Koukoulas, S.Higginbottom, T. P.Cavan, G.and Marsden, S. 2020. Land cover dynamics and mangrove degradation in the Niger Delta region. ***Remote Sensing***, 12(21): 3619.

Nakalembe, C.Becker-Reshef, I.Bonifacio, R.Hu, G.Humber, M. L.Justice, C. J.Keniston, J.Mwangi, K.Rembold, F.and Shukla, S. 2021. A review of satellite-based global agricultural monitoring systems available for Africa. ***Global Food Security***, 29: 100543.

Nash, J. E.and Sutcliffe, J. V. 1970. River flow forecasting through conceptual models part I—A discussion of principles. ***Journal of hydrology***, 10(3): 282-290.

Ngcamu, B. S.and Chari, F. 2020. Drought influences on food insecurity in Africa: A Systematic literature review. ***International Journal of Environmental Research and Public Health***, 17(16): 5897.

Nitze, I.Schulthess, U.and Asche, H. 2012. Comparison of machine learning algorithms random forest, artificial neural network and support vector machine to maximum likelihood for supervised crop type classification. ***Proceedings of the 4th GEOBIA, Rio de Janeiro, Brazil***, 79: 3540.

Noureldeen, N.Mao, K.Mohmmed, A.Yuan, Z.and Yang, Y. 2020. Spatiotemporal drought assessment over sahelian countries from 1985 to 2015. ***Journal of Meteorological Research***, 34(4): 760-774.

Novella, N. S.and Thiaw, W. M. 2013. African rainfall climatology version 2 for famine early warning systems. ***JAMC***, 52(3): 588-606.

Ochieng, J.Kirimi, L.and Mathenge, M. 2016. Effects of climate variability and change on agricultural production: The case of small scale farmers in Kenya. ***NJAS: Wageningen Journal of Life Sciences***, 77(1): 71-78.

Omonge, P.Feigl, M.Olang, L.Schulz, K.and Herrnegger, M. 2022. Evaluation of satellite precipitation products for water allocation studies in the Sio-Malaba-Malakisi River Basin of East Africa. ***Journal of Hydrology: Regional Studies***, 39: 100983.

Organization, W. M. 2017. WMO guidelines on the calculation of climate normals: World Meteorological Organization Geneva, Switzerland.

Orusa, T.and Borgogno Mondino, E. 2021. Exploring Short-term climate change effects on rangelands and broad-leaved forests by free satellite data in Aosta Valley (Northwest Italy). ***Climate***, 9(3): 47.

Orusa, T.Orusa, R.Viani, A.Carella, E.and Borgogno Mondino, E. 2020. Geomatics and EO data to support wildlife diseases assessment at landscape level: A pilot experience to map infectious keratoconjunctivitis in chamois and phenological trends in Aosta Valley (NW Italy). ***Remote Sensing***, 12(21): 3542.

Osman, A. M. K. O. 2012. Agricultural change, land and violence: An examination of the region of Darfur, Sudan. (***PhD thesis, Tufts University***).

Osman, A. 2017. Climate Change and Drylands Farming in Sudan: Trend, Impact and Adaptation. ***UK Journal of Natural Resources and Environmental Studies Special Issue Oct***, 2017: 1-10.

Osman, A. K. 2007. Community based seed supply in Sudan. ***LEISA-LEUSDEN-***, 23(2): 18.

Osman, A. M. K.and Cohen, M. J. 2014. We No Longer Share the Land: Agricultural change, land, and violence in Darfur. Policy & Practice, ***Oxfam International***

Osman, A. M. K.Young, H.Houser, R. F.and Coates, J. C. 2013. Agricultural change, land, and violence in protracted political crisis. ***An examination of Darfur. Oxfam America research backgrounder series. Oxfam America, Boston***.

Osman, Y. Z.and Shamseldin, A. Y. 2002. Qualitative rainfall prediction models for central and southern Sudan using El Niño–Southern Oscillation and Indian Ocean sea surface temperature indices. ***Int J Climatol INT J CLIMATOL***, 22(15): 1861-1878.

Ouzemou, J.-E.El Harti, A.Lhissou, R.El Moujahid, A.Bouch, N.El Ouazzani, R.Bachaoui, E. M.and El Ghmari, A. 2018. Crop type mapping from pansharpened Landsat 8 NDVI data: A case of a highly fragmented and intensive agricultural system. ***Remote Sensing Applications: Society and Environment***, 11: 94-103.

Ozdogan, M. 2010. The spatial distribution of crop types from MODIS data: Temporal unmixing using Independent Component Analysis. ***Remote Sensing of Environment***, 114(6): 1190-1204.

Paliwal, A.and Jain, M. 2020. The accuracy of self-reported crop yield estimates and their ability to train remote sensing algorithms. ***Frontiers in Sustainable Food Systems***, 4: 25–35.

Palmer, W. 1965. Meteorological drought. US Weather Bureau Research Paper 45, 58 pp.

Paredes Trejo, F. J.Alves Barbosa, H.Peñaloza-Murillo, M. A.Moreno, M. A.and Farias, A. 2016. Intercomparison of improved satellite rainfall estimation with CHIRPS gridded product and rain gauge data over Venezuela. ***Atmosfera***, 29(4): 323-342.

Pasternak, M.and Pawluszek-Filipiak, K. 2022. The evaluation of spectral vegetation indexes and redundancy reduction on the accuracy of crop type detection. ***Applied Sciences***, 12(10): 5067.

Peña-Gallardo, M.Vicente-Serrano, S. M.Quiring, S.Svoboda, M.Hannaford, J.Tomas-Burguera, M.Martín-Hernández, N.Domínguez-Castro, F.and El Kenawy, A. 2019. Response of crop yield to different time-scales of drought in the United States: Spatio-temporal patterns and climatic and environmental drivers. ***Agricultural and Forest Meteorology***, 264: 40-55.

Phalan, B.Balmford, A.Green, R. E.and Scharlemann, J. P. 2011. Minimising the harm to biodiversity of producing more food globally. ***Food Policy***, 36: S62-S71.

Pierre, C.Bergametti, G.Marticorena, B.Mougin, E.Lebel, T.and Ali, A. 2011. Pluriannual comparisons of satellite-based rainfall products over the Sahelian belt for seasonal vegetation modeling. ***Journal of Geophysical Research: Atmospheres***, 116(D18).

Pimple, U.Simonetti, D.Sitthi, A.Pungkul, S.Leadprathom, K.Skupek, H.Som-Ard, J.Gond, V.and Towprayoon, S. 2018. Google earth engine based three decadal landsat imagery analysis for mapping of mangrove forests and its surroundings in the trat province of Thailand. ***Journal of Computer and Communications***, 6, 247-264.

Praticò, S.Solano, F.Di Fazio, S.and Modica, G. 2021. Machine learning classification of mediterranean forest habitats in google earth engine based on seasonal sentinel-2 time-series and input image composition optimisation. ***Remote Sensing***, 13(4): 586.

Pretty, J. N.Williams, S.and Toulmin, C. 2012. ***Sustainable intensification: increasing productivity in African food and agricultural systems***: Routledge.

Puissant, A.Rougier, S.and Stumpf, A. 2014. Object-oriented mapping of urban trees using Random Forest classifiers. ***International Journal of Applied Earth Observation and Geoinformation***, 26: 235-245.

Qader, S. H.Dash, J.Alegana, V. A.Khwarahm, N. R.Tatem, A. J.and Atkinson, P. M. 2021. The role of earth observation in achieving sustainable agricultural production in arid and semi-arid regions of the world. ***Remote Sensing***, 13(17): 3382.

Qader, S. H.Utazi, C. E.Priyatikanto, R.Najmaddin, P.Hama-Ali, E. O.Khwarahm, N. R.Tatem, A. J.and Dash, J. 2023. Exploring the use of Sentinel-2 datasets and environmental variables to model wheat crop yield in smallholder arid and semi-arid farming systems. ***Science of The Total Environment***, 869: 161716.

Qian, Y.Zhou, W.Yan, J.Li, W.and Han, L. 2014. Comparing machine learning classifiers for object-based land cover classification using very high resolution imagery. ***Remote Sensing***, 7(1): 153-168.

Rao, P.Zhou, W.Bhattarai, N.Srivastava, A. K.Singh, B.Poonia, S.Lobell, D. B.and Jain, M. 2021. Using Sentinel-1, Sentinel-2, and Planet imagery to map crop type of smallholder farms. ***Remote Sensing***, 13(10): 1870.

Ray, D. K.Ramankutty, N.Mueller, N. D.West, P. C.and Foley, J. A. 2012. Recent patterns of crop yield growth and stagnation. ***Nature communications***, 3(1): 1293.

Raziei, T.Saghafian, B.Paulo, A. A.Pereira, L. S.and Bordi, I. 2009. Spatial patterns and temporal variability of drought in western Iran. ***Water resources management***, 23(3): 439-455.

Reddy, V. R.and Syme, G. J. 2014. ***Integrated assessment of scale impacts of watershed intervention: assessing hydrogeological and bio-physical influences on livelihoods***: Elsevier.

Rembold, F.Meroni, M.Urbano, F.Csak, G.Kerdiles, H.Perez-Hoyos, A.Lemoine, G.Leo, O.and Negre, T. 2019. ASAP: A new global early warning system to detect anomaly hot spots of agricultural production for food security analysis. ***Agricultural systems***, 168: 247-257.

Rhee, J.Im, J.and Carbone, G. J. 2010. Monitoring agricultural drought for arid and humid regions using multi-sensor remote sensing data. ***Remote Sensing of environment***, 114(12): 2875-2887.

Richardson, A. J.and Wiegand, C. 1977. Distinguishing vegetation from soil background information. ***Photogrammetric engineering and remote sensing***, 43(12): 1541-1552.

Rockström, J.Barron, J.and Fox, P. 2003. Water productivity in rain-fed agriculture: challenges and opportunities for smallholder farmers in drought-prone tropical agroecosystems. ***Water productivity in agriculture: Limits and opportunities for improvement***: 145-162.

Rockström, J.Karlberg, L.Wani, S. P.Barron, J.Hatibu, N.Oweis, T.Bruggeman, A.Farahani, J.and Qiang, Z. 2010. Managing water in rainfed agriculture—the need for a paradigm shift. ***Agricultural Water Management***, 97(4): 543-550.

Rodriguez-Galiano, V. F.Ghimire, B.Rogan, J.Chica-Olmo, M.and Rigol-Sanchez, J. P. 2012. An assessment of the effectiveness of a random forest classifier for land-cover classification. ***ISPRS journal of photogrammetry and remote sensing***, 67: 93-104.

Rouse, J. W.Haas, R. H.Schell, J. A.and Deering, D. W. 1974. Monitoring vegetation systems in the Great Plains with ERTS. ***NASA Spec. Publ***, 351(1): 309.

Roushdi, M. 2022. Spatio-Temporal Assessment of Satellite Estimates and Gauge-Based Rainfall Products in Northern Part of Egypt. ***J. Clim***, 10(9): 134.

Roy, D.and Dikshit, O. 1994. Investigation of image resampling effects upon the textural information content of a high spatial resolution remotely sensed image. ***TitleREMOTE SENSING***, 15(5): 1123-1130.

Rwanga, S. S.and Ndambuki, J. M. 2017. Accuracy assessment of land use/land cover classification using remote sensing and GIS. ***International Journal of Geosciences***, 8(04): 611.

Sabzchi-Dehkharghani, H.Nazemi, A. H.Sadraddini, A. A.Majnooni-Heris, A.and Biswas, A. 2021. Recognition of different yield potentials among rain-fed wheat fields before harvest using remote sensing. ***Agricultural Water Management***, 245: 106611.

Sahajpal, R.Fontana, L.Lafluf, P.Leale, G.Puricelli, E.O'Neill, D.Hosseini, M.Varela, M.and Reshef, I. 2020. ***Using machine-learning models for field-scale crop yield and condition modeling in***

Argentina. Paper presented at the XII Congreso de AgroInformática (CAI 2020)-JAIIO 49 (Modalidad virtual).

Sánchez-Espinosa, A.and Schröder, C. 2019. Land use and land cover mapping in wetlands one step closer to the ground: Sentinel-2 versus landsat 8. ***Journal of Environmental Management***, 247: 484-498.

Sanogo, S.Fink, A. H.Omotosho, J. A.Ba, A.Redl, R.and Ermert, V. 2015. Spatio-temporal characteristics of the recent rainfall recovery in West Africa. ***Int J Climatol*** 35(15): 4589-4605.

Sapkota, T. B.Jat, M.Jat, R.Kapoor, P.and Stirling, C. 2016. Yield estimation of food and non-food crops in smallholder production systems. ***Methods for measuring greenhouse gas balances and evaluating mitigation options in smallholder agriculture***: 163-174.

Sayed, M. A.and Abdala, B. 2013. Sudan environmental and climate change assessment. ***International Fund for Agricultural Development: Rome, Italy***.

Schaefer, M.and Thinh, N. X. 2019. Evaluation of land cover change and agricultural protection sites: a GIS and remote sensing approach for Ho chi minh city, vietnam. ***Heliyon***, 5(5): e01773.

Schimmer, R. 2008. Tracking the genocide in Darfur: population displacement as recorded by remote sensing: ***Genocide Studies Working Paper. Yale University, 36***

Segarra, J.Buchaillot, M. L.Araus, J. L.and Kefauver, S. C. 2020. Remote sensing for precision agriculture: Sentinel-2 improved features and applications. ***Agronomy***, 10(5): 641.

Selby, J.and Hoffmann, C. 2014. Beyond scarcity: rethinking water, climate change and conflict in the Sudans. ***Global Environmental Change***, 29: 360-370.

Sen, P. K. 1968. Estimates of the regression coefficient based on Kendall's tau. ***Journal of the American statistical association***, 63(324): 1379-1389.

Shaharum, N. S. N.Shafri, H. Z. M.Ghani, W. A. W. A. K.Samsatli, S.Al-Habshi, M. M. A.and Yusuf, B. 2020. Oil palm mapping over Peninsular Malaysia using Google Earth Engine and machine learning algorithms. ***Remote Sensing Applications: Society and Environment***, 17: 100287.

Shelestov, A.Lavreniuk, M.Kussul, N.Novikov, A.and Skakun, S. 2017. Exploring Google Earth Engine platform for big data processing: Classification of multi-temporal satellite imagery for crop mapping. ***frontiers in Earth Science***, 5 : 1–10.

Shetty, S. 2019. Analysis of machine learning classifiers for LULC classification on Google Earth Engine. (Master's thesis), University of Twente, Enschede, The Netherlands: 1–65.

Siddig, K. 2010. Macroeconomy and agriculture in Sudan: Analysis of trade policies, external shocks, and economic bans in a computable general equilibrium approach. Available at SSRN 1684084.

Siddig, K; Elagra, S; Grethe, H; Mubarak, A. 2018. A post-separation social accounting matrix for the Sudan, Humboldt Universität zu Berlin, Faculty of Life Sciences, Department of Agricultural Economics, Working Paper, Berlin,92

Siddig, K.Stepanyan, D.Wiebelt, M.Grethe, H.and Zhu, T. 2020a. Climate change and agriculture in the Sudan: Impact pathways beyond changes in mean rainfall and temperature. ***Ecological Economics***, 169: 106566.

Siddig, K.Stepanyan, D.Wiebelt, M.Grethe, H.and Zhu, T. J. 2020b. Climate change and agriculture in the Sudan: Impact pathways beyond changes in mean rainfall and temperature. ***J Ecol Econ***, 169: 106566.

Singh, A. 1989. Review article digital change detection techniques using remotely-sensed data. ***International journal of remote sensing***, 10(6): 989-1003.

Sinha, R.Quirós, J. J.Sankaran, S.and Khot, L. R. 2022. High resolution aerial photogrammetry based 3D mapping of fruit crop canopies for precision inputs management. ***Information Processing in Agriculture***, 9(1): 11-23.

SIRDAŞ, S.and Sen, Z. 2003. Spatio-temporal drought analysis in the Trakya region, Turkey. ***Hydrological Sciences Journal***, 48(5): 809-820.

Sohoulande, C. D.Stone, K.Szogi, A.and Bauer, P. 2019. An investigation of seasonal precipitation patterns for rainfed agriculture in the Southeastern region of the United States. ***Agricultural Water Management***, 223: 105728.

Sonobe, R.Tani, H.Wang, X.Kobayashi, N.and Shimamura, H. 2014. Parameter tuning in the support vector machine and random forest and their performances in cross-and same-year crop classification using TerraSAR-X. ***International Journal of Remote Sensing***, 35(23): 7898-7909.

Sothe, C.Almeida, C. M. d.Liesenberg, V.and Schimalski, M. B. 2017. Evaluating Sentinel-2 and Landsat-8 data to map sucessional forest stages in a subtropical forest in Southern Brazil. ***Remote Sensing***, 9(8): 838.

Stillman, S.Ninneman, J.Zeng, X.Franz, T.Scott, R. L.Shuttleworth, W. J.and Cummins, K. 2014. Summer soil moisture spatiotemporal variability in southeastern Arizona. ***Journal of Hydrometeorology***, 15(4): 1473-1485.

Su, J.Lü, H.Wang, J.Sadeghi, A. M.and Zhu, Y. 2017. Evaluating the applicability of four latest satellite–gauge combined precipitation estimates for extreme precipitation and streamflow predictions over the upper Yellow River basins in China. ***Remote Sensing***, 9(11): 1176.

Sujud, L.Jaafar, H.Hassan, M. A. H.and Zurayk, R. 2021. Cannabis detection from optical and RADAR data fusion: A comparative analysis of the SMILE machine learning algorithms in Google Earth Engine. ***Remote Sensing Applications: Society and Environment***, 24: 100639.

Sungmin, O.Foelsche, U.Kirchengast, G.Fuchsberger, J.Tan, J.and Petersen, W. A. 2017. Evaluation of GPM IMERG Early, Late, and Final rainfall estimates using WegenerNet gauge data in southeastern Austria. ***J Hydrol Earth Syst Sc***, 21(12): 6559-6572.

Svoboda, M.and Fuchs, B. 2016. Handbook of drought indicators and indices. ***Drought and water crises: Integrating science, management, and policy***: 155-208.

Svoboda, M.Hayes, M.and Wood, D. 2012. Standardized precipitation index in (Geneva: WMO): user guide:ISBN 978-92-63-11091-6

Tarnavsky, E.Grimes, D.Maidment, R.Black, E.Allan, R. P.Stringer, M.Chadwick, R.and Kayitakire, F. 2014. Extension of the TAMSAT satellite-based rainfall monitoring over Africa and from 1983 to present. ***Journal of Applied Meteorology and Climatology***, 53(12): 2805-2822.

Taye, M.Mengistu, D.and Sahlu, D. 2023. Performance evaluation of multiple satellite rainfall data sets in central highlands of Abbay Basin, Ethiopia. ***Eur J Remote Sens***, 56(1): 2233686.

Teklu, T.Von Braun, J.and Zaki, E. 1992. Drought and famine relationships in Sudan: Policy implications. ***Food and Nutrition Bulletin***, 14(2): 1-3.

Thenkabail, P. S.Smith, R. B.and De Pauw, E. 2000. Hyperspectral vegetation indices and their relationships with agricultural crop characteristics. ***Remote sensing of Environment***, 71(2): 158-182.

Thyagharajan, K.and Vignesh, T. 2019. Soft computing techniques for land use and land cover monitoring with multispectral remote sensing images: a review. ***Archives of Computational Methods in Engineering***, 26(2): 275-301.

Tigkas, D.Vangelis, H.and Tsakiris, G. 2016. Introducing a modified reconnaissance drought index (RDIe) incorporating effective precipitation. ***Procedia Engineering***, 162: 332-339.

Toté, C.Patricio, D.Boogaard, H.Van der Wijngaart, R.Tarnavsky, E.and Funk, C. 2015. Evaluation of satellite rainfall estimates for drought and flood monitoring in Mozambique. ***Remote Sensing***, 7(2): 1758-1776.

Tran, K. H.Zhang, H. K.McMaine, J. T.Zhang, X.and Luo, D. 2022. 10 m crop type mapping using Sentinel-2 reflectance and 30 m cropland data layer product. ***International Journal of Applied Earth Observation and Geoinformation***, 107: 102692.

Tsakiris, G.Nalbantis, I.Pangalou, D.Tigkas, D.and Vangelis, H. 2008. ***Drought meteorological monitoring network design for the reconnaissance drought index (RDI)***. Paper presented at the Proceedings of the 1st International Conference “Drought management: scientific and technological innovations”. Zaragoza, Spain: option Méditerranéennes, series A.

Tsoumakas, G.Partalas, I.and Vlahavas, I. 2009. An ensemble pruning primer, ***Applications of supervised and unsupervised ensemble methods***: 1-13: Springer.

Tubiello, F. N.Salvatore, M.Rossi, S.Ferrara, A.Fitton, N.and Smith, P. 2013. The FAOSTAT database of greenhouse gas emissions from agriculture. ***Environmental Research Letters***, 8(1): 015009.

Twongyirwe, R.Mfitumukiza, D.Barasa, B.Naggayi, B. R.Odongo, H.Nyakato, V.and Mutoni, G. 2019. Perceived effects of drought on household food security in South-western Uganda: Coping responses and determinants. ***Weather and Climate Extremes***, 24: 100201.

Usman, M.Nichol, J. E.Ibrahim, A. T.and Buba, L. F. 2018. A spatio-temporal analysis of trends in rainfall from long term satellite rainfall products in the Sudano Sahelian zone of Nigeria. ***Agric For Meteorol***, 260: 273-286.

Vangelis, H.Tigkas, D.and Tsakiris, G. 2013. The effect of PET method on Reconnaissance Drought Index (RDI) calculation. ***Journal of Arid Environments***, 88: 130-140.

Verikas, A.Gelzinis, A.and Bacauskiene, M. 2011. Mining data with random forests: A survey and results of new tests. ***Pattern recognition***, 44(2): 330-349.

Vuolo, F.Neuwirth, M.Immitzer, M.Atzberger, C.and Ng, W.-T. 2018. How much does multi-temporal Sentinel-2 data improve crop type classification? ***International journal of applied earth observation and geoinformation***, 72: 122-130.

Waithaka, M.Nelson, G. C.Thomas, T. S.and Kyotalimye, M. 2013. ***East African agriculture and climate change: A comprehensive analysis***: Washington, DC: International Food Policy Research Institute (IFPRI), 76: 4

Waldner, F.De Abelleyra, D.Verón, S. R.Zhang, M.Wu, B.Plotnikov, D.Bartalev, S.Lavreniuk, M.Skakun, S.and Kussul, N. 2016. Towards a set of agrosystem-specific cropland mapping methods to address the global cropland diversity. ***International Journal of Remote Sensing***, 37(14): 3196-3231.

Wani, S. P.Sreedevi, T.Rockström, J.and Ramakrishna, Y. 2009. Rainfed agriculture-past trends and future prospects, ***Rainfed agriculture: Unlocking the potential***: 1-35: CABI Wallingford UK.

Wedajo, G. K.Muleta, M. K.and Awoke, B. G. 2021. Performance evaluation of multiple satellite rainfall products for Dhidhessa River Basin (DRB), Ethiopia. ***Atmos Meas Tech***, 14(3): 2299-2316.

WG III, I. 2007. Working Group III Fourth Assessment Report. ***http://www. mnp. nl/ipcc/pages_media/AR4-chapters. html***.

Wu, Y.Zhang, Z.Huang, Y.Jin, Q.Chen, X.and Chang, J. 2019. Evaluation of the GPM IMERG v5 and TRMM 3B42 v7 precipitation products in the Yangtze River basin, China. ***Water***, 11(7): 1459.

Xie, G.and Niculescu, S. 2022. Mapping crop types using sentinel-2 data machine learning and monitoring crop phenology with sentinel-1 backscatter time series in pays de Brest, Brittany, France. ***Remote Sensing***, 14(18): 4437.

Xie, P.and Arkin, P. A. 1998. Global monthly precipitation estimates from satellite-observed outgoing longwave radiation. ***Journal of Climate***, 11(2): 137-164.

Xiong, J.Thenkabail, P. S.Tilton, J. C.Gumma, M. K.Teluguntla, P.Oliphant, A.Congalton, R. G.Yadav, K.and Gorelick, N. 2017. Nominal 30-m cropland extent map of continental Africa by integrating pixel-based and object-based algorithms using Sentinel-2 and Landsat-8 data on Google Earth Engine. ***Remote Sensing***, 9(10): 1065.

Xue, J.and Su, B. 2017. Significant remote sensing vegetation indices: A review of developments and applications. ***Journal of sensors***, , 2017(1), 1353691

Yan, H.Xiao, X.Huang, H.Liu, J.Chen, J.and Bai, X. 2014. Multiple cropping intensity in China derived from agro-meteorological observations and MODIS data. ***Chinese Geographical Science***, 24: 205-219.

Yang, X.Mustard, J. F.Tang, J.and Xu, H. 2012. Regional-scale phenology modeling based on meteorological records and remote sensing observations. ***Journal of Geophysical Research: Biogeosciences***, 117: 03029

Yao, N.Li, Y.Lei, T.and Peng, L. 2018. Drought evolution, severity and trends in mainland China over 1961–2013. ***Science of the Total Environment***, 616: 73-89.

Yin, H.Prishchepov, A. V.Kuemmerle, T.Bleyhl, B.Buchner, J.and Radeloff, V. C. 2018. Mapping agricultural land abandonment from spatial and temporal segmentation of Landsat time series. ***Remote sensing of environment***, 210: 12-24.

Yong, B.Chen, B.Gourley, J. J.Ren, L.Hong, Y.Chen, X.Wang, W.Chen, S.and Gong, L. 2014. Intercomparison of the Version-6 and Version-7 TMPA precipitation products over high and low latitudes basins with independent gauge networks: Is the newer version better in both real-time and post-real-time analysis for water resources and hydrologic extremes? ***Journal of Hydrology***, 508: 77-87.

Young, H.Osman, A. M.Aklilu, Y.Dale, R.Badri, B.and Fuddle, A. 2005. Darfur 2005 Livelihoods Under Siege. ***Medford: Feinstien International Famine Center, Tufts University***: 130:40–56.

Yu, H.Zhang, Q.Xu, C.-Y.Du, J.Sun, P.and Hu, P. 2019. Modified palmer drought severity index: model improvement and application. ***Environment international***, 130: 104951.

Zakieldeen, S. A. 2009. Adaptation to climate change: A vulnerability assessment for Sudan. ***Gatekeeper series/International Institute for Environment and Development, Sustainable Agriculture and Rural Livelihoods Programme; 142***: 3–17.

Zambrano-Bigiarini, M.Nauditt, A.Birkel, C.Verbist, K.and Ribbe, L. 2017a. Temporal and spatial evaluation of satellite-based rainfall estimates across the complex topographical and climatic gradients of Chile. ***J Hydrol Earth Syst Sc***, 21(2): 1295-1320.

Zambrano-Bigiarini, M.Nauditt, A.Birkel, C.Verbist, K.and Ribbe, L. 2017b. Temporal and spatial evaluation of satellite-based rainfall estimates across the complex topographical and climatic gradients of Chile. ***Hydrology and Earth System Sciences***, 21(2): 1295-1320.

Zarch, M. A. A.Sivakumar, B.Malekinezhad, H.and Sharma, A. 2017. Future aridity under conditions of global climate change. ***Journal of Hydrology***, 554: 451-469.

Zarch, M. A. A.Sivakumar, B.and Sharma, A. 2015. Droughts in a warming climate: A global assessment of Standardized precipitation index (SPI) and Reconnaissance drought index (RDI). ***Journal of hydrology***, 526: 183-195.

Zhang, H.Kang, J.Xu, X.and Zhang, L. 2020. Accessing the temporal and spectral features in crop type mapping using multi-temporal Sentinel-2 imagery: A case study of Yi'an County, Heilongjiang province, China. ***Computers and Electronics in Agriculture***, 176: 105618.

Zhang, Z.Tian, J.Huang, Y.Chen, X.Chen, S.and Duan, Z. 2019. Hydrologic evaluation of TRMM and GPM IMERG satellite-based precipitation in a humid basin of China. ***Remote Sensing***, 11(4): 431.

Zhong, R.Chen, X.Lai, C.Wang, Z.Lian, Y.Yu, H.and Wu, X. 2019. Drought monitoring utility of satellite-based precipitation products across mainland China. ***Journal of hydrology***, 568: 343-359.